

**ENVIRONMENTAL EFFECTS ON BACTERIAL COMMUNICATION AND  
COMMUNAL BEHAVIOR**

by  
Eric Ka-On Chu

A dissertation submitted to Johns Hopkins University in conformity with the  
requirements for the degree of Doctor of Philosophy

Baltimore, Maryland  
January 2019

© 2019 Eric Ka-On Chu  
All Rights Reserved

# Abstract

Despite their autonomous nature, bacteria can often reside within complex, multicellular communities. One benefit of communal organization is the protection it offers from hazardous environments around the cells, which can come in the form of physical shielding or collective adaptive behaviors that arise from cell aggregation. This dissertation explores how environmental conditions itself might modulate or trigger these collective cell behaviors. We first explored how the environment can affect the active coordination of collective cell behavior, which involves cell-to-cell communication mechanisms such as quorum sensing (QS). Using a microfluidic platform to modulate the environment, we showed that existing explanations of environmental dependence pertaining to modulation of signal retention alone were inadequate in explaining the response. Instead, a dynamics-based analysis coupled with a mathematical model revealed a regulatory mechanism that is defined by the growth-mediated balance between synthesis and dilution of the signaling machinery proteins. This mechanism is able to account for the temporal and spatial properties observed during the onset and propagation of the collective response. These properties culminated in a cell education strategy that effectively combines response diversification with cell signaling to accelerate the onset of the collective cell behavior, which can have tremendous implications for the fitness of the cells that can exhibit this behavior. In addition, we also examined the effects of direct environmental cues, such as mechanical cues, on the emergence of collective cell behaviors. We found that physical confinement of bacterial colonies can lead to a buildup of self-imposed mechanical stress, which can elicit a biological stress response and the secretion of biofilm-related extracellular materials. We demonstrate that this renders the colony biofilm-like, with the

associated functional consequence of increased antibiotic tolerance. Across these studies, we combined engineering approaches with experimentation and computational modeling to explore the relationship between bacterial colonies and its surrounding environment and found a high degree of dependence, most often reflected in spatial dependences of responses. As the appreciation for the importance of the microenvironment and its influence on bacterial colonies grow, we anticipate that the interdisciplinary approaches presented here will prove to be valuable tools in helping us understand the workings of bacterial collective cell behavior.

**Advisor:** Andre Levchenko, PhD

**Readers:** Andre Levchenko, PhD; Jie Xiao, PhD

**Thesis Committee:** Andre Levchenko, PhD; Winston Timp, PhD; Jie Xiao, PhD

# Acknowledgements

First and foremost, I wish to thank my advisor, Prof. Andre Levchenko, for his mentorship throughout my Ph.D. studies. He gave me the freedom and opportunity to explore on my own, which allowed me to make and learn from my own mistakes, and in the process, become a better scientist. For that I am very grateful.

I would also like to thank my thesis committee members, Profs. Jie Xiao and Winston Timp, for their guidance and numerous helpful suggestions over the years that significantly strengthened the work in this thesis. I also wish to express gratitude to Dr. Onur Kilic, who taught me the fundamentals of microfabrication that laid the foundations for much of the work presented in this thesis. I must also thank Prof. Alex Groisman for sharing with me his best microfluidic ideas and helpful critique. I also wish to acknowledge Dr. Hojung Cho for laying down the groundworks for the biofilm study.

I want to express my heartfelt thanks to all members of the Levchenko Lab, past and present, who have taken part in this amazing journey with me. It has been an honor and a privilege to have had the chance to know every one of you, and to be able to learn a little bit about this mysterious world together. Nevertheless, I wish to highlight a few people who have been particularly important to me during my time in the lab as a Ph.D. student. Sincere thanks to Dr. Hao Chang for letting me pick his brain whenever I was stuck on a problem, and also for bringing me on frequent Costco runs to buy pizza, which I am sure fueled more than half of the work done in this thesis. Dr. Tae-Yun Kang never fails to amaze me with her depth and breadth of knowledge, and I thoroughly enjoyed each and

every one of our talks, whether it was about 3D printing or the latest Korean trends. I've also been very fortunate to have met Rebecca LaCroix, who shares the same passion for food as I and with whom I have shared numerous wonderful meals as we explored the New Haven restaurant scene. In no particular order, I also wish to thank Ben, Jinseok, Sunghoon, Kiran, Patrick, Kshitiz, Rita, Masha, and Archer for all of their help and advice, and for making Levchenko lab such a fun place to work. I will always cherish our friendships and remember the numerous fun times we've spent together. I also wish to thank Hong, Naomi, and Meredith for all of their administrative help.

Finally, I wish to thank my family. I thank my parents, Cheuk Wai and Im Ngan, who have both sacrificed so much to give me the chance to succeed, and for all of their love and support, I will always be grateful. I am also extremely thankful for all of the love and prayers from my sister, Jenny, brother-in-law, Jeremy, and nephew, Timothy, which helped tremendously when my cells were not showing me any love. Most important of all, I thank Roxane, my soulmate and best friend, for her unconditional love and boundless patience throughout this long journey. Without her unwavering support and joyous optimism that helped me through the trying times during my studies, this thesis would not have been possible. Thank you.

# Table of Contents

Abstract.....	ii
Acknowledgements.....	iv
Table of Contents.....	vi
List of Tables.....	ix
List of Figures.....	x
Chapter 1. Introduction.....	1
1.1 Bacterial Communities.....	1
1.2 Quorum sensing.....	2
1.3 Biofilms.....	4
1.4 Microfluidics for studying bacteria.....	6
1.5 Aims and significance of this thesis research.....	9
Chapter 2. Influence of the environment on the quorum sensing response.....	12
2.1 Introduction.....	12
2.2 Results.....	14
2.2.1 Development of microfluidic platform.....	14
2.2.2 Characterization of differential diffusive properties.....	16
2.2.3 Characterization of differential growth rates.....	19
2.2.4 Neither classical quorum sensing nor diffusion sensing can explain QS response variation.....	22
2.2.5 Response dynamics is reflective of environmental conditions.....	26
2.2.6 Response dynamics is modulated by balance of synthesis and dilution.....	29
2.2.7 Analysis of the balance of synthesis and dilution to understand QS dynamics.....	32
2.2.8 Mathematical model of QS dynamics.....	35
2.2.9 Medium composition changes synthesis and dilution rates.....	36
2.2.10 Temperature changes synthesis and dilution rates.....	40
2.2.11 Changes in synthesis and dilution affects QS protein accumulation.....	43
2.2.12 Information theoretic analysis of QS sensitivity to environmental conditions.....	48
2.3 Discussion.....	49

2.4 Experimental methods.....	52
2.4.1 Bacterial strain and growth conditions.....	52
2.4.2 Design and fabrication of microfluidic device.....	53
2.4.3 Microscopy.....	57
2.4.4 Image processing and data analysis.....	58
2.5 Computational methods.....	60
2.5.1 Simulation of diffusion.....	60
2.5.2 Simulation of QS response.....	60
Chapter 3. Spatial and temporal correlates of quorum sensing.....	66
3.1 Introduction.....	66
3.2 Results.....	68
3.2.1 Origins of spatial gradients of QS response.....	68
3.2.2 Quantification of spatial gradients.....	70
3.2.3 Spatial responses are nutrient-dependent.....	73
3.2.4 Spatial gradients map onto mean response distribution.....	76
3.2.5 QS exhibits temporal threshold property.....	80
3.2.6 QS response exhibits bistability and hysteresis.....	83
3.2.7 Bistability and hysteresis are dependent on LuxR.....	86
3.2.8 Emergence of an induced subpopulation.....	88
3.2.9 Induced subpopulation as a memory.....	90
3.2.10 Stable maintenance of an induced subpopulation.....	92
3.2.11 Acceleration of onset by an induced subpopulation.....	93
3.3 Discussion.....	98
3.4 Methods.....	101
Chapter 4. Self-imposed mechanical stress can induce biofilm formation.....	102
4.1 Introduction.....	102
4.2 Results.....	103
4.2.1 Confined growth leads to self-generated pressure buildup.....	103
4.2.2 Self-generated pressure buildup leads to biological stress response.....	107
4.2.3 Mechanical stress due to colony expansion leads to biofilm formation.....	108
4.2.4 Biofilm formation is spatially correlated with stress response.....	111

4.2.5 Antibiotic tolerance due to biofilm as a penetration barrier.....	115
4.2.6 Biofilm formation due to self-generated stress within matrix-like environment.....	118
4.3 Discussion .....	124
4.4 Experimental methods.....	126
4.4.1 Bacterial strains and growth conditions .....	126
4.4.2 Device design, fabrication, and operation .....	126
4.4.3 Device calibration and pressure measurement .....	128
4.4.4 Cell staining.....	128
4.4.5 Microscopy and data analysis.....	129
4.4.6 Preparation of hydrogel matrices.....	132
4.5 Computational methods.....	133
4.5.1 Agent-based model.....	133
4.5.2 Mean field model.....	135
Chapter 5. General conclusions .....	137
5.1 Summary of results.....	137
5.2 Future directions and concluding thoughts .....	139
Bibliography .....	143
Curriculum Vitae .....	151



# List of Tables

Table 2.1: Simulation parameter values.....	63
Table 2.2: Dilution rates .....	63
Table 2.3: Synthesis rate .....	64

# List of Figures

Figure 2.1: Microfluidic platform for studying environmental dependence of QS .....	14
Figure 2.2: Characterization of diffusive properties of microfluidic platform .....	18
Figure 2.3: Characterization of growth rates in microfluidic platform.....	21
Figure 2.4: QS response dynamics in tryptone medium with 20 mM glucose.....	23
Figure 2.5: QS response magnitude are non-monotonic functions of diffusive coupling to the environment .....	25
Figure 2.6: Evolution of QS dynamics in tryptone medium at 25° .....	27
Figure 2.7: Response dynamics governed by balance of synthesis and dilution .....	30
Figure 2.8: Juxtaposition of nutrient conditions within gradient-generating device .....	37
Figure 2.9: QS response dynamics in casamino acids medium at 25°C.....	38
Figure 2.10: Evolution of QS dynamics in casamino acids medium at 25°C.....	39
Figure 2.11: QS dynamics within various conditions at 30°C.....	41
Figure 2.12: QS dynamics of LuxR perturbations .....	44
Figure 2.13: Components of QS response dynamics exhibit differential sensitivity to environmental conditions.....	47
Figure 2.14: Information theory analysis of dynamics sensitivity to environmental conditions.....	48
Figure 3.1: QS expresses spatial gradients of response .....	71
Figure 3.2: Quantification workflow for spatial gradient and onset location .....	72
Figure 3.3: Spatial responses exhibit condition-dependent dynamics .....	74
Figure 3.4: Non-monotonic QS dependence on local growth rate specifies divergent spatial QS gradients and onset locations.....	77
Figure 3.5: QS displays temporal thresholding and hysteretic properties .....	82
Figure 3.6: Hysteretic response in transient environments.....	86
Figure 3.7: Simultaneous induction and repression elicits induced subpopulation .....	89
Figure 3.8: Microfluidic device for screening conditions optimal for emergence of induced subpopulation .....	94
Figure 3.9: Memory of QS-conducive environment can accelerate subsequent QS onset	95

Figure 3.10: Response dynamics within various initial glucose concentrations and positions .....	97
Figure 4.1: Microfluidic device for measuring pressure from growth within confinement.....	105
Figure 4.2: Bacterial growth within confinement can lead to buildup of pressure.....	107
Figure 4.3: Pressure buildup as a result of confined growth leads to biochemical stress response.....	109
Figure 4.4: Pressure buildup and stress response leads to expression of biofilm markers.....	110
Figure 4.5: Spatial correlation between expression of biofilm-associated cell surface structures and biochemical stress response.....	112
Figure 4.6: Direct application of pressure.....	114
Figure 4.7: Confinement-dependent formation of a selective penetration barrier confers increased antibiotic tolerance.....	117
Figure 4.8: Selective penetration of molecules into the colony.....	119
Figure 4.9: Biofilm growth in environment with mechanical resistance.....	121

# Chapter 1: Introduction

## 1.1: Bacterial communities

In recent years, there has been a gradual shift in the perception of how bacteria behave. Due to their simplistic nature as single-celled organisms, bacteria are traditionally thought of as independent, autonomous beings. However, increasing evidence suggests that bacteria are not asocial like once thought, but rather can reside in highly-organized, complex multicellular communities. One reason to do so is that the environment surrounding the cells can often be hazardous, and residing within a community and engaging in social interactions with other cells might help facilitate the onset of collective adaptive behaviors that can confer protection. These collective adaptive behaviors are not unlike the coordinated behaviors prevalent within many multicellular organisms which enable complex responses to diverse ranges of stimuli [1-3].

The bacterial communities that arise could span multiple scales, from small cell clusters comprised of the same species, to the vast, diverse multicellular consortia that is the gut microbiota residing within host animals [4]. The recent discovery that the gut microbiome plays a vital role in shaping the health of the host has further increased the appreciation for the complexity and importance of bacterial communities [5, 6]. Since the composition of the gut microbiome is in constant, delicate balance, the harmonious coexistence and organization of the vast numbers of species within gut microbiota necessitates the interaction and exchange of information between cells [7, 8]. Within these complex microbial communities, the bacteria can interact with cells from the same species, cells from different species, and even cells belonging to the host [9, 10]. One method by which

cells can interact with other cells and coordinate their actions is a chemical-based signaling system called quorum sensing.

## **1.2: Quorum sensing**

Quorum sensing (QS) is the archetypal cell-to-cell communication mechanism for the coordination of collective cell behavior within a wide variety of prokaryotes [11, 12]. Mechanistically, it is a form of paracrine signaling whereby bacterial cells from the same or different species produce, release, and detect small pheromone-like diffusible chemical cues called autoinducers (AI) [13]. The detection of AI by its cognate receptors within the recipient cell often leads to induction of gene expression. This frequently include genes that are involved in the collective phenotype, as well as genes that encode for the QS machinery proteins [14]. Thus, the detection of AI often initiates a positive feedback loop that results in the production and release of more signal that can further induce the same cell or increase the propensity of activation in other, neighboring cells, resulting in the coupling of gene expression and the onset of synchronous behavior within a cell population. Due to this inherent positive feedback interaction, QS responses have traditionally been regarded as on-off switches that are triggered when the AI concentration exceeds the threshold level required for induction to occur [15]. However, the amount of AI that accumulates is partly a function of the number of cells (i.e. the more cells there are, the more AI there is), since cells produce AI endogenously. As a result, QS induction is often triggered in a cell number-dependent manner, leading it to be classically defined as a means by which a population can sense whether there are enough cells to successfully

execute collective cell behavior [16, 17]. This cell number dependence is what led the researchers who discovered this signaling system to coin the term “quorum sensing [18].”

QS is used by different species of bacteria to coordinate a wide spectrum of collective cell behaviors, such as sporulation [19, 20], virulence [21-23], and biofilm formation [24-26]. Across many diverse species of bacteria, numerous different QS signaling molecules and network architectures are used to achieve the population-wide synchronization. For example, within the canonical *Vibrio fischeri* LuxI/LuxR system, the AI is N-(3-oxohexanoyl)-L-homoserine lactone, an acyl-homoserine lactone, or AHL [27]. This AI is produced by basally expressed AI synthase LuxI, and can freely diffuse into and out of cells, bind to its cognate cytoplasmic receptor LuxR, and increase transcription of the divergent operon, consisting of *LuxR* on one side and *LuxICDABE* on the other, the latter of which encodes for a strong positive feedback as well as for the bioluminescence [28-30]. In many cases, multiple systems can be found within one single species. For example, in *Vibrio harveyi*, three different classes of AI are used, which bind to membrane-bound receptors and inhibit the activation of a phosphorylation cascade, resulting in the cessation of transcription of Qrr sRNAs that regulate translation of master regulators, ultimately leading to onset of collective behavior [31, 32]. Within gram positive bacteria such as *Staphylococcus aureus*, peptide-based AIs are used to orchestrate collective cell behavior [33, 34]. *S. aureus* uses the peptide AI called autoinducing peptide (AIP), which binds to a membrane-bound receptor and leads to phosphorylation of a protein that can activate transcription of genes that lead to pathogenesis.

Despite the variability in AI and network architectures between different species, the activation of a QS response still relies on the accumulation of AI. However, because the AI can diffuse freely, its accumulation is highly subjected to environmental conditions, such as the degree of spatial confinement that could aid in signal retention or the rate of fluid flow that could remove AI through convection [35, 36]. In fact, the strong dependency of the QS response on the immediate environment around the cell led to the formulation of alternative theory of diffusion sensing (DS), which stipulated that QS evolved as a means by which the cell can evaluate the diffusive and geometric properties of the immediate environment, rather than the conventional theory of population counting [37]. The theory states that the released AI molecules only serves as a proxy to gauge whether the environment would be favorable for the release of metabolically expensive goods targeted for secretion into the surrounding milieu. Therefore, this alternative theory also implies that there is no cell-to-cell communication aspect to the behavior, and is a purely cell autonomous behavior. A unifying theory of efficiency sensing (ES), which combines the ideas of QS and DS while also taking into account the density and spatial distribution of the cells within a population, has also been proposed [38]. It is important to note that, despite the appreciation for the effects of the environment, none of these alternative theories account for the effects of the environment other than its effects on the accumulation of AI.

### **1.3: Biofilms**

A widely known example of bacterial communities is a bacterial biofilm. Bacterial biofilms are, at its very essence, a population of cells that is encased within an extracellular matrix

comprised of extracellular polymeric substances (EPS) such as polysaccharides, proteins, lipids, and DNA that are secreted by the cells themselves [39-42]. Biofilms are found in a wide variety of settings, from the teeth of animals [43] to the surfaces of medical devices and apparatuses [44, 45]. Biofilms often have complex, three-dimensional structures supported by the matrix, which forms a growth environment that is vastly different from that in the planktonic state, with some properties and ramifications that will be explored in a later chapter. Our understanding of biofilm formation has improved greatly with advances in imaging technology [46]. Biofilm formation is proposed to occur in five stages [47, 48]. Biofilm formation initiates with weak, reversible attachment of the cells to the surface by van der Waals forces or hydrophobic effects. This is followed by strong adhesion, which can be mediated by surface pili. Irreversible attachment then facilitates the next two stages of maturation of the biofilm via the growth of the cell into a colony, with the concomitant production and release of EPS to form the surrounding matrix. The final step is the dispersal stage, where cells residing within the biofilm structure return to the bulk fluid via various detachment mechanisms such as enzymatic digestion of the biofilm matrix. The dispersal of cells from the biofilm can allow for the colonization of new surfaces, and can involve the detachment of individual cells (swarming), clusters (clumping) or whole biofilms (surface). These stages appear to be relatively conserved across a wide range of prokaryotes.

The formation of a biofilm can impart constituent cells with numerous properties. The physical structure can facilitate the maintenance of cells in close proximity with each other and create a relatively stable environment for cell proliferation that is substantially different



from planktonic culture [49]. Being adjacent to other cells could enable the cooperation between cells via QS [26], but could also lead to increased competition between cells for the limited resources [50]. The properties of the biofilm matrix itself can also affect the viability of the cells in various ways. Molecules of interest can adsorb onto or absorb into the biofilm matrix and remain in the vicinity of the cells and be concentrated so that it may be utilized by the cells [51, 52]. However, the sorption of molecules is nonspecific, so it is possible that harmful molecules can be retained in the biofilm. Despite this, the biofilm composition is malleable and can be remodeled by the cells to adapt to more challenging conditions. The biofilm matrix can also help retain particulates from the cells, such as residual cellular debris after it dies, or enzymes that are secreted by cells to create an extracellular digestion system [53]. Finally, biofilms can also protect cells from the effects of antimicrobial molecules, either through acting as a penetration barrier, creating conditions conducive to the transition to dormancy which protect against growth-dependent antimicrobial agents, or facilitating the exchange of resistance genes [54, 55]. These protective qualities that aid in the survival of the cells are also the features that make biofilm-related infections so difficult to treat in the clinic. Therefore, biofilms can drastically change the local environment around the cells in order to protect it from adverse conditions, but it is not clear how the environment might actually affect biofilm initiation or its modulation.

#### **1.4: Microfluidics for studying bacteria**

Microfluidics has been an invaluable tool in the field of biology within the past decade. Lab-on-a-chip microfluidics technology has enabled the miniaturization of traditional

biochemical assays, which allows reagents to be conserved as well as increasing the throughput [56, 57]. However, it is the application to cell culture that has enabled scientists to tackle biological questions that were previously inaccessible [58-60]. Microfluidics offers a highly customizable and cost-effective method to create precisely controlled environments for mimicking *in vivo* conditions to study cellular behavior within a more natural context. Since the feature sizes within microfluidic devices are the same length scale as cells, the perturbations from the spatial environment are relevant [61]. Preserving the spatial context within a cell colony is important due to the fact that cellular responses are often not homogeneous, but rather heterogeneous, even within clonal populations [62]. Traditional assays that involve the averaging of signals from an entire population would result in the loss of the information regarding response variation, which could be even more prevalent within a spatial context. Microfluidic cultures can preserve spatial information that would otherwise be lost, enabling the study of correlation between space and response. Microfluidics also allow for the long-term culturing of populations, allowing for the examination of real time responses to precisely controlled spatiotemporal perturbations [63-65]. Therefore, microfluidics offers a best-of-both-worlds solution in that it combines the spatial organization characteristics of natural, *in vivo* environments, that is absent in traditional lab culture methods, while allowing for the precise control of environmental variables necessary for experimentation that is often easy to do in traditional cell culture but difficult to do within *in vivo* settings.

Traditional experimentation with bacteria involves growth within well-mixed, planktonic bulk culture. The continuous agitation ensures that bacteria are well aerated and have

access to fresh nutrients while removing surrounding accumulation of metabolic byproducts, but also prevent the formation of cohesive cell ensembles. Chemostatic growth within bulk culture is achieved by pumps that continuously supply an influx of fresh media at a rate that is equal to the removal of the existing culture. Microfluidics has been applied to the culturing of bacteria with great success, which overcomes some of the shortcomings of traditional chemostatic culture [66-68]. Cells can be cultured within chambers and expand within a spatially well-defined environment. Nutrients and waste products can be continuously supplied and removed, respectively, via flow-through channels [58]. Bacterial colonies within microfluidic chemostats can be grown indefinitely while enabling the continuous observation of spatially organized colonies. The dimension of the chamber can also be made such that the height of the chamber is similar to the dimensions of the cell, such that the growth of bacterial colonies are restricted into a monolayer, enabling single-cell studies [59]. This design aspect can be modified even further, by also restricting the width of the chamber to the dimensions of the cell such that colonies are arranged in straight lines. These “mother machines” enable the observation of bacterial growth at a single-cell level, and the termination of one end of the chamber ensured that the lineages of that one cell (mother) at the end can be continuously tracked [69]. These improvements to the bacterial chemostat enabled studies that were previously not possible.

In addition to enabling the simple culturing of bacterial colonies, researchers have also used the unique features of microfluidics to study other phenomena that are otherwise impossible to study in bulk culture. For example, since QS is dependent on the accumulation of the diffusible AI molecule, auto-induction of the QS response within

populations is subjected to environmental conditions. By embedding cells that can only produce the signal within hydrogel spots upstream and cells that can only receive the signal downstream, it was shown that the flow rate determined the induction states of the receiver cells, by affecting the accumulation of the AI produced by the transmitting cells [36]. The formation of a biofilm matrix, however, can counteract the inhibitory effects of flow and aid in the accumulation of AI and induction of QS [25]. In comparison, a complete confinement of single cells within chambers that are picoliters in volume can lead to the accumulation of AI and induce the onset of a QS response in the absence of the quorum [35]. The ability to precisely control the microenvironment makes microfluidic platforms a very useful tool for the study of biological phenomena.

### **1.5: Aims and significance of this thesis research**

The study of bacterial communities is often limited by the ability to observe their behavior within their natural, and often highly structured, environments. Microfluidics provide a platform to approximate the natural spatial organization that can occur while simultaneously imparting the ability by experimenters to precisely manipulate the micro-environment. Such an approach would allow us to glean important new information about how bacterial communities gather information about and interact with the environment. While many of the collective adaptive responses initiated by bacterial communities is to counter adverse environmental effects, it is surprising that the dependence of collective behavior on the environment is still poorly understood. Therefore, the general aim of this thesis research is to explore the effects of the environment on the behavior of bacterial colonies, within the contexts of both its effects on the active signaling mechanisms

involved in coordination, as well as its effects on direct cues, such as mechanical cues, that can guide collective cell behavior, through the development of novel microfluidic platforms. This thesis is organized along three aims:

**Specific Aim 1: Explore the influence of the environment on the quorum sensing response (Chapter 2).**

Here, we describe the development of a microfluidic platform that can modulate the nutrient composition and access. Through experimentation and modeling, we identify a unifying mechanism which modulates the QS response in different conditions. The sensitivity of the response to the environmental input is also analyzed.

**Specific Aim 2: Investigate spatial and temporal correlates of quorum sensing (Chapter 3).**

We apply the platform developed in aim 1 to explore properties of QS that arises from changes in environmental conditions. We provide insights into how these properties serve to define the onset and propagation of QS and uncover how individual cells contribute to the emergence of collective response. Finally, we compare how a cell-cell communication system within different environments might provide different fitness results versus the commonly assumed bet-hedging strategy.

**Specific Aim 3: Investigate biofilm formation in the setting of self-induced mechanical stress and limited nutrient access (Chapter 4).**

In this aim, we develop a new platform to study how mechanical stress as a result of spatial confinement is related to biofilm formation. Using a combination of experiments and modeling, we further our understanding of the impact of confinement on a growing bacterial colony.

The work presented in this thesis provides novel tools for studying the behavior of bacterial colonies growing within various environmental conditions. The tools enable the precise control of the spatial and chemical environment that can mimic natural conditions the bacterial colonies often reside in. This can be applied to study mechanically- or chemically-based emergent behaviors. For instance, we manipulated the environmental conditions to uncover significant new insights into the temporal and spatial control of QS onset and propagation, implicating the importance of additional factors in the regulation of the signaling system that was previously unknown. Furthermore, we utilized a similar set of tools to elucidate mechanically-based triggers of biofilm formation, which can occur as a result of growth within confinement and independent of other causes.

# Chapter 2: Influence of the environment on the quorum sensing response

## 2.1: Introduction

Because to the diversity of bacterial species and the possibility of multiple QS systems within the same species, much of the research efforts on QS have been focused on the identification of novel signaling systems and network components, which are largely performed in bulk culture [70-73]. While experiments in well-mixed bulk culture, which are often supplemented with saturating levels of exogenous signals, provide a homogeneous environment through which the components of the genetic circuit can be precisely characterized, it overlooks the complexity and sensitivity of the response that could arise from the organization of bacterial communities within its natural environments. Since paracrine signaling systems such as QS rely on released, diffusible signals, the collective response is understandably sensitive to environmental conditions and perturbations [36, 74]. Environmental conditions are understood to have a tremendous impact on the ability to retain the diffusive AI molecule in high enough concentrations such that it can induce expression of QS circuitry within cells. While the diffusion sensing interpretation of QS has undoubtedly increased the appreciation of the potential effects of the environment on the QS response, as exemplified by studies of how flow and confinement impact AI retention and QS induction, the overall influence of the environment on the QS response remains an aspect of collective cell behavior that has been, for the most part, poorly addressed on a quantitative level [75, 76]. More specifically, these studies have mainly focused on the effects of the environment on AI accumulation, but

have largely ignored the effects on the other diffusible molecules: the nutrients. Since spatial confinement and structuring of cells can result in the formation of local environments with variable degrees of mass transport, environments that affect the accumulation of AI can likewise affect nutrient access, in a negatively correlated relationship. For example, while conditions such as high cell density or spatial confinement are conducive to the retention of QS signals, they can also exacerbate the limited nutrient availability because of decrease in the mass transfer [35, 77].

Nutrient limitation is an important factor to consider in the analysis of QS response because it can have far-reaching effects in changing not only the cell proliferation rate, but also the transcriptomic [78] and proteomic profiles [79]. Yet, how information regarding the nutrient environment is integrated with AI sensing into QS-based cellular decision making is currently unclear. Furthermore, the QS-mediated behaviors themselves are often adaptive behaviors triggered to counteract adverse environmental conditions, such as sporulation [19, 20], virulence [21-23], and biofilm formation [24-26]. However, our understanding of how the magnitude of that response is reciprocally defined by a key aspect of the environment, nutrient availability, is currently lacking. For example, while the formation of a biofilm can create a protective barrier that enables the shielded colony to thrive within an otherwise inhospitable environment, the barrier could also act as a double-edged sword and hinder the mass transfer of nutrients into the core of the colony [80]. Studies incorporating spatial organization of bacterial cells could unravel the complex interactions between cells and their environment that could reveal universal key modulators of QS-mediated collective cell behaviors. Microfluidics offer the ideal platform to address



such questions, since culture chambers could be designed to accommodate cell colonies of various sizes, with the culturing conditions under precise control either through medium composition or access. Colonies could also be cultured chemostatically, enabling the long-term monitoring of QS behavior. Thus, we decided to employ a microfluidic approach to study the relationship between QS and environmental conditions.

## 2.2 Results

### 2.2.1: Development of microfluidic platform

Since the goal is to explore the link between QS response and environmental conditions (Figure 2.1A), the device was designed with the ability to modulate both the environment's chemical composition and its diffusive coupling with dense cell colonies, enabling high-

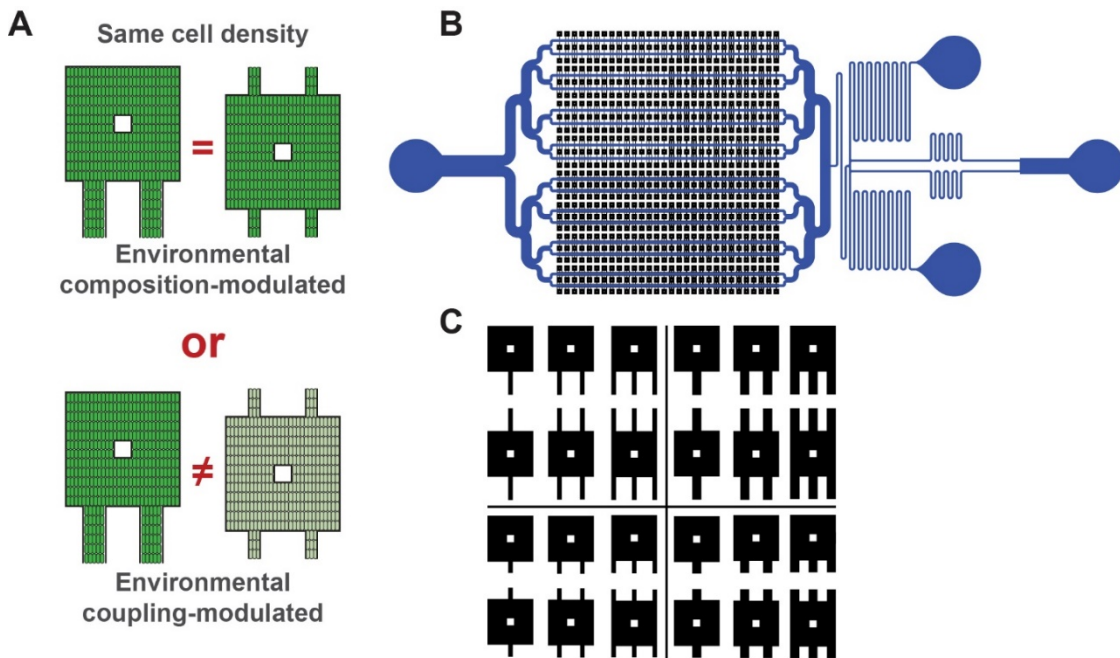


**Figure 2.1: Microfluidic platform for studying environmental dependence of QS.** **A**, Diagram illustrating the difference between environmental composition-modulation versus coupling-modulation of the QS response within identical cell density conditions. **B**, Diagram of microfluidic device. **C**, Diagram showing the distribution of the 24 unique configurations within the four quadrants of the chamber array.

throughput evaluations of various nutrient conditions. We designed a microfluidic platform with two inlets for the selective supply of media via a switch built into the channel design that allows the instantaneous switches between the two inputs, as well as a downstream array of chambers that are identical in dimensions but different in numbers and sizes of connective channels for modulating the diffusive coupling to the flow-through channels (Figure 2.1B). By systematically varying the number and dimensions of the connections, or capillary channels, between the chambers and flow-through channels, we vary the rate of interaction and molecular exchange between the colony and the environment, which, when coupled with the consumption by the cells residing in the chambers, can create differences in nutrient conditions between the different chambers. The 720-chamber array consists of 24 different chamber configurations (Figure 2.1C). All of the chamber configurations have identical  $100 \times 100 \times 0.8 \mu\text{m}$  dimensions, which has a high aspect ratio and makes the chambers highly resistant to cross flows, so the dominant form of chemical exchange between the chambers and the flow-through channels is diffusion. The  $15 \mu\text{m}$  tall flow-through channels and sufficiently high flow rate ensure delivery of enough nutrients to the relatively large area of the chamber to permit chemostatic growth of *E. coli* colonies of  $\sim 3500$  cells each. The cell number in each chamber is kept at a relatively steady level by the continuous escape of proliferating cells through the coupling channels, which ensured the occurrence of multiple cell generations in each dense colony. The shallow height of the chamber, on the order of the diameter of the cell, also ensures that in most cases, cells that reside within each of the different chamber configurations are filled to capacity and are maintained at similar cell numbers and densities in the form of a monolayer oriented in the plane of the device. The monolayer also allows for

straightforward comparisons between chamber configurations without the need to normalize to the density of cells. This ensures that any differences observed between chamber configurations are due to differences within the cells themselves, and not an artifact as a result of observing the cumulative signal from multiple layers of cells.

### **2.2.2 Characterization of differential diffusive properties**

To evaluate and compare the mass transport properties between the different chamber configurations with varying degrees of coupling with the environment, we perfused a fluorescent dye molecule into the flow-through channels of the device and monitored the fluorescence change within the chambers as diffusion occurred. Different chambers are expected to have different diffusion rates due to different cross-sectional areas through which the flux of diffusible molecules can pass through, as well as different lengths between the flow-through channels and chambers that diffusible molecules travel through before reaching the square chamber region. Alexa Fluor 555 dye was chosen to serve as a proxy for a diffusible molecule of interest, such as autoinducer (AI) or nutrients, because it allowed for the visualization and quantification of the differences in diffusion time between the different chamber configurations. Alexa Fluor 555 has a relatively high molecular weight as compared to many diffusible molecules of interest (1150 g/mol, as compared to 213.23 g/mol for AI and 180.16 g/mol for glucose), imbuing it with a smaller diffusion coefficient and longer diffusion time than many molecules that are at play, which would make its transport dynamics representative of the slower diffusing nutrient molecules, but also encompass the dynamics of smaller, faster diffusing molecules. The slower diffusing Alexa Fluor 555 would provide an idea of the timescales involved in

nutrient access, enabling the comparison to the timescales of other processes such as growth and QS response later on.

A three-dimensional (3-D) simulation of diffusion dynamics inside virtually recreated chambers of identical dimensions was performed in COMSOL Multiphysics modeling software. The simulation of the diffusion of a molecule with diffusion coefficient of  $2 * 10^{-10} m^2 s^{-1}$  at a concentration of 0.1 mM, corresponding to Alexa Fluor 555, into a chamber was performed by maintaining the interface between the capillary channel and flow-through channel at constant concentration, and allowing diffusion to occur until the mean concentration within the square chamber region has equilibrated with the source, (i.e. reached 0.1 mM). The time required for equilibrium to occur between the 24 chamber configurations range from approximately 1 to 15 minutes (Figure 2.2A). In general, chambers with a larger total cross-sectional area in the capillary channels or shorter capillary channels tended to require less time for equilibrium to occur. Validation of the model predictions was performed by continuous perfusion of the flow-through channels with an Alexa Fluor 555 dye solution while the chambers are filled with cells and by using epifluorescence time-lapse microscopy to capture the fluorescence signal within each chamber type as the dye molecule diffused from the flow-through channels into the chamber via the capillary channels. Averaging the signal within the square chamber region for each chamber type reproduced similar dynamics as the simulation, with the mean fluorescence intensity saturating within one minute for the chamber configuration with the highest diffusive coupling, and within 15 minutes for the chamber configuration with the highest diffusive coupling (Figure 2.2B). The timescale of the dynamics for the diffusion

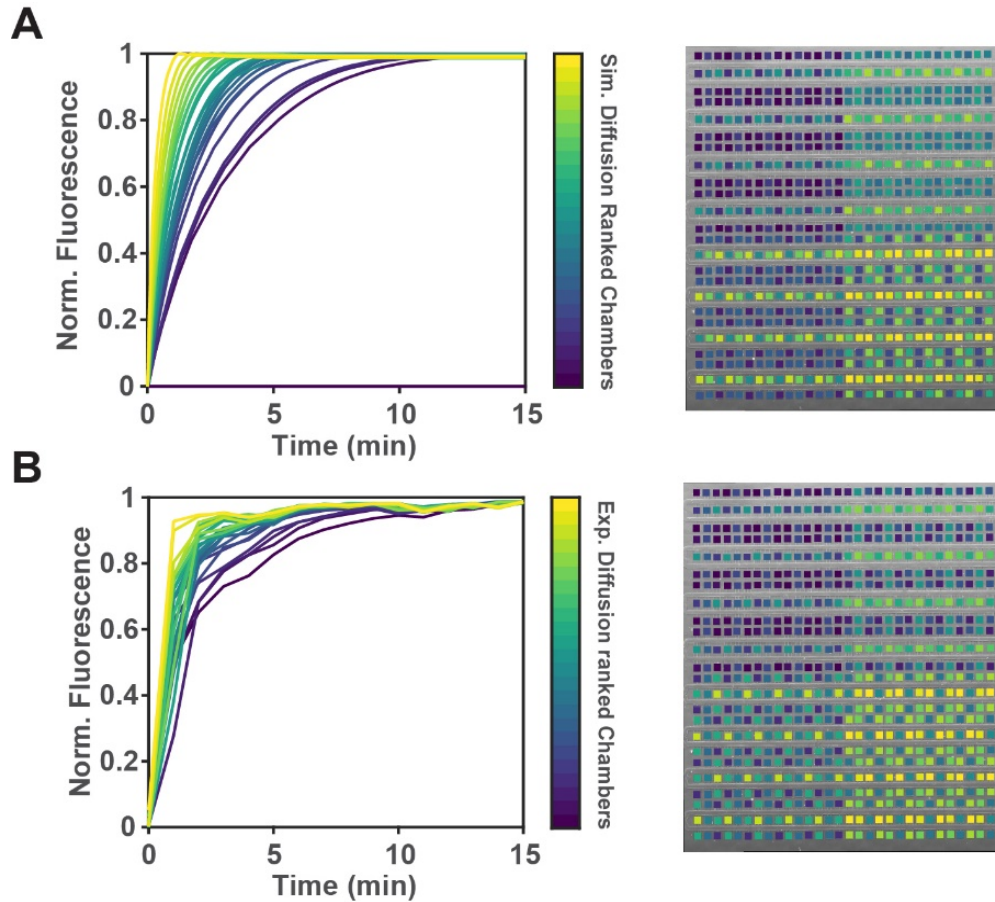


**Figure 2.2: Characterization of diffusive properties of microfluidic platform. A, B,** Diffusion dynamics and phase contrast micrograph of microfluidic device color-coded according to the ranking of chambers determined from simulated (A) and experimental ( $n = 2$ ) (B) dye diffusion.

of dye out of the chamber is identical as well. As was the case in the simulations, configurations possessing a larger total capillary channel cross-sectional area or shorter capillary channels generally required less time for the inert dye to equilibrate. Since the dye is neither consumed nor degraded by the cells, the fluorescence signal saturates as the concentration in the chamber becomes uniform and reaches equilibrium with the flow-through channel. A molecule that can be altered by the cell, such as nutrients, would, however, be expected to have different local concentrations, if the consumption of nutrients in a particular region happen on a time scale that is faster than the time scale for nutrients to diffuse to the region. Nevertheless, both experiments and simulations indicate that the

diffusion dynamics of this relatively heavy dye molecule occurs on the time scale of minutes, with diffusion of smaller molecules potentially occurring even faster.

### **2.2.3 Characterization of differential growth rates**

To ascertain whether the differences in transport rates of molecules such as nutrients into the chamber translates into observable phenotypic differences in terms of cell proliferation, we need to determine the mean growth rate within the chamber configurations. Due to the dense packing of cells within the relatively large dimensions of the chamber, direct measurement of growth rate on a single-cell level is not easy to perform. The segmentation and lineage tracking of ~3500 cells densely packed together makes the task computationally challenging. The mean rate of colony expansion could potentially be estimated by monitoring the bulk movement of cells towards the chamber exits as a result of proliferation with techniques such as optical flow, but it might not be able provide the resolution to distinguish small differences in growth rates between various chamber configurations. The mean growth rate could theoretically be obtained in a relatively easy manner by monitoring the rate of dilution of a stable protein, in which its synthesis has ceased, and its degradation is negligible due to its stability. Therefore, the concentration of the protein is only reduced when the continuous cycles of cell growth and division lead to the distribution of a finite amount of protein into an ever-expanding total cell volume, making the rate of protein decrease proportional to the growth rate. Green fluorescence protein (GFP) serves as a good candidate for this purpose for several reasons: since the protein level would be proportional to the fluorescence signal, it can be measured with live-cell microscopy, and the GFP molecule can be extremely stable [81], so loss of signal from

degradation and bleaching would be minimal. The inducible production of GFP would allow synthesis of the protein to be initiated and halted on command, which would allow for the accumulation of the protein to a detectable level before ceasing its production. Since fresh medium is continuously supplied in the flow-through channels, cell proliferation is not limited in time, with growth maintained at a constant rate. The continuous division of cells leads to serial dilution of GFP and loss of fluorescence signal. Thus, fluorescence loss is proportional to rate of proliferation, which is expected to be exponential as a result of chemostatic growth, allowing for the growth rate within each chamber type to be estimated by an exponential decay function fitted to the fluorescence intensity.

The *E. coli* lab strain MG01S [73], which is MG1655 containing a genomically integrated, truncated version of the *Vibrio fischeri* QS *lux* operon containing the *LuxR* gene under the control of the endogenous *LuxR* promoter, the Lux box, and a *GFP* gene under the control of the endogenous *LuxI* promoter, was used in conjunction with the aforementioned method to estimate the mean growth rate of colonies within the different chamber configurations. Upon the addition of exogenous AI (N-3-oxo-hexanoyl L homoserine lactone), the AI binds to LuxR to form a complex that dimerizes and activates the transcription of *LuxR* and *GFP* genes, leading to the production of GFP and subsequent detection of fluorescence, which we classify as the induced state. Since the strain lacks the ability to produce LuxI, and thus, lacks the ability to produce endogenous AI itself, the production of GFP can be initiated or halted, with the addition or removal of exogenous AI, respectively. Exposure to exogenous AI after initial cell seeding into the chambers and during the growth and expansion of the colony to fill the empty space of the chambers allowed the cells to be

uniformly induced across all chamber configurations prior to the onset of nutrient-dependent effects, if any exists (Figure 2.3A). Upon filling the chambers to capacity, the exogenous AI was removed from the flow-through channels, which allowed residual AI to diffuse out and be cleared from the chambers by the flow, ultimately halting GFP production (Figure 2.3B). Given the results from the dye diffusion experiments, the exogenous AI is expected to be removed from the chambers within 15 minutes, and

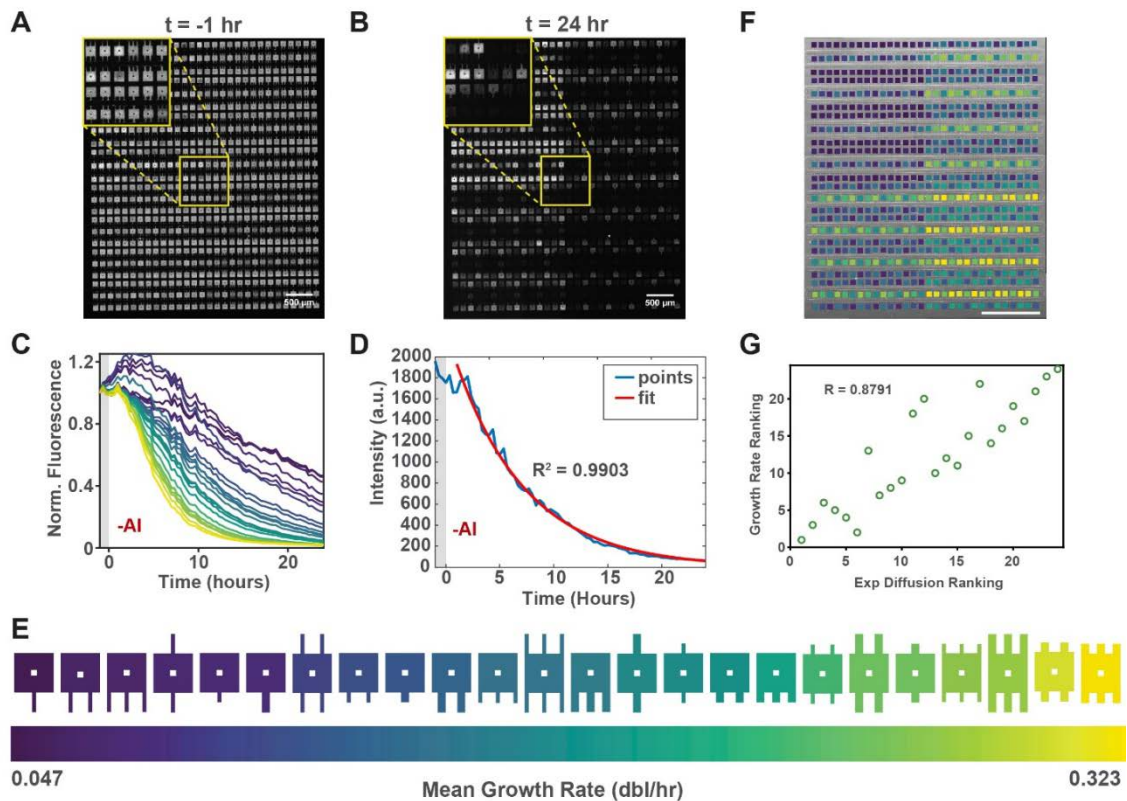


**Figure 2.3: Characterization of growth rates in microfluidic platform.** **A,B,** Fluorescence micrographs of chamber array containing MG01S cells taken **(A)** 1 hour before and **(B)** 24 hours after AI removal in tryptone medium at 25°C. Insets contain magnified view of the region indicated, which contains all 24 chamber configurations. Scale bars, 500  $\mu\text{m}$ . **C,** Protein dilution dynamics in chambers. ( $n = 6$ , from 3 independent experiments) **D,** Representative example of signal decay overlaid with exponential fit after AI removal. **E,** Color-coding of chamber configurations based on mean growth rate determined from dilution experiment. **F,** Phase contrast micrograph of microfluidic device overlaid with color-coding corresponding to the 24 unique coupling configurations. Scale bar, 1 mm. **G,** Correlation of chamber rankings determined from experimental diffusion time and growth rate.



potentially much less, given the smaller molecular weight of AI as compared to Alexa Fluor 555. The continuous cell division coupled with the suspended GFP production from the transient exogenous AI exposure resulted in the decay of the fluorescence signal due to the dilution of stable GFP molecules (Figure 2.3C). By fitting an exponential decay function (Figure 2.3D) to the GFP fluorescence intensity for all 24 chamber configurations and extracting the rate constant, the estimated growth rates of all chamber configurations were determined (Figure 2.3E,F). Comparison of the chamber order when ranked according to the experimentally determined dye diffusion time, and the chamber order when ranked according to the experimentally determined growth rate, resulted in a positive correlation ( $R=0.8791$ ), which suggests that faster diffusion corresponds to faster growth rates, most likely from the increased access of nutrients (Figure 2.3G).

#### **2.2.4: Neither classical quorum sensing nor diffusion sensing can explain QS response variation**

Differences in the degree of diffusive coupling between the chambers and the flow-through channels have demonstrated observable differences in mass transport and growth rates, which are both positively correlated. In order to explore whether the differences in nutrient access and growth rates translate to differences in the QS response, we utilized the QS signaling-capable *E. coli* lab strain MG02S [73], which is identical to the MG01S strain with the exception that it also has the endogenous *LuxI* gene upstream of the GFP reporter under the endogenous *LuxI* promoter. The *LuxI* gene enables the cells to make LuxI, which is the AI synthase that produces endogenous AI, thereby, allowing for auto-induction and self-maintenance of the QS response as a result of the activation of the positive feedback-

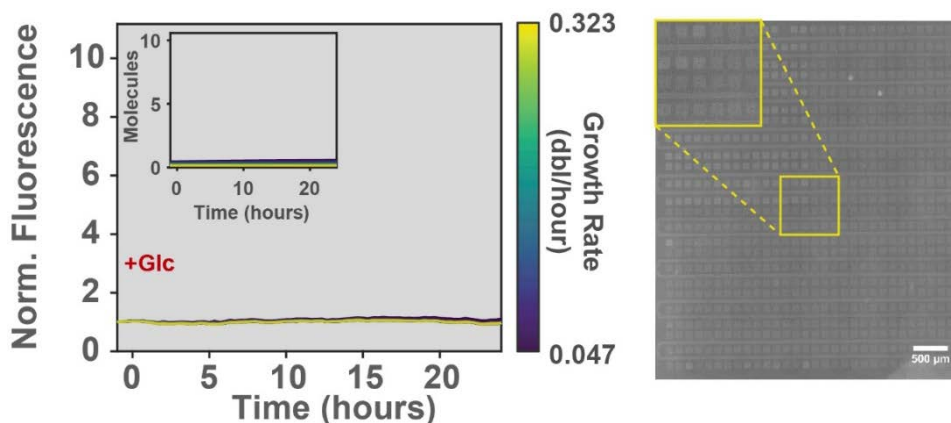


**Figure 2.4: QS response dynamics in tryptone medium with 20 mM glucose.**

Response dynamics and fluorescence micrograph of auto-induction in tryptone medium with 20 mM glucose at 25°C ( $n = 6$ , from 3 independent experiments). Inset in graph contains simulated dynamics. Inset in fluorescence micrograph contains magnified view of the region indicated, which contains all 24 chamber configurations. Scale bar, 500  $\mu\text{m}$ .

regulated production of LuxI. Due to the presence of a CRP binding site in the LuxR promoter region, the presence of glucose suppresses the QS response. We utilize this dependency to suppress the QS response by growing the cells in tryptone-based M9 media supplemented with 20 mM succinate and 20 mM glucose at 25°C, until all the chambers are filled with cells such that density conditions are comparable across all chambers and the effects of nutrient dependence are maximized. These cells exhibited no detectable QS when grown within these conditions, even 24 hours after chambers reached maximum occupancy (Figure 2.4). Once the medium is switched to glucose-free medium, cells are able to produce basal levels of LuxR and respond to endogenously produced AI. After 24 hours of glucose-free conditions, all chamber configurations exhibited fluorescence, indicating cells have initiated a QS response in the form of triggering the positive-feedback loop leading to GFP production (Figure 2.5B). The fluorescence micrograph also indicate that different chamber configurations exhibit different levels of fluorescence, despite equivalent cell numbers and densities between them, suggesting the differential QS

response is related to the differences in diffusive coupling amongst the various chamber configuration (Figure 2.5A).

Although the results initially appeared in agreement with the Diffusion Sensing interpretation of QS, we surprisingly found that the degree of QS induction varied with the extent of diffusive coupling (and cell growth rate) in a non-monotonic, biphasic fashion. The QS response intensity in the chamber type with the slowest growth is relatively low, but the intensity increases as the growth rate increases. However, the intensity reaches a maximum in chambers with intermediate growth rates, after which the intensity proceeds to decrease as growth rate continues to increase. To further explore if AI accumulation in individual chambers due to differential diffusive coupling would be the determinant of the QS response, as postulated by the Diffusion Sensing model, we repeated the experiment by inducing the QS response with the introduction of 1  $\mu\text{M}$  (10x saturating) exogenous AI in the flow-through channels concurrent with the removal of glucose. The addition of exogenous AI should remove the diffusive coupling-mediated differences in AI accumulation, by saturating all chambers with more than enough AI to maximally induce the response. Therefore, if the modulation of the response was indeed due to differences in AI accumulation from differential accumulation of AI, the addition of exogenous AI would homogenize the response between the different chamber configurations. Unexpectedly, after 24 hours of exogenous AI exposure, the relative pattern of fluorescence signal in the fluorescence micrograph (Figure 2.5C) as well as the biphasic response distribution (Figure 2.5D) were very similar as compared to the auto-induction case, suggesting that the differences in QS response intensity between chamber configurations is not due to differences in AI levels, and that the endogenously produced AI is sufficient to fully induce

QS response in the colony. This also dispels the notion that differential chamber access predominantly regulates AI retention, since the most restricted chamber would accumulate

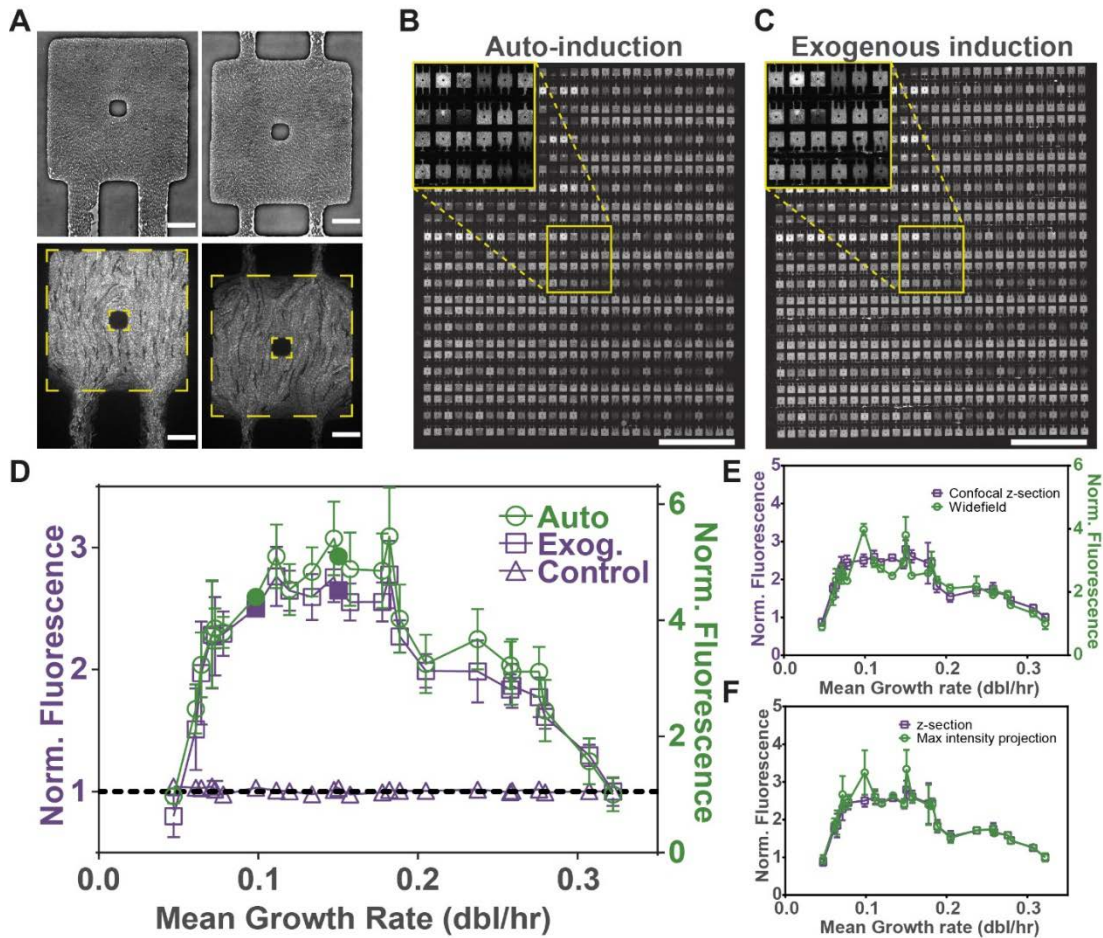


**Figure 2.5: QS response magnitude are non-monotonic functions of diffusive coupling to the environment.** **A**, Phase contrast and fluorescence micrographs of auto-induced QS response within a single-sided and a double-sided chamber in tryptone medium at 25°C. Scale bars, 20  $\mu\text{m}$ . **B,C**, Fluorescence micrographs of chamber array taken 24 hours after (B) auto- and (C) exogenous (1  $\mu\text{M}$  AI) induction. Insets contain magnified view of the region indicated, which contains all 24 chamber configurations. Scale bars, 1 mm. **D**, Distributions of QS response after 24 hours in auto-induction, exogenous induction, and inhibitory (control) conditions. (n=105 or n=60, for single- or double-sided chambers, respectively, from 3 independent experiments). Filled shapes indicate the 2 chamber types excluded from this analysis due to partial formation of cell bilayer. **E**, QS response distributions after 24 hours in exogenous induction conditions in tryptone medium at 25°C from confocal z-section (n=2) and widefield images (n=105 or n=60, for single- or double-sided chambers, respectively, from 3 independent experiments). **F**, QS response distributions after 24 hours in exogenous induction conditions in tryptone medium at 25°C from confocal z-section and confocal maximum intensity projections (n=2). (mean  $\pm$  SD)

the most AI and would be expected to have the highest level of response. Therefore, neither the traditional Density Sensing nor the alternative Diffusion Sensing interpretations could fully account for the QS responses we observed. Indeed, all chambers contained equally dense cells populations and were supplied with the same saturating amount of exogenous AI, and yet the QS induction displayed complex non-monotonically distributed response patterns. Thus, differential chamber access must be governing additional factors which contribute to the regulation of the QS response. We next set out to determine the mechanism of this complex QS dependence and the details of its unfolding in time and space.

### **2.2.5: Response dynamics is reflective of environmental conditions**

Despite the similarities between the final biphasic response distributions of the two induction methods, which are also observed readily by examining the distribution of normalized QS response intensities at the 24 hour mark from the signal of whole chambers obtained with widefield epifluorescence microscopy, as well as of a single slice of the chamber obtained with confocal microscopy (Figure 2.5E), the response dynamics obtained from time-lapses from the former does reveal very important distinctions between auto and exogenous inductions that may uncover the source of the discrepancy in the QS response between the different chamber configurations. Firstly, exogenously induced colonies (Figure 2.6A) exhibit a QS response much sooner ( $1.71 \pm 0.47$  hours) than the auto-induction case (Figure 2.6B), which display a noticeable lag time ( $10.97 \pm 2.69$  hours) between glucose removal and QS response onset, perhaps suggesting the lack of components as the reason of the delay. However, it is not surprising that exogenous

induction is much faster than auto-induction, since the QS response is dependent on AI, so the availability of saturating levels of AI in the exogenous case would certainly allow LuxR-AI complexes to be made almost immediately and initiate the QS response, even if LuxR levels are very low. This is in contrast to auto-induction, in which levels of AI do not ramp up until induction has occurred in at least some of the cells such that positive feedback-dependent LuxI production can occur and promote induction throughout the population.

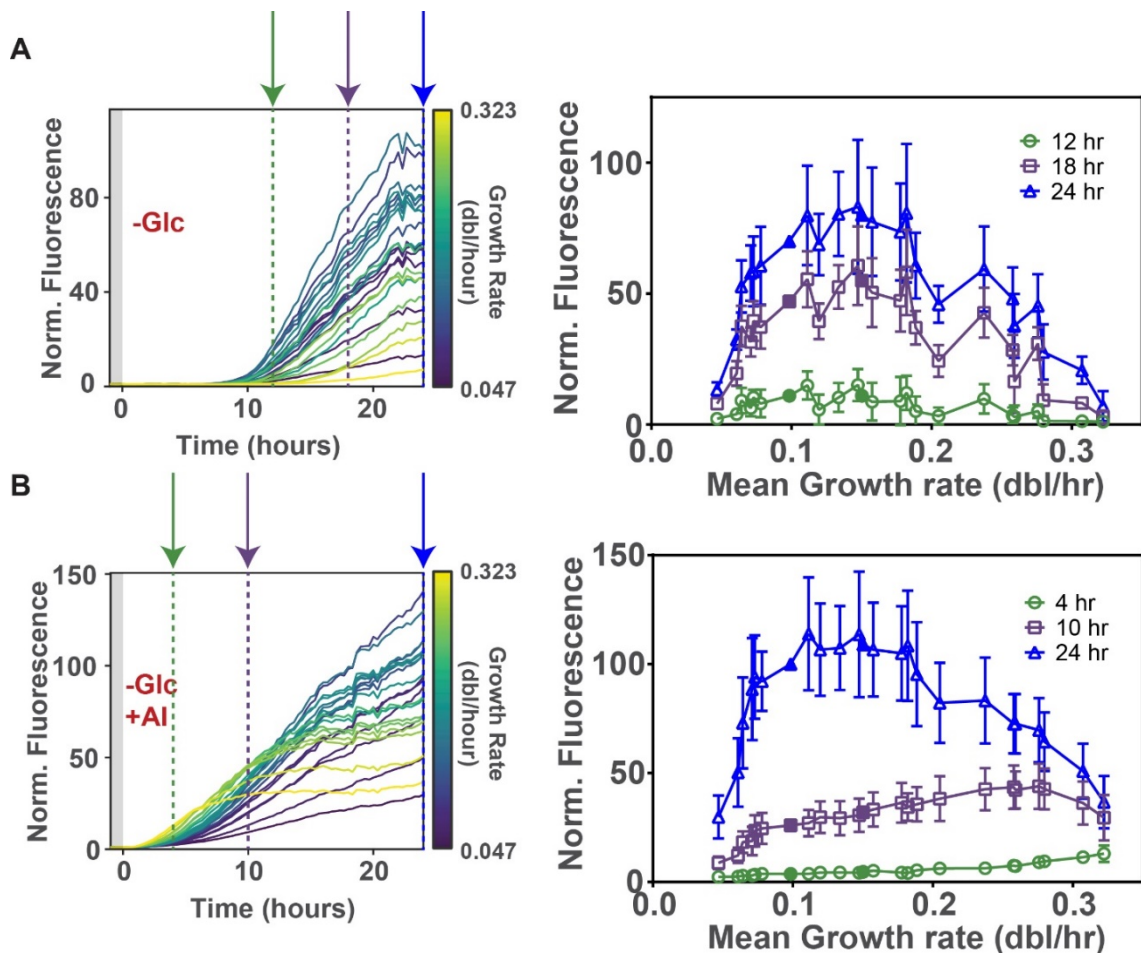


**Figure 2.6: Evolution of QS dynamics in tryptone medium at 25°.** A,B QS response dynamics and distributions of QS response at various time points in (A) auto- and (B) exogenous induction conditions in tryptone medium at 25°C ( $n = 6$ , from 3 independent experiments) (mean  $\pm$  SD). Filled shapes indicate the 2 chamber types excluded from this analysis due to partial formation of cell bilayer.

Secondly, comparisons of the response traces between the different induction scenarios post-onset demonstrated different behavior. In auto-induction, intermediate growth rate chamber configurations maintained the highest response rate throughout, while in exogenous induction, the chamber configuration with the highest growth rate exhibited the highest initial response rate, but also plateaued first at the lowest steady state level. This is best exemplified by comparing the distributions of the normalized QS response intensities of the different chambers at various time points, where the response is vastly different between auto and exogenous induction even though they are both biphasic at the 24-hour mark. For example, in auto-induction, the distribution of the normalized QS response intensities appears to be biphasic throughout the entire time of capture, from approximately 2 hours after the onset of the first chamber type at the 12-hour mark to the endpoint at the 24-hour mark (Figure 2.6A). On the other hand, the distribution of the normalized QS response intensities in exogenous induction changes through time (Figure 2.6B). Approximately 2 hours after the onset of the first chamber type at the 4-hour mark, the distribution of the normalized QS response intensities is monotonically increasing, with the chamber with the highest growth rate exhibiting the highest level of response. At the 10-hour mark, most of the chambers still exhibit a monotonically increasing dependence, but the peak of the response distribution has shifted to a chamber with a slower growth rate, beyond which the chambers with faster growth rates exhibited a monotonically decreasing dependence of response level on growth rate. The shift is caused by the chambers with the highest growth rates approaching a steady state level of response, while the response level in chambers with slower growth rates continue to rise. By the end of the 24-hour mark, the distribution of the normalized QS response intensities has morphed into

a biphasic distribution, due to more of the chambers with higher growth rates approaching or reaching steady state, while chambers with lower growth rate continue to increase in response level, shifting the peak of the distribution further to slower growth rates.

While the distribution of responses in auto-induction was relatively static through time, the distribution of responses in exogenous induction was extremely malleable, demonstrating shifts in the peak response from higher growth rates to lower growth rates through time. The dynamical shift in the peak of the distribution supports the idea of QS regulation by two opposing forces, since the response distribution initially exhibits a positive correlation between response level and growth rate, but the negative correlation between response level and growth rate emerges, as evident by the peak shift and a transition to a biphasic response. The plasticity in response distribution of exogenous induction suggests that if the regulation of the QS response is indeed dependent on two opposing forces, it would be manifested in rates of processes governing the dynamics of the system, which enabled the system to achieve the same state as auto-induction, albeit transiently, despite different initial distributions.

#### **2.2.6: Response dynamics is modulated by balance of synthesis and dilution**

Analyzing the rate of increase in the QS response in exogenous induction for a period of 5 hours after onset has occurred, which is reflective of LuxI synthesis, revealed a monotonically increasing dependence on growth rate, in agreement with the positive correlation observed between QS response and growth rate (Figure 2.7B, C). However, in contrast with the transition to a more biphasic dependence as seen in the distribution of



responses, the monotonically increasing distribution of induction rates is likely to remain static with time, since the positive feedback in the circuit is expected to be maintained given the sustained saturating levels of exogenous AI in this scenario. Also, we do not believe that chambers with slower growth rates have lower induction rates as a result of reduced AI diffusion, since the time-scale of diffusion is much shorter than the timescale of fluorescence increase, so AI should have reached high enough levels in less than 15

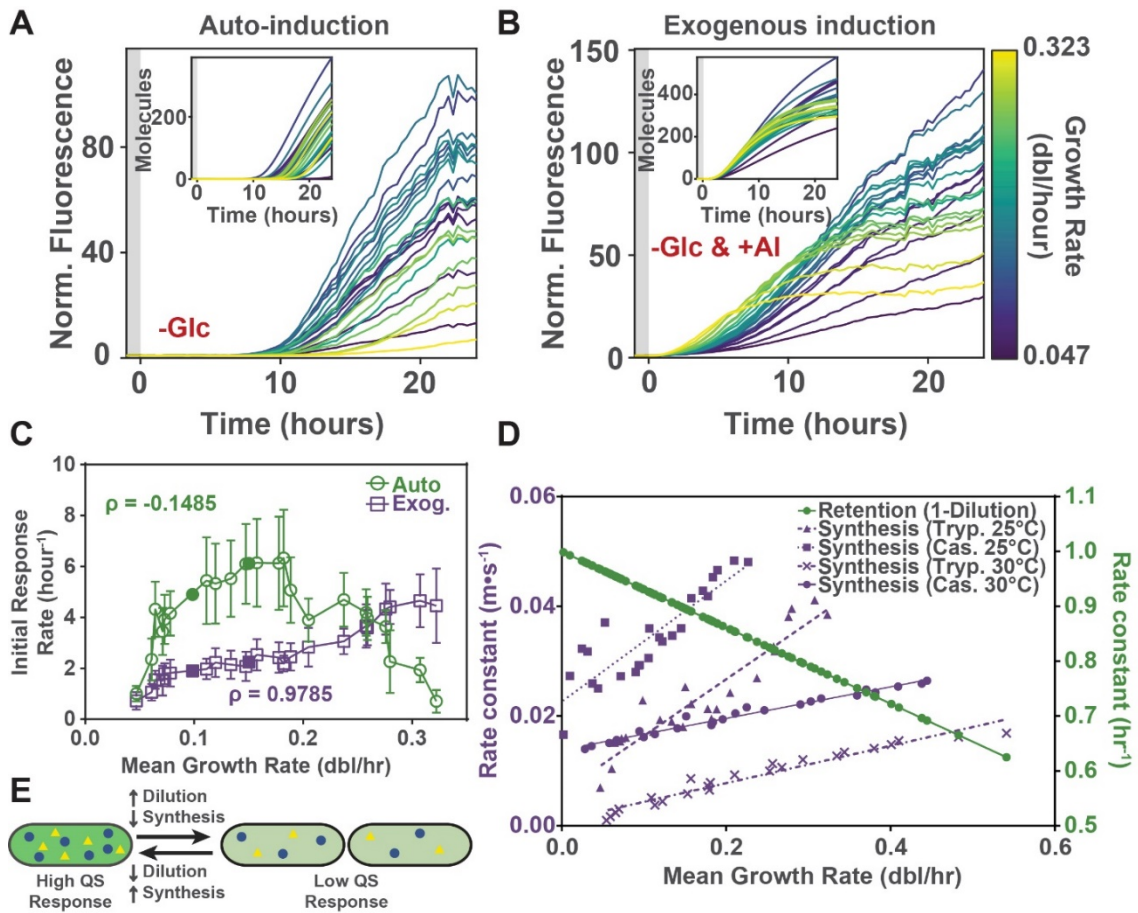


**Figure 2.7: Response dynamics governed by balance of synthesis and dilution.** **A**, **B**, Response dynamics over 24 hours in **(A)** auto- and **(B)** exogenous induction conditions. ( $n = 6$ , from 3 independent experiments). Inset in graph contains simulated dynamics. **C**, Distribution of initial QS response rates in auto- and exogenous induction. ( $n = 6$ , from 3 independent experiments). Filled shapes indicate the 2 chamber types excluded from this analysis due to partial formation of cell bilayer. (mean  $\pm$  SD) **D**, Measured and inferred synthesis and dilution (growth) rate constants from various environmental conditions. **E**, Diagram of proposed mechanism regulating QS dynamics.

minutes to saturate the response even in the most restricted chamber type. Thus, the maximum rate of QS response induction has a monotonically increasing relationship with growth rate, and by extension, with the diffusive coupling which affects nutrient access. A possible source of this monotonically increasing relationship between maximal induction rate of QS response and growth rate could be an increase in protein synthesis rate, for example, of QS components such as LuxI, which might be facilitated by the additional access to nutrients in higher growth rate chambers. A similar analysis performed for the initial rate of change in the QS response for auto-induction revealed a distribution of rate of induction of the QS response that is biphasic, which is in agreement with the distribution of QS responses (Figure 2.7A, C). Thus, the robustness of the biphasic QS response distribution appears to stem from the biphasic distribution of induction rate, coupled with non-steady state conditions. However, the biphasic response distribution can still be explained by the monotonically increasing synthesis rate distribution, which will be discussed later.

Although there is a monotonically increasing dependence of induction rate on growth rate that imparts the chamber with fastest growth the highest induction rate in exogenous induction, the transition in the QS response distribution from monotonically increasing to biphasic suggests there is an inverse component that acts in an opposing manner. This results in the dynamics of the fastest growing chamber type to also have the greatest loss of signal and lowest steady state level, implying that this additional set of rates monotonically decreases with increasing growth rate. Since this monotonically decreasing relationship does not arise until after onset has occurred, it implies that the QS-averse

mechanism could be concentration dependent. One process that is negatively correlated with growth and is also concentration dependent is the retention rate of protein during cell division. Previous work has demonstrated that protein concentration decreases monotonically with increasing growth rate due to higher protein dilution as a result of increased cell division [82]. The dilution of a component of QS, such as LuxR, through cell division in higher growth chambers could adversely affect the ability of a cell to initiate or maintain a QS response, while growth in chambers with less nutrient access could help with retention of the QS components that promote a QS response (Figure 2.7D).

### 2.2.7: Analysis of the balance of synthesis and dilution to understand QS dynamics

We hypothesize that the balance of the synthesis and dilution of QS proteins could be the governing forces behind the modulation of QS response dynamics (Figure 2.7E), but first, we attempted to further understand analytically how a monotonically increasing synthesis rate coupled with a monotonically decreasing retention rate might combine to recreate the biphasic response distribution by examining the equation that govern the dynamics of GFP production and loss. The governing equation for the rate of change of GFP, which is very similar to that for LuxI (since the two genes are under the same promoter), is

$$\frac{d[G]}{dt} = c_{0I} + \frac{k_{synI}[C]}{K_{DI} + [C]} - k_{dil}[G] - k_{degG}[G] \quad (1)$$

where G is GFP and C is the LuxR-AI complex dimer that binds to Lux box region of the DNA to affect changes in gene transcription behavior. The first term represents the

constitutive production rate of G, which is a constant. The second term represents the production of G due to positive feedback, which has been modeled with Michaelis-Menten enzyme kinetics by substituting the DNA/transcription/translation machinery for the enzyme and C for the substrate. The third term represents loss of G due to dilution from cell division, and the fourth term represents loss of G due to degradation. At the onset of the exogenous induction response, the contribution to the overall rate by the dilution and degradation terms would be negligible, since there is no production of GFP yet beyond basal concentrations, which is lower than what we could detect with fluorescence microscopy. The onset of the exogenous induction represents the induction of the GFP production by the positive feedback, which is expected to be much greater than the constitutive production, rendering the constitutive production term also negligible, leaving only the positive feedback term. However, because it is exogenous induction, a saturating level of AI is available, so all LuxR is presumably converted into the complex, which allows us to assume  $[C] \gg K_{DI}$ . This results in

$$\frac{d[G]}{dt} = k_{synI} \quad (2)$$

which suggests that the rate of GFP production at the onset of exogenous induction is the maximal rate of the positive feedback production of GFP and was measured to be a monotonically increasing function with respect to growth rate. At steady state, the rate of change of GFP is equal to 0. Since it is exogenous induction, we again assume  $[C] \gg K_{DI}$ , as well as the production by the positive feedback is expected to be much greater than the constitutive production, rendering the constitutive production term negligible. We are also

using a very stable form of GFP, so loss of GFP via degradation is also assumed to be negligible. Rearranging to solve for G gives

$$[G] = \frac{k_{synI}}{k_{dil}} \quad (3)$$

at steady state. Since  $k_{synI}$  is monotonically increasing with increasing growth rate, and from the exogenous induction dynamics, for the traces that have reached steady state, we know that G decreases with increasing growth rate. Therefore, if the equation is to reproduce the dynamics,  $k_{dil}$  must also be a monotonically increasing function with increasing growth rate. However, since thinking about protein concentration in terms of what is retained, instead of what is diluted, makes it easier to compare to what is synthesized, we will discuss the effect of dilution in terms of retention from henceforth. Since retention is the opposite of dilution, retention would be a monotonically decreasing function with increasing growth rate. This analysis does indeed suggest that a monotonically increasing synthesis rate coupled with a monotonically decreasing retention rate can reproduce the dynamics of the exogenous induction. A similar simplified analysis might also explain a potential origin of the biphasic distribution of rate of change of GFP at the onset of auto-induction. Similar to the onset of exogenous induction, the contributions of the first, third, and fourth terms are assumed to be negligible for identical reasons. However, since auto-induction relies on the endogenously produced AI to activate the positive feedback, the concentration of C at onset is expected to be low, since there is no saturating level of AI to convert all of the LuxR to C. Therefore, we assume  $K_{DI} \gg [C]$ , so the rate of change of GFP is governed by

$$\frac{d[G]}{dt} = \frac{k_{synI}[C]}{K_{DI}} \quad (4)$$

where  $k_{synI}$  is a monotonically increasing function with increasing growth rate, and C is a protein, so its levels are assumed to be regulated by the dilution, making it a monotonically decreasing function with increasing growth rate. The multiplication of monotonically increasing and monotonically decreasing functions can result in a biphasic-like curve, which might provide one possible explanation, albeit an extremely simplified one, of how a biphasic curve could arise at the onset within the specific conditions that we used.

### **2.2.8: Mathematical model of QS dynamics**

We hypothesized that the interplay between LuxI synthesis rate and protein retention rate, varying in a monotonically increasing and a monotonically decreasing manner, respectively, relative to growth rate as a result of the differences in diffusive coupling, contributed to the biphasic response and dynamics observed in both induction methods. To test the hypothesis, we modified previously published mathematical models of QS response to incorporate direct experimental measurements of synthesis and dilution parameters [83, 84]. Specifically, the synthesis rate we modulated is the LuxI feedback synthesis rate, since analysis of the equations suggests this is the term that would be modulated in exogenous induction onset. Also, presence of positive feedback in the synthesis rate makes it much more sensitive to perturbations since any changes will be amplified substantially. The

retention rate was modeled to affect all protein species. We found that training the model with previously published and newly measured parameters for the tryptone medium at 25°C condition successfully reproduced the QS dynamics, namely, the delay in the time of the onset of a QS response in auto-induction, as well as the rates and intensity distributions at both the onset and the 24-hour mark and for both auto and exogenous inductions (Figure 2.7A, B). The reproduction of onset time is particularly interesting, since the process of model creation did not take into account the onset time, suggesting that perhaps onset time is governed by the same process behind the modulation of response dynamics. These results suggest that dynamics, as regulated by a balance of synthesis and dilution, might hold the key to understanding the regulation of the QS response, and in particular, the temporal dependence of QS onset. Since differential diffusive coupling, which modulate nutrient access, was shown to alter the QS response, we next tested if the model will be predictive for another source of nutrients.

### **2.2.9: Medium composition changes synthesis and dilution rates**

To vary the medium composition, we replaced tryptone in the original medium, which is obtained via the digestion of casein by trypsin, with casamino acids, which is obtained by acid hydrolysis of casein (Figure 2.8). Tryptone tends to be composed mainly of an assortment of oligopeptides, while casamino acids tend to have predominantly free amino acids. Growth in casamino acids-based medium had overall slower measured growth rates than in tryptone medium, but the measured synthesis rates are overall higher, which might suggest a reallocation of resources from production of proteins for growth to production of proteins for other functions (Figure 2.7D). Regardless of the mechanism, inputting

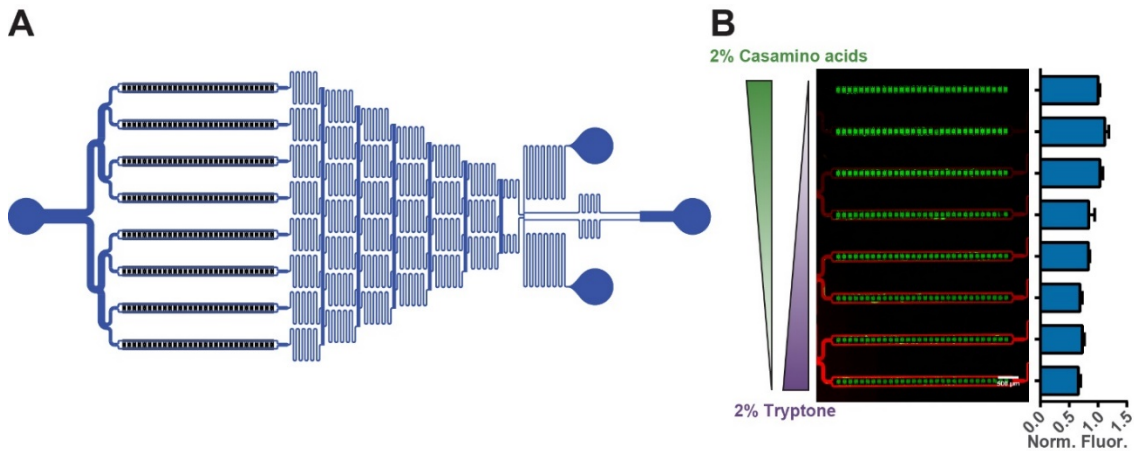


**Figure 2.8: Juxtaposition of nutrient conditions within gradient-generating device.**

**A**, Diagram of gradient-generating microfluidic device with a singular chamber configuration (highest diffusive coupling). **B**, Fluorescence micrograph and response distribution of exogenous induction in opposing tryptone and casamino acids gradients at 25°C (n=30). Scale bar, 500  $\mu\text{m}$ . (mean  $\pm$  SD)

decreased growth rates and increased synthesis rates into the model and simulating auto-induction conditions predicted an earlier onset time as compared to tryptone medium, and a biphasic response distribution both at the onset and after 24 hours (Figure 2.9A). However, the intensities of the response distribution after 24 hours in casamino acids medium are more narrowly distributed, suggesting a more homogeneous response level between the different chamber configurations, as compared to the tryptone medium. The experimental dynamics of auto-induction in casamino acids medium confirmed the predictions made by the model, demonstrating a dramatically earlier onset time ( $4.52 \pm 1.35$  hours), along with biphasic response distributions that are much narrower than that in tryptone medium (Figure 2.9A). The homogeneity of the response between chamber configurations can also be observed in the fluorescence micrograph (Figure 2.9B). In the case of exogenous induction in casamino acids medium, the model predicted slightly higher rates of increase at onset, but otherwise a similar onset time as exogenous induction in tryptone medium (Figure 2.9C). Also, the response distributions at onset and after 24 hours



are similar to exogenous induction in tryptone medium, where the maximum rate of synthesis has a monotonically increasing dependence on growth rate at onset, but evolves into a biphasic response after 24 hours. Like the casamino acids auto-induction case, the distribution of responses is narrow. Compared to the experimental results, the model predictions faithfully reproduced the features of the dynamics, such as onset time and response distributions at onset and after 24 hours (Figure 2.9C). The response profile also looks similar to auto-induction (Figure 2.9D), with comparable response distributions (Figure 2.9E). However, the difference between the two induction methods is still reflected in the dynamics (Figure 2.9F), where the intensity distributions at different time points

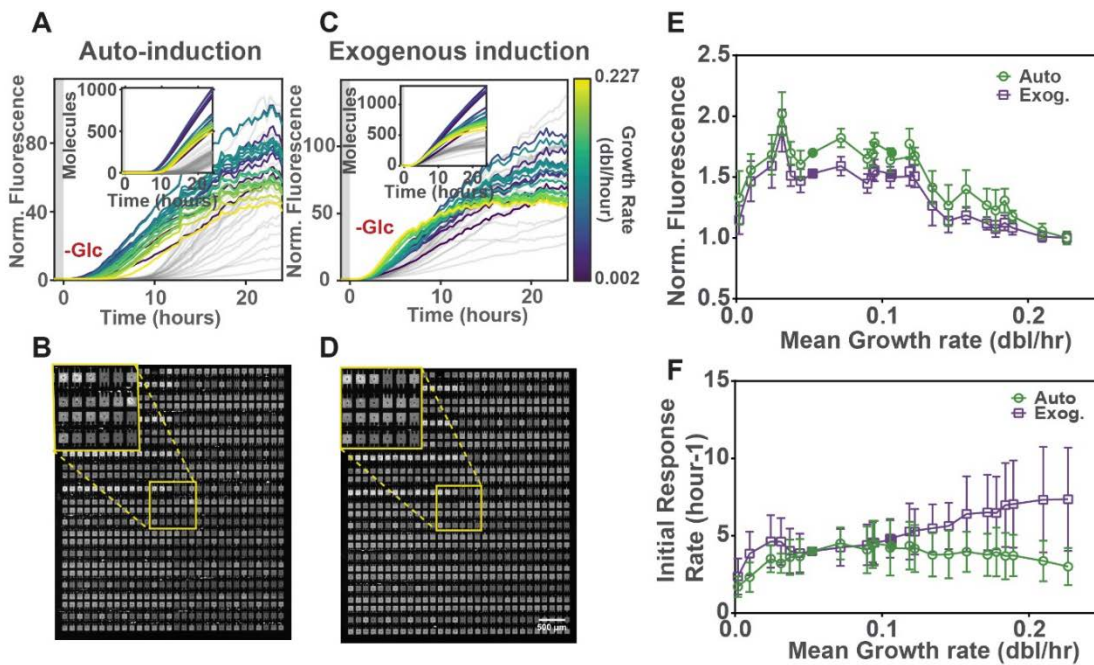


**Figure 2.9: QS response dynamics in casamino acids medium at 25°.** A-D, Response dynamics and fluorescence micrographs of (A, B) auto- and (C, D) exogenous inductions in casamino acids medium at 25°C, respectively, with induction within tryptone medium at 25°C shown in gray ( $n = 6$ , from 3 independent experiments). Insets are the simulated dynamics. Scale bar, 500  $\mu\text{m}$ . E, Distribution of QS response after 24 hours in auto- and exogenous, induction conditions in casamino acids medium at 25°C. ( $n=105$  or  $n=60$ , for single- or double-sided chambers, respectively, from 3 independent experiments). F, Distribution of initial QS response rates in auto- and exogenous induction in casamino acids medium at 25°C. ( $n = 6$ , from 3 independent experiments). Filled shapes indicate the 2 chamber types excluded from this analysis due to partial formation of cell bilayer. (mean  $\pm$  SD)

mirrored the differences in the tryptone condition (Figure 2.10A, B). Both the experiment and simulation results suggest that a switch to medium with slower growth rates decreases the time to onset in auto-induction, and homogenizes the response between chamber configurations, potentially as a result of increased LuxI synthesis rates or increased QS component retention rates as a result of reduced growth and dilution. Since both of these lead to increase in QS components, through increases in AI production or LuxR levels, it is possible that the regulation of the QS onset time would depend on the accumulation of LuxR to a level sensitive to the local AI concentration. The reduction in growth rate might

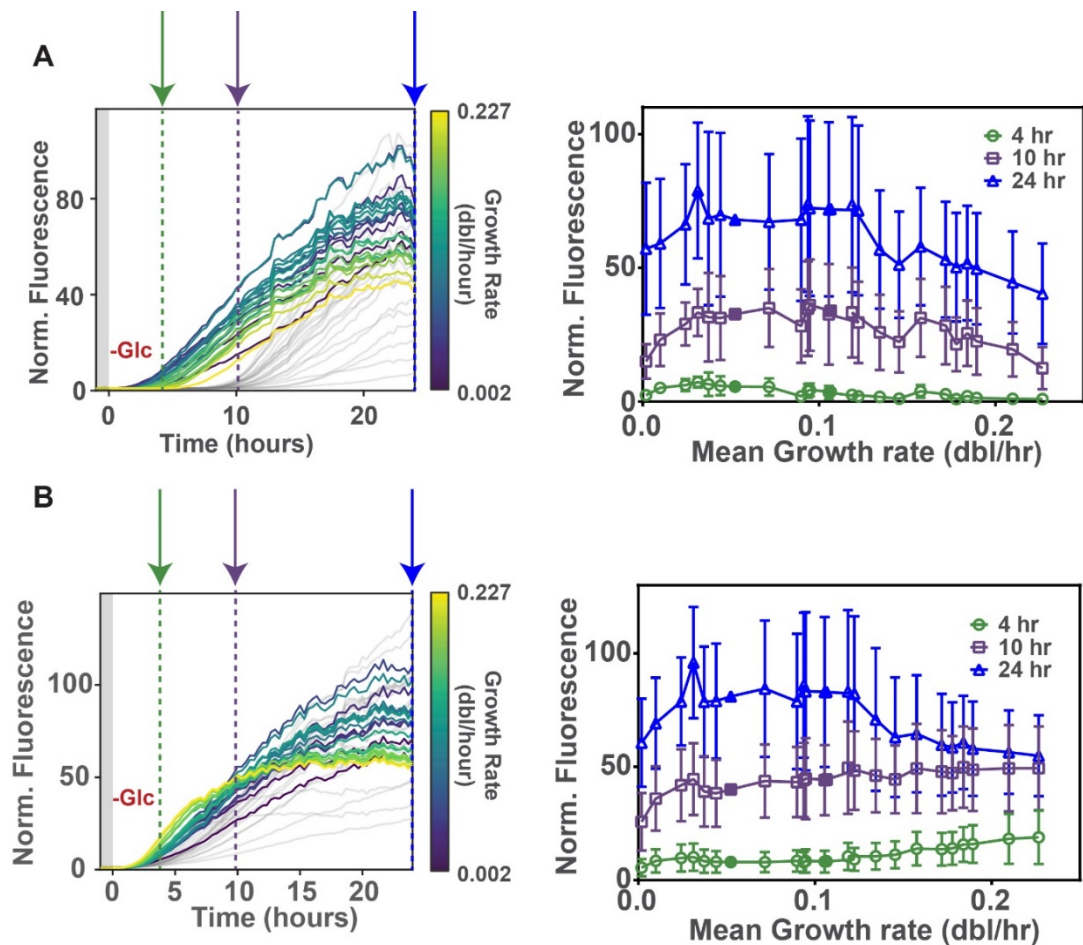


**Figure 2.10: Evolution of QS dynamics in casamino acids medium at 25°.** A, B QS response dynamics and distributions of QS response at various time points in (A) auto- and (B) exogenous induction conditions in casamino acids medium at 25°C (n = 6, from 3 independent experiments) (mean ± SD). Filled shapes indicate the 2 chamber types excluded from this analysis due to partial formation of cell bilayer.

also aid in the reduction of consumption rate of the nutrients, allowing diffusion to create a more uniform nutrient profile between the chamber configurations, thereby minimizing the effects of differential diffusion between different chamber configurations. Nevertheless, the switch to another medium also demonstrates that the different diffusive coupling serves to modulate the nutrient access by the cells, which then defines the response levels. The chamber geometry itself does not dictate the behavior of the cells, since the same chamber type in different media conditions can have different dynamics and response levels.

#### **2.2.10: Temperature changes synthesis and dilution rates**

If the QS response dynamics is indeed defined predominantly by the growth-mediated balance of synthesis and dilution, then non-nutrient-based perturbations to the environment that affects growth should also alter the dynamics of QS response. Temperature can have a tremendous effect on the growth rate even within the same nutrient conditions, so we chose to perturb the temperature to examine its effects on the QS response. By increasing the temperature to 30°C, the measured growth rates for the tryptone and casamino acids media extended to higher levels as compared to the previous temperature of 25°C (Figure 2.7D). The synthesis rates at 30°C were inferred by comparing the differences in measured synthesis rates at 25°C between the two media conditions relative to the change in measured growth rates, and extrapolating that relationship to determine the change in synthesis rates from 25°C to 30°C based on the corresponding change in measured growth rates within each medium condition (Figure 2.7D). By simulating with the parameters for synthesis and growth rate at 30°C, we were able to obtain predictions regarding the

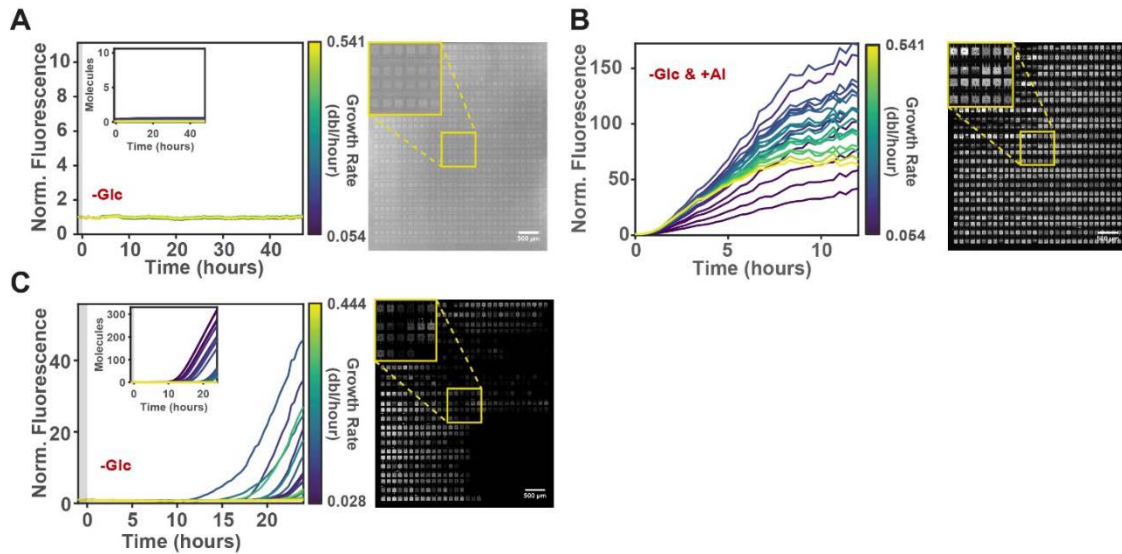


**Figure 2.11: QS dynamics within various conditions at 30°C.** A-C, Response dynamics and fluorescence micrograph of various conditions: (A) Auto-induction in tryptone medium at 30°C, (B) Exogenous induction in tryptone medium at 30°C, and (C) auto-induction in casamino acids medium at 30°C (n = 6, from 3 independent experiments). Insets in graphs contain simulated dynamics. Insets in fluorescence micrographs contain magnified view of the region indicated, which contains all 24 chamber configurations. Scale bars, 500  $\mu\text{m}$ .

dynamics at the elevated temperature. At 30°C in tryptone medium, simulations indicate there is no onset of the QS response in any of the chambers even after an extended period of 49 hours (Figure 2.11A). This result is in agreement with experiments, since no QS response was detected in any chamber in tryptone medium at 30°C (Figure 2.11A). This result is similar to the situation where cells are grown in tryptone medium with 20 mM glucose at 25°C, where there is no detectable onset of the QS response. However, that is due to the direct repression of the QS response via the suppression of LuxR transcription, which involves the CRP-cAMP complex. The presence of 20 mM glucose prevents the production of high levels of cAMP, thus minimizing the activation of catabolic genes by CRP. In the situation of tryptone at 30°C, however, there is no direct repression of LuxR or any other QS component at the transcription, translation, or post-translational level. In fact, the QS response is not directly suppressed, as visualization of the time-lapse images

reveals that individual cells stochastically exhibit onset of a QS response. However, these single cells are not able to influence the onset in other cells, and the response gradually declines to undetectable levels as the cell divides and dilutes the QS response machinery. Furthermore, addition of exogenous AI in tryptone medium at 30°C is able to induce complete onset of the QS response in all of the chamber configurations, suggesting that there is no direct repression of the QS response at 30°C since basal levels of LuxR are sufficient for the induction of QS response in the presence of exogenous AI (Figure 2.11B). Yet, the conditions in tryptone medium at 30°C remains uncondusive to an auto-induced QS response, whereas at 25°C in the same medium, all the chambers exhibited a QS response. This suggests that growth medium alone is not predictive or representative of the QS response, and other factors, such as temperature can dramatically affect the probability of QS onset.

Since growth in tryptone medium at 30°C is uncondusive to an auto-induced QS response, we wondered if the growth-mediated modulation of synthesis or dilution is affecting the onset, and if so, whether it is possible to rescue the response by reverting back to slower growth conditions while maintained at the elevated temperature. Within the simulation, this was done by reducing the dilution rates and increasing the synthesis rates to that corresponding to casamino acids medium, which would replicate a switch to the slower growth medium. Inputting these parameters into the mathematical model gave a prediction that only a subset of chamber configurations will respond within a 24-hour period, with the intermediate growth rate chambers responding the soonest, despite an overall significant lag period of a little more than 10 hours, which is similar to, but still slower than, the auto-

induction response in tryptone medium at 25°C (Figure 2.11C). Indeed, by experimentally switching to casamino acids medium at 30°C, we were able to obtain an onset of a QS auto-induced response in some, but not all, of the chamber configurations (Figure 2.11C). This implies that it is not temperature, medium composition, nor the nutrient access as dictated by the capillary configuration that defines the QS response, but what they in turn regulate, which is the QS protein accumulation via the balance of synthesis and dilution.

### **2.2.11: Changes in synthesis and dilution affects QS protein accumulation**

Manipulation of both the medium composition and temperature have modulated the dynamics of the QS response in a predictable manner, which supports the idea that these conditions are, in actuality, modulating the rates of synthesis and retention, and therefore, affecting the accumulation of QS proteins which ultimately govern the response. However, changes in medium composition and temperature have wide-ranging effects within the cell, which, combined with the inability to decouple the simultaneous modulation of synthesis and dilution rates, makes the origins of dynamics modulation unclear. We wanted to explore whether direct manipulation of the accumulation of a single QS protein would alter QS dynamics, and in particular, the onset time, in a similar predictable fashion. Exposure to exogenous AI, which has the same effects as LuxI overexpression, has already been shown to be effective in reducing the onset time, but we would now like to overexpress LuxR, which is the cytoplasmic protein receptor that initiates changes in gene expression behavior when the presence of AI is detected. Since the effects of LuxR is more confined to the host cell (activation of positive feedback and production of GFP), whereas the effects of LuxI are more global (the AI produced diffuses out and affects other cells), LuxR plays

a defining role in a cell's sensitivity to the presence or absence of a signal, and its decision to respond or not. Overexpression of LuxR is expected to increase its accumulation and accelerate QS response. We overexpressed LuxR by putting a copy of the gene on a low copy plasmid (in addition to the genomically integrated copy) under the control of a *tac* promoter, the expression of which can be induced with IPTG (Figure 2.12A). Since the copy of the LuxR gene on the plasmid is not under the control of CRP-cAMP, the presence of glucose does not suppress the response, so the cells are unrestricted in their ability to respond.

Simulation of the overexpression of LuxR was performed by increasing constitutive and feedback production of LuxR by a factor of 10 as compared to the regular uninhibited

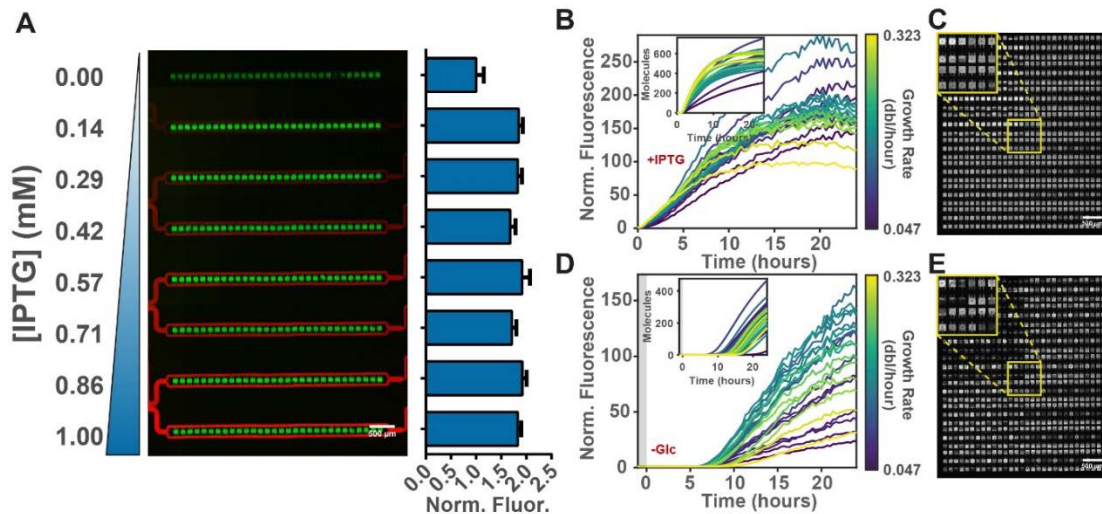


**Figure 2.12: QS dynamics of LuxR perturbations.** **A**, Fluorescence micrograph and response distribution of auto-induction of an IPTG-inducible overexpression strain in 0-1 mM IPTG gradient at 25°C (n=30). Scale bar, 500  $\mu$ m. (mean  $\pm$  SD) **B-E**, Response dynamics and fluorescence micrograph of various conditions: (**B,C**) auto-induction of overexpression capable strain in tryptone medium with 1 mM IPTG at 25°C, and (**D,E**) auto-induction in tryptone medium with an initial 10 mM glucose at 25°C (n = 6, from 3 independent experiments). Insets in graphs contain simulated dynamics. Insets in fluorescence micrographs contain magnified view of the region indicated, which contains all 24 chamber configurations. Scale bars, 500  $\mu$ m.

levels to replicate the increased copy number and higher levels of transcription, but utilizing the same LuxI synthesis and dilution rate constants from tryptone medium at 25°C. Doing so produced response dynamics that were similar to that from exogenous induction of WT cells in casamino acids medium at 25°C, with the exception of a much sharper initial response rate increase. The onset time was also comparable, with a near instantaneous induction (Figure 2.12B). Experimental validation with IPTG (1 mM)-induced LuxR overexpression in tryptone medium at 25°C produced response dynamics that were indeed similar to the experimental dynamics of exogenous induction in casamino acids medium at 25°C (Figure 2.12B). The experimental dynamics had a high initial increase in the response, and resulted in a higher and more uniform level of induction, which is also visible in the fluorescence micrographs (Figure 2.12C). This demonstrate that increased synthesis could have equivalent effects as a reduction in dilution, because they both lead to the increased accumulation of the protein. The much earlier onset time of ( $0.64 \pm 0.22$  hours) in the overexpression case as compared to the non-overexpression case within the same medium and temperature conditions suggest that the additional LuxR imparted by the extra copies of the gene enhanced the accumulation rate of LuxR, making it much more sensitive to the same AI levels than non-overexpressed conditions and enabling the cells to initiate a QS response sooner.

Since the degree of overexpression of LuxR was difficult to control precisely, coupled with the extreme sensitivity of the promoter to even very small increases in LuxR levels due to activation of the positive feedback, this method of manipulating the concentration of LuxR can only be used to examine the two opposite extremes on the spectrum of responses, but



cannot be used to tease out the effects of small changes in LuxR levels. However, since overexpression is a modulation of the rate, if we can modulate the initial concentration instead, but maintain the same rate during induction, perhaps the onset time can be reduced without affecting the rest of the QS dynamics (rate of increase). If onset is dependent on the accumulation of LuxR to a critical level such that it is sensitive to the local AI concentration, then, given identical local AI concentrations but different initial LuxR levels, the time to onset would vary. A method to finely tune the level of initial LuxR could be through glucose concentration during growth. A reduction in glucose concentration during growth (20 to 10 mM) is assumed to repress the promoter to a lesser extent, but still enough to suppress the onset of the response, resulting in higher initial LuxR levels. Once glucose is completely removed, the onset time would presumably occur earlier due to higher initial LuxR levels, thereby requiring less AI buildup and time to become induced, but the rate of production will be identical to the previous cases. Higher initial LuxR expression conditions were simulated by interpolating the midway point between the expression levels at 20 mM and 0 mM. Simulation using the interpolated parameters resulted in slightly earlier onset time, but otherwise unchanged dynamics (Figure 2.12D). Experimental validation showed that the reduction in onset time is even more significant ( $7.51 \pm 1.56$  hours) than the model had predicted, suggesting that the relationship between glucose concentration and LuxR expression is not linear and that the model had overestimated the degree of repression (Figure 2.12D). However, it did verify that the dynamics and response profiles were essentially unchanged after induction occurred (Figure 2.12E), as compared to the induction from initial growth at 20 mM glucose, suggesting different aspects of QS dynamics are selectively affected by changes to initial concentration and synthesis rates.



### 2.2.12: Information theoretic analysis of QS sensitivity to environmental conditions

Since the QS dynamics from the numerous different conditions we tested were all quite different from each other, we wondered if the dynamics are an accurate reflection of the conditions the cells are exposed to, and if an analysis of the dynamics would reveal the ability by the cells to distinguish the different environments. By focusing on three aspects of the dynamics (Figure 2.13A), namely onset time, initial response rate, and 24<sup>th</sup>-hour response magnitude, we saw that different aspects were more adept at distinguishing the various facets of the environment (Figure 2.13B). By employing an information theoretic

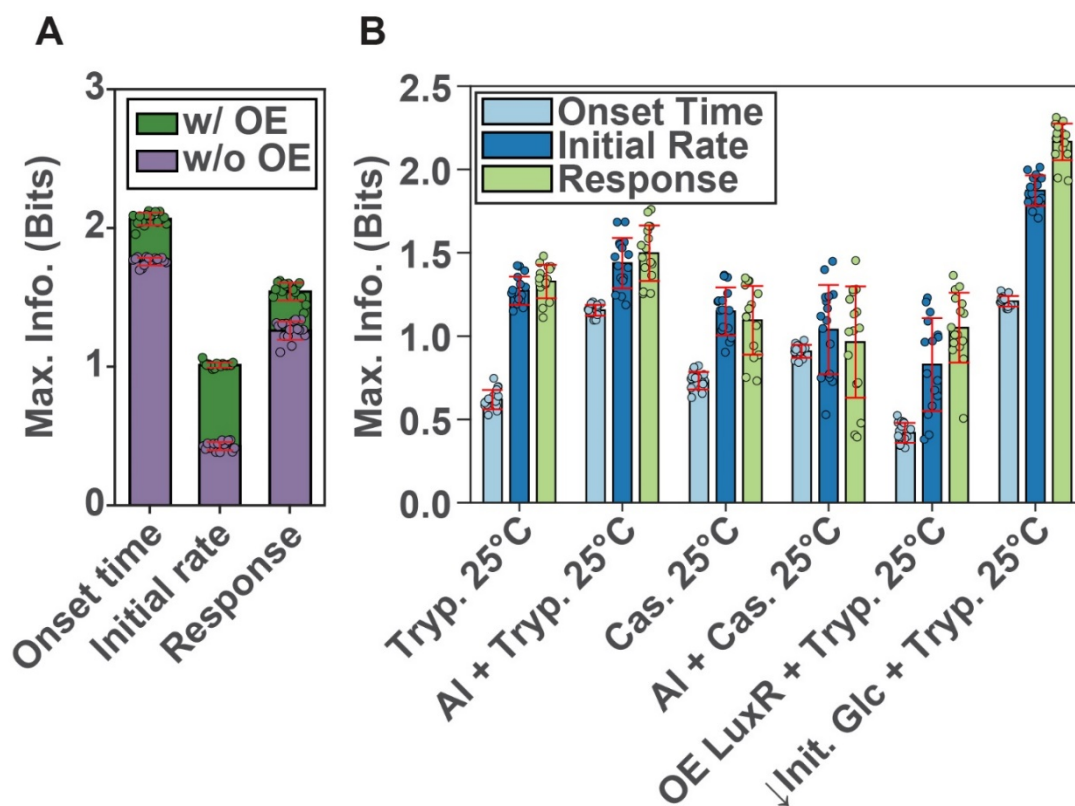


**Figure 2.14: Information theory analysis of dynamics sensitivity to environmental conditions.** **A**, Comparison of information about external environmental conditions discerned by each aspect of QS dynamics assuming all chamber configurations are equivalent. **B**, Comparison of information about the differential coupling environment discerned by each aspect of QS dynamics. (mean  $\pm$  SD)

approach [85, 86], we determined that onset time demonstrated the highest sensitivity in discriminating external environmental conditions, yielding  $1.76 \pm 0.04$  bits of information, equivalent to distinguishing  $2^{1.76} = 3.4$ , or around 3 different conditions (Figure 2.14A). The elevated sensitivity of onset time is reflective of the tight control of QS initiation, as it coincides with the checkpoint for the transition in gene expression profile. Conversely, the endpoint response magnitude is overall the most resolving of the differential diffusive coupling, with at least 1 bit of information representing the ability to distinguish at least 2 levels for each environmental condition (Figure 2.14B). However, this maximum information may be an underestimation, since the biphasic nature of the endpoint response distributions signify that two distinct growth conditions could have the same mean response magnitude, an ambiguity which the current information theoretic approach does not distinguish.

### **2.3: Discussion**

QS is one of the most ancient mechanisms of cell communication, and yet, its functional role remains ambiguous. It has been proposed that, in addition to the widely accepted cell density sensing function, QS can also serve to assess the diffusive transport properties of the microenvironment. Our results provide a more complex view of this archetypal signaling mechanism, demonstrating that QS signaling is also sensitive to various other environmental conditions such as nutrient composition and access, and temperature. Mechanistically, environmental conditions modulate the differential balance between the synthesis rates of QS network components and the growth rate of the bacterial cells, affecting overall QS dynamic behavior.

Since QS often regulates adaptive responses that counteract adverse growth conditions, the basis of the environmental dependence of QS dynamics might be rooted in the improvement in fitness that can accompany QS induction in unfavorable environments. However, a change in fitness is observed through the prism of cost and benefit of the expression of QS and its downstream proteins. The balance of metabolic expense incurred from QS induction versus growth benefits might explain the behaviors we observed, such as the variable onset time. For instance, loss of glucose from tryptone (polypeptides from casein digestion) medium may still support a high enough growth rate such that cells benefit from waiting longer before committing resources to QS onset, as the suboptimal, but still adverse condition might be transient, or perhaps the conditions can deteriorate further before adaptive responses are required. Conversely, the loss of glucose from casamino acids (free amino acids from casein digestion) medium may indicate growth-limiting conditions like high cell density that necessitate an urgent QS onset and strong adaptive response before total incapacitation occurs. This suggests that the dependence of the QS response on the environment stems from an assessment by the cells, based on the relative change in the environmental conditions, whether a commitment to initiate a QS response is worth the resource expenditures. The conclusion from the assessment would then determine the timing as well as intensity of the response. If the conditions are still relatively conducive to cell proliferation, as reflected in relatively high growth rates, the postponement of QS onset would prevent potentially unnecessary activation of adaptive responses, thereby conserving resources. The activation of adaptive responses would therefore not be initiated until suboptimal conditions have persisted long enough, or if the

conditions would demand it. On the other hand, if conditions are poor, the potential fitness advantages from a QS onset and the associated adaptive response might outweigh the investment of resources into the production of QS protein machinery, thereby promoting the earlier onset of the response.

Furthermore, since the activation of QS responses have also been shown to be reliant on the temperature in the same manner as it does on nutrient composition and access, we concluded that it was a general, over-arching growth-mediated strategy that can encompass multiple different environmental conditions. Since temperature is another factor that contributes to how conducive the environment is to growth, temperature-mediated modulation of the propensity for QS onset is congruent with the reasoning we proposed earlier with regards to the nutrient dependence. This dependence on multiple factors of the environment further affirms that this strategy is optimized for all conditions that contribute to growth, and not specific for any particular factor, such as nutrient composition, alone. This increases the versatility of QS as a mechanism for controlling the activation of adaptive responses to combat adverse conditions, since it can then be sensitive to multiple different aspects of the overall environment and take into account the current conditions for all of the environmental factors before enacting a gene expression strategy. The sensitivity of the response to the temperature also brings up an interesting point. While the QS model we are using is the *V. fischeri* QS circuit integrated into *E. coli*, temperatures optimal for *E. coli* growth is not optimal for the onset of this QS response, which is highlighted by the fact that response is absent, or severely delayed at higher temperatures (30-37°C). However, lowering of the temperature to 25°C enables the QS response to

occur, which coincides with not only suboptimal temperatures for *E. coli* growth, but also the approximate temperature at which *V. fischeri* resides within the light organs of Hawaiian bobtail squids off the shores of Hawaii. The increased propensity for QS responses in suboptimal conditions further supports the idea that QS mechanisms can be used to regulate adaptive responses.

## 2.4: Experimental methods

### 2.4.1: Bacterial strain and growth conditions

MG1655 *E. coli* expressing a truncated LuxIR QS operon from *V. fischeri* made in a previous study [73] was used. Briefly, MG01S, containing *luxR* divergently transcribed from *PluxI* fused to *GFP*, and MG02S, which is identical to MG01S bar the addition of *LuxI* upstream of *GFP* and under the same promoter, were made by the restriction digests of *EcoRI-KpnI* and *EcoRI-BamHI* fragments of the *lux* operon from pLVA01 and pLVA02, respectively, and cloned into pPROBE'-GFP-Tagless. An *EcoRI-NotI* digestion of the resulting plasmid and subsequent cloning into  $\lambda$ InCh vector allowed for the genomic integration of the *lux* QS circuit into the *E. coli* MG1655 chromosome. 100 ug/mL ampicillin was added for selection.

The inducible LuxR strain was made by PCR amplification of the *LuxR* gene from MG02S

with forward primer 5' – ATCTCTGAATTCCCGTTTTAATGATATATAACACGCAAACTTGCGAC – 3', which adds an *EcoRI* restriction site upstream of the *LuxR*, and reverse primer 5' – CAAGTATGGTACCCGTA CTTAACTTTTAAAGTATGGGCAATCAATTGCTCC –

3', which adds a *KpnI* restriction site downstream of the gene. The PCR fragment was cloned into pEXT22 plasmid by digesting both with *EcoRI* and *KpnI*, placing *LuxR* under the control of a *tac* promoter. The subsequent plasmid was transformed into MG02S. LuxR overexpression was induced with 10 mM IPTG added to growth medium. 50 ug/mL kanamycin was added for selection

Prior to every experiment, a single colony was selected from a plate and inoculated into LB with the appropriate antibiotics and grown overnight at 30°C with shaking at 230 RPM. The next day, the overnight culture was diluted 1:100 into RM minimal medium [2% casamino acids, 1x M9 salts (12.8g Na<sub>2</sub>HPO<sub>4</sub> 7H<sub>2</sub>O, 3g KH<sub>2</sub>PO<sub>4</sub>, 0.5g NaCl and 1g NH<sub>4</sub>Cl per liter), 1 mM MgCl<sub>2</sub>] with 20 mM Succinate, 20 mM Glucose and 100 ug/mL ampicillin, and grown at 30°C with shaking at 230 RPM until the culture reached an OD<sub>600</sub> of 0.2-0.3 (approximately 3-4 hours). The culture was subsequently centrifuged and cell pellet re-suspended in 1% BSA in PBS prior to loading into the device. Cell loading was performed from the outlet port of a BSA solution-primed device. After loading cells into the device, growth medium with the appropriate antibiotics and 20 mM glucose is supplied to the cells continuously via one or two inlets and the cells are grown at 30°C until all chambers are occupied to capacity before initiating any experiment, unless otherwise indicated. Other growth media used were all variations of the RM minimal medium, with 20 mM, 10 mM, or absence of glucose, or the substitution of 2% casamino acids with 2% tryptone, both of which are sourced from digestions of casein.

#### **2.4.2: Design and fabrication of microfluidic device**



The overall organization of the channels and chambers in the microfluidic device is similar to that in previous studies [58, 59]. Briefly, an array of 16 parallel flow-through channels with a depth of 15  $\mu\text{m}$  is connected to 24 rows of 30 0.8  $\mu\text{m}$  deep chambers each, which house the cells. The dimensions of the chambers are 100 x 100  $\mu\text{m}$ , with a 15 x 15  $\mu\text{m}$  post in the center. The degree to which the chambers are connected to the flow-through channels via coupling channels are varied. 16 rows of chambers are connected to flow-through channels by coupling channels only on one single side of the chamber, while eight rows of chambers are connected to flow-through channels by coupling channels on two, opposing sides of the chamber. Each side of the chamber that is connected to the flow-through channels has either one, two, or three coupling channels, giving one-sided chambers a total of one, two, or three coupling channels, while double-sided chambers have a total of two, four, or six coupling channels. In addition, the coupling channel dimensions are 25 or 50  $\mu\text{m}$  in length, and 10 or 20  $\mu\text{m}$  in width. The combination of different dimensions and configurations of coupling channels produced 24 unique chamber types with varying degrees of mass transport properties. The chambers are organized into four quadrants of six types each, with three single-sided and three double-sided chambers in each quadrant. Each group is then distributed in a tandem, repeated triplet fashion, to ensure that each chamber type is distributed evenly throughout the quadrant to minimize the effect of positional dependence relative to the source of medium.

Growth medium is supplied from either one of two inlets, which connect to the flow-through channels and supply nutrients to chambers on its way to a single outlet port, while the fluid from the alternate inlet is directed to a waste port. Because the height of the

chambers is relatively shallow compared to the height of the flow-through channels, the chambers are much more resistant to flow across the chamber as compared to flow through the channels, hence, the dominant mode of mass transport into the chamber is through diffusion. The symmetric binary branching of the flow-through channels ensures that the pressures are balanced between channels, further preventing crossflow into the chamber. Flow is driven through the device via hydrostatic pressure differences, with the height of the syringe connected to the inlet with the desired medium higher than the alternate inlet, which are both higher than the syringes connected to the outlet and waste port. The medium being supplied to the chambers from one inlet can be instantaneously switched to that of the alternate inlet by swapping the height of the syringes, allowing for rapid changes in the medium conditions.

A chemical gradient-generating microfluidic device was also used in this study, based off of the Christmas tree design [87]. Similar to the device mentioned above, the gradient device contains 2 inlets, 1 outlet, and 1 waste port, allowing for similar operation under normal conditions. However, between the chambers and the inlets are a series of serpentine channels, which can perform mixing of solutions if medium from both inlets are supplied simultaneously. If one inlet (source) contains a molecule which the other inlet (sink) lacks, each stage of serpentine channels performs progressively more refined dilutions, resulting an increasingly resolved concentration gradient spanning the two concentrations of the inlets. Individual concentration doses are separated into channels, allowing downstream chambers to be exposed to different concentrations. The device creates 8 linearly graded concentration doses from 2 input concentrations, each connected to a row of 30 (only

double-sided) or 90 (single- and double-sided) chambers, depending on the design. The design with 30 chambers in each row has only a chamber type with the highest degree of connectivity, while the design with 90 chambers in each row has 12 chamber types, all of which contain 25  $\mu\text{m}$  long coupling channels. The heights of the chamber and channels are the same as the device above, except the design with 90 chambers in each row have chamber heights of  $\sim 0.7 \mu\text{m}$ . The channels converge into the outlet via the same symmetric binary branching structure, allowing for equal pressures. When a gradient is desired, it can be generated by equating the pressure from both syringes and supplying medium from both inlets at the same time. A fluorescent dye is used to visualize the gradient.

The device was fabricated in a similar fashion as in previous studies [58, 59]. Briefly, the initial design was drawn in Adobe Illustrator and sent to be printed as a photomask. The photomask was used to produce a master mold via photolithography. The master mold was made with a 3" silicon wafer with a two-level micro-relief (0.8  $\mu\text{m}$  and 15  $\mu\text{m}$ ) of a UV-curable epoxy (SU-8 by MicroChem, Newton, MA). The first level was made with SU-8 2002 spun onto the silicon wafer at an initial 500 rpm for 10 seconds with an acceleration of 1, then 10000 rpm for 30 seconds with an acceleration of 100, to produce a  $\sim 0.8 \mu\text{m}$  thick film. The chambers were patterned with photolithography, followed by subsequent baking and development to form the structures. The subsequent level was made with SU-8 2015 spun onto the silicon wafer at an initial 500 rpm for 10 seconds with an acceleration of 1, then 3250 rpm for 30 seconds with an acceleration of 2 to produce a  $\sim 15 \mu\text{m}$  thick film. The channels were patterned and made as above. Microfluidic devices were then fabricated with PDMS (Sylgard 184, Dow Corning) via soft lithography. A 5 mm thick

cast of PDMS made with 10:1 ratio of elastomer base to elastomer curing agent. The PDMS cast was peeled off the wafer and cut into individual chips, and ports were punched with a 20-gauge luer stub. Devices were washed and hermetically sealed to #1.5 microscope cover slips, then baked in a 130°C oven overnight prior to use.

### **2.4.3: Microscopy**

Widefield image acquisition was performed on a Nikon Eclipse TE2000 epifluorescence inverted microscope equipped with a motorized stage (Prior Scientific, Cambridge, UK) and a Cascade 1K EMCCD camera (Photometrics, Tucson, Arizona). Time-lapse images were acquired with a Nikon Plan Fluor 40x/0.75 Ph2 DLL objective, while montage images were captured with a Nikon Plan Fluor 10x/0.3 Ph1 DL objective, and stitched together automatically with 10% image overlap with a custom MATLAB script. Both phase contrast and fluorescence images were captured for time-lapse and montage images. Time-lapse images were acquired every 20 minutes, with an exposure time of 100-500 ms, while the montage images were taken with an exposure time of 1000 ms. The excitation filter wavelengths used for GFP detection were 450-490 nm (Chroma, Rockingham, VT), while the emission filter wavelength was 525 nm. The excitation filter wavelengths used for detection of Alexa Fluor 555 were 541-565 nm, while the emission filter wavelengths were 584-679 nm. A spectral 2D template autofocus algorithm was used to maintain the focus for the entire duration of time-lapse imaging. For time-lapsed images, at least two positions for each condition/chamber type were chosen for each experiment, while montages varied from 42 to 77 images depending on the device type used. Control of the microscope and

capture of images were performed in an automated fashion via Slidebook 5.5 (Intelligent Imaging Innovations, Denver, Colorado).

Z-stacks were acquired with a Leica SP8 Laser Scanning Confocal microscope equipped with a white light pulsed laser with continuous wavelength and hybrid detectors. Images were acquired on a HC PL APO 40x/1.30 Oil, CS2 objective and the Leica Application Suite X software.

#### **2.4.4: Image processing and data analysis**

Automated image acquisition was performed with Slidebook 5.5. Raw images were exported in .tiff format and processed using custom MATLAB scripts. All images were corrected for uneven illumination with the following correction:  $C = (I-D)/(F-D)*M$ , where  $C$  is the corrected image,  $I$  is the initial image,  $D$  is the darkfield image,  $F$  is the flatfield image, and  $M$  is the mean of the flatfield minus darkfield images. The flatfield and darkfield were averages of multiple images. Time-lapse images were aligned automatically with a segmentation and alignment algorithm, while montage images were stitched together with the same alignment algorithm with 10% overlap between adjacent images. Each calculated metric is an average of at least 3 independent experiments of at least 2 replicates each for each chamber configuration, unless otherwise indicated.

The automated data analysis pipeline imports the processed image file and determines the square chamber region, excluding the post, containing cells. The mean intensity value for the entire chamber was determined for both sets of image types. For time-lapse images,

this is done for all time points, and additional metrics were also calculated. To visualize the spatial distribution of response along the y-axis, the intensity values were averaged along the x-axis and the resultant column of intensity values were normalized by subtracting the minimum value and dividing by the minimum-subtracted maximum value. The inclination of spatial gradients at each time point was approximated with the slope from a linear regression performed on the column of intensity values versus a normalized distance of 1, with a positive slope assigned to represent higher responses in the distal regions relative to the coupling channels, and a negative slope assigned to represent higher responses in the proximal regions relative to the coupling channels. Double-sided chambers are analyzed as half-chambers along the y-axis due to symmetry, and the calculated metric for both halves are averaged into a single value to represent the whole chamber. Aggregating these intensity value columns for each time point generated the kymographs used for spatial analysis. Onset time is defined as the time point at which more than 1.5% of the pixels within the square region of the chamber have intensity values greater than  $\text{mean} + 4 \cdot \text{SD}$  of the same region in the initial frame. Onset location was quantified from the kymographs. Briefly, the columns of normalized intensity values from the onset time point to a time point 2 hours later were extracted, and the positions with a normalized value of greater than or equal to 0.99 were collected and the mean and standard deviation values were calculated. The initial rate was estimated from the slope of a linear regression on the first 5 hours of response after the onset time within exogenous induction conditions, which is expected to reach maximal levels of production. Time-lapse fluorescence intensity measurements were normalized to the initial value, while chip-wide measurements from montage images were normalized to the chamber type with the highest degree of mass

transfer. Two chamber configurations were excluded (filled shapes) from the montage image analysis of chip-wide measurements due to partial formation of cell bilayer, but z-sections from confocal microscopy confirmed the biphasic nature of the response distribution when monolayers were compared (Fig. 2.5E, F).

Z-stacks from confocal microscopy were split into individual focal planes, with the chamber region for each plane segmented and the mean intensity calculated. The slice with the highest mean intensity was used for analysis, and were compared to the mean value from the maximum intensity projections.

## **2.5: Computational methods**

### **2.5.1: Simulation of diffusion**

Diffusion dynamics were simulated using COMSOL Multiphysics 4.2. Briefly, the 3D geometry of each chamber configuration was recreated within the software, and the concentration of the entire volume of the chamber was set to an initial concentration of 0 mM. All surfaces of the chamber were set to have null flux except for the surfaces that interface with the flow-through channels, which are set to a constant concentration of 0.01 mM, corresponding to the concentration of dye used in the experiment. A diffusion coefficient of  $2 \times 10^{-10} \text{ m}^2 \text{ s}^{-1}$  was used for the Alexa Fluor 555 dye. Time-dependent transport of diluted species simulations were performed for all 24 chamber configurations. The average concentration within the chamber volume was determined and plotted.

### **2.5.2: Simulation of QS response**

The mathematical model is a simplified version of a model from a previous study [83], accounting for only one cell, but with new species and terms added:

$$\frac{d[R]}{dt} = k_6 + \frac{k_3[C]}{K_{DR}+[C]} - k_{10}[R] - k_1[R][A] + k_{-1}[RA] - k_{11}[R] \quad (5)$$

$$\frac{d[RA]}{dt} = k_1[R][A] - k_{-1}[RA] - 2k_2[RA]^2 + 2k_{-2}[C] - k_{11}[RA] \quad (6)$$

$$\frac{d[C]}{dt} = k_2[RA]^2 - k_{-2}[C] - k_{11}[C] \quad (7)$$

$$\frac{d[I]}{dt} = k_7 + \frac{k_4[C]}{K_{DI}+[C]} - k_{11}[I] - k_8[I] \quad (8)$$

$$\frac{d[G]}{dt} = k_7 + \frac{k_4[C]}{K_{DI}+[C]} - k_{11}[G] - k_9[G] \quad (9)$$

$$\frac{d[A]}{dt} = -k_1[R][A] + k_{-1}[RA] - k_{-13}[A] + k_{13}[A_e] + k_5[I] \quad (10)$$

$$\frac{d[A_e]}{dt} = k_{-13}[A] - k_{13}[A_e] - k_{12}[A_e] \quad (11)$$

Diffusion of AI is only considered as a rate of loss from the cell, if no exogenous AI is introduced. In addition, the production of AI from C has been explicitly separated into



production of LuxI from C (which then produces AI) to account for dilution of QS proteins. Because GFP is downstream of LuxI, the added equation is nearly identical, with a different degradation term the only difference. Dilution terms were also added to the equations for all protein species to account for loss of protein due to cell division.

The global constants that are applicable to all the conditions are listed in Table 1, most of which were based on a previous study [84]. For each environmental condition, a new set of  $k_4$  (synthesis, Table 2) and  $k_{11}$  (dilution, Table 3) values were used, the various values of which corresponds to the different chamber configurations, and were measured from experiments.  $k_4$  (synthesis) was estimated with the slope of a linear regression corresponding to the first 5 hours of response after the onset time within exogenous induction conditions, which is expected to reach maximal levels of production. Dilution rates are proportional to growth rate, so  $k_{11}$  (dilution) is calculated in the same way with an exponential fit of the GFP dilution data. The exceptions are  $k_4$  (synthesis) for tryptone and casamino acids conditions at 30°C, which were inferred by comparing the change in growth rates and synthesis rates from tryptone to casamino acids medium at 25°C, and extrapolating that relationship to the change in temperature from 25°C to 30°C in both media types.

Simulations were performed in MATLAB. Briefly, each simulation was run for an initial 24 simulation hours with either the LuxR repressed or LuxR partially repressed values for  $k_3$  and  $k_6$ , to replicate the initial growth in 20 mM or 10 mM glucose medium, respectively, and to allow for a basal steady state amount of proteins and components to be made. The

$k_3$  and  $k_6$  values are subsequently switched to the derepressed or overexpressed values, and simulation resumed for at least another 24 simulation hours. Simulations corresponding to the transient glucose switching experiments consisted of transient changes in the  $k_3$  and  $k_6$  values at the appropriate time points.

**Table 2.1: Simulation parameter values**

Symbol	Value	Units	Description	Reference
$k_1$	$5 \times 10^{-5}$	$m^{-1} s^{-1}$	Association between R and A	(83)
$k_{-1}$	$5 \times 10^{-4}$	$s^{-1}$	Dissociation of RA	(83)
$k_2$	$1 \times 10^{-5}$	$m^{-1} s^{-1}$	Dimerization of RA	(83)
$k_{-2}$	0.01	$s^{-1}$	Dissociation of C	(83)
$k_3$ (LuxR repressed, +20 mM Glc)	$7 \times 10^{-4}$	$m s^{-1}$	Feedback production of R, maximal rate	Estimated
$k_3$ (LuxR partially repressed, +10 mM Glc)	0.00535	$m s^{-1}$	Feedback production of R, maximal rate	Estimated
$k_3$ (LuxR derepressed, -Glc)	0.01	$m s^{-1}$	Feedback production of R, maximal rate	Estimated
$k_3$ (LuxR Overexpressed)	0.1	$m s^{-1}$	Feedback production of R, maximal rate	Estimated
$k_4$	Variable, See Table 2	$m s^{-1}$	Feedback production of I, maximal rate	Measured
$k_5$	0.45	$s^{-1}$	Enzymatic production of A	(83)
$k_6$ (LuxR repressed, +20 mM Glc)	$7 \times 10^{-4}$	$m s^{-1}$	Constitutive production of R	(83)
$k_6$ (LuxR partially repressed, +10 mM Glc)	0.00285	$m s^{-1}$	Constitutive production of R	(83)
$k_6$ (LuxR derepressed, -Glc)	0.005	$m s^{-1}$	Constitutive production of R	(83)
$k_6$ (LuxR Overexpressed)	0.05	$m s^{-1}$	Constitutive production of R	Estimated
$k_7$	$1 \times 10^{-5}$	$m s^{-1}$	Constitutive production of I	Estimated
$k_8$	$5 \times 10^{-5}$	$s^{-1}$	Degradation of I	(83)
$k_9$	$7.4 \times 10^{-6}$	$s^{-1}$	Degradation of GFP	(81)
$k_{10}$	0.001	$s^{-1}$	Degradation of R	(83)
$k_{11}$	Variable, See Table 3	$s^{-1}$	Dilution rate	Measured
$k_{12}$	0.01	$s^{-1}$	Removal of extracellular A	Estimated
$k_{13}$	0.4	$s^{-1}$	Exchange of A from extracellular to intracellular	(83)
$k_{-13}$	0.4	$s^{-1}$	Exchange of A from intracellular to extracellular	(83)
KDI	25	m	Dissociation constant for I	(83)
KDR	1	m	Dissociation constant for R	(83)

**Table 2.2: Dilution rates (Order defined based on Tryptone 25°C condition) ( $s^{-1}$ )**

	Tryptone 25°C	Casamino Acids 25°C	Tryptone 30°C	Casamino Acids 30°C
singlesinglelongnarrow	9.02E-06	3.63E-07	1.05E-05	5.43E-06
doublesinglelongnarrow	1.17E-05	1.91E-06	1.14E-05	6.99E-06
triplesinglelongnarrow	1.24E-05	4.68E-06	1.26E-05	1.11E-05
singledoublelongnarrow	1.37E-05	6.02E-06	1.34E-05	1.29E-05
singlesingleshortnarrow	1.40E-05	7.19E-06	2.18E-05	1.92E-05
singlesinglelongwide	1.50E-05	8.49E-06	2.36E-05	2.18E-05
doubledoublelongnarrow	1.90E-05	1.01E-05	2.1E-05	1.82E-05
doublesingleshortnarrow	2.14E-05	1.38E-05	2.95E-05	2.71E-05
singlesingleshortwide	2.30E-05	1.73E-05	3.46E-05	3.51E-05
doublesinglelongwide	2.57E-05	1.80E-05	3.43E-05	3.54E-05
triplesingleshortnarrow	2.84E-05	1.83E-05	3.48E-05	3.77E-05
tripledoublelongnarrow	2.89E-05	2.05E-05	3.02E-05	2.91E-05
triplesinglelongwide	3.03E-05	2.03E-05	4.05E-05	4.07E-05
singledoublelongwide	3.42E-05	2.36E-05	4.87E-05	4.75E-05
singledoubleshortnarrow	3.50E-05	2.29E-05	5.16E-05	4.33E-05
doublesingleshortwide	3.63E-05	2.59E-05	4.94E-05	5.59E-05
triplesingleshortwide	3.95E-05	2.80E-05	5.65E-05	5.83E-05
doubledoubleshortnarrow	4.57E-05	3.03E-05	6.44E-05	6.08E-05
doubledoublelongwide	4.96E-05	3.31E-05	6.62E-05	6.92E-05
singledoubleshortwide	4.99E-05	3.42E-05	7.32E-05	7.35E-05
tripledoubleshortnarrow	5.31E-05	3.54E-05	7.72E-05	7.13E-05
tripledoublelongwide	5.39E-05	3.65E-05	7.9E-05	7.88E-05
doubledoubleshortwide	5.92E-05	4.04E-05	9.29E-05	8.43E-05
tripledoubleshortwide	6.22E-05	4.36E-05	0.000104	8.56E-05

**Table 2.3: Synthesis rate (Order defined based on Tryptone 25°C condition) (m\*s<sup>-1</sup>)**

	Tryptone 25°C	Casamino Acids 25°C	Tryptone 30°C (Inferred)	Casamino Acids 30°C (Inferred)
singlesinglelongnarrow	0.006953	0.016613	0.014001	0.014001
doublesinglelongnarrow	0.010404	0.0273	0.024679	0.014543
triplesinglelongnarrow	0.015151	0.032305	0.028997	0.015085
singledoublelongnarrow	0.01542	0.031761	0.028238	0.015627
singlesingleshortnarrow	0.015919	0.025956	0.019758	0.016169
singlesinglelongwide	0.016091	0.025045	0.018182	0.016711
doubledoublelongnarrow	0.022878	0.037048	0.032875	0.017253
doublesingleshortnarrow	0.017174	0.02727	0.020442	0.017795
singlesingleshortwide	0.019349	0.028035	0.018884	0.018337
doublesinglelongwide	0.018987	0.029261	0.020302	0.018879
triplesingleshortnarrow	0.018061	0.02931	0.019293	0.019421
tripledoublelongnarrow	0.025332	0.035974	0.031532	0.019963
triplesinglelongwide	0.022206	0.030584	0.020096	0.020505
singledoublelongwide	0.021332	0.03361	0.021291	0.021047
singledoubleshortnarrow	0.019509	0.034323	0.023775	0.021589
doublesingleshortwide	0.021258	0.034675	0.019208	0.022131
triplesingleshortwide	0.024263	0.036005	0.02037	0.022674
doubledoubleshortnarrow	0.026939	0.041492	0.025806	0.023216
doubledoublelongwide	0.032675	0.042832	0.024232	0.023758

singledoubleshortwide	0.031864	0.041858	0.021646	0.0243
tripledoubleshortnarrow	0.038133	0.045328	0.026836	0.024842
tripledoublelongwide	0.039596	0.046597	0.024778	0.025384
doubledoubleshortwide	0.041151	0.048342	0.025689	0.025926
tripledoubleshortwide	0.038491	0.048087	0.026468	0.026468

# **3: Spatial and temporal correlates of quorum sensing**

## **3.1: Introduction**

In the previous chapter, we showed that a dynamical analysis of QS, especially within the context of different environmental conditions, enabled a more comprehensive understanding of how the onset and progression of collective cell behavior actually occurs, which is in stark contrast to the traditional view that they are all switch-like transitions. More specifically, we showed that QS can be highly sensitive to the environment, with variations in the dynamical aspects of onset time, rate of increase, and response intensity level that is characteristic of the different environments. This condition-dependent display of dynamically complex, non-monotonically distributed responses was attributed to a growth-mediated balance of synthesis and dilution of QS machinery proteins. However, since the dynamics were obtained by looking at whole-chamber averages, the analysis does not account for any potential inhomogeneity between individual cells or clusters of cells that can be reflected in the spatial distribution of responses.

Gene expression is known to be inherently heterogeneous, even among genetically homogeneous clonal cells exposed to identical environments [88]. This is due to the fact that biological processes are often governed by small numbers of molecules whose levels are subjected to random fluctuations, resulting in noisy responses. Although QS is theorized to coordinate the synchronous gene expression behavior in cell populations via a diffusible signal, the responses of individual cells within the population can still be

surprisingly diverse. Studies have shown that variability in QS is rampant, and manifest as heterogeneity in the phenotype and at its extreme, could even result in bimodal response distributions [70, 72]. For example, a bimodal QS response distribution was observed within a small range of exogenous AI concentrations (0-50nM) that arose due to a combination of stochastic gene expression and inherent bistability of LuxR expression in *V. fischeri* as a result of positive feedback [73]. While experiments in well-mixed, bulk culture provide a homogeneous environment through which the noisy behavior of the genetic circuit can be precisely characterized, the natural spatial structure of bacterial communities could impart organization to the heterogeneous response that could reveal potential dependences on the localized environmental conditions. Therefore, a spatial analysis of the QS response within the various conditions is crucial to the overall understanding of the dependence on the environmental conditions.

In addition, the sensitivity of the response dynamics, and more specifically, the variable onset time, to the environmental conditions suggests it can act as an important control mechanism of the onset of QS induction. Onset time as a checkpoint control mechanism for QS-associated phenotypic transitions would demonstrate certain properties and features that can help mediate this role. For example, if the onset time functioned as a temporal threshold which requires a persistent stimulation for a duration longer than the threshold time in order for a response to occur, it could prevent transient or spurious inputs from activating a response. This degree of control, if present, is not trivial given that the environment can often fluctuate with complex dynamics. The resistance to response initiation could also be linked to the robustness of the QS response in preventing

deactivation, lending evidence to the communication nature of QS, which is widely accepted but has been difficult to demonstrate. We conclude the chapter by showing that the condition-dependent spatial, temporal and signaling properties culminate in a cell-education strategy that suggests that QS-mediated communication can carry useful information beyond density sensing.

## **3.2 Results**

### **3.2.1: Origins of spatial gradients of QS response**

Differential growth conditions have shown to influence the QS response in terms of the onset and response amplitude. However, this difference was observed across different chamber configurations, where the difference in capillary geometries have a significant effect on nutrient access, as reflected in the wide range of growth rates. Since the chamber dimensions are approximately 50 times larger than the largest dimension of an individual cell, it would be conceivable to imagine that, within chambers, different local nutrient conditions could arise, albeit with a smaller range as compared to across chamber variations. Since the rate of diffusion decays with square of distance, the regions of the chamber distal from the capillary, especially in one-sided chambers, are expected to require more time for nutrients to reach than in regions proximal to the capillary. As verified in the dye diffusion experiments and simulation, as the dye is introduced, regions of the chamber proximal to the capillary consistently have a higher level of signal as compared to regions of the chamber distal to the capillary, prior to the saturation of the dye molecule in the chamber. Unlike the dye, however, diffusive nutrient molecules are actively consumed by cells. Since different regions of the chamber require different amounts of time for a

molecule to diffuse to, if the nutrient is consumed at a rate higher than the diffusion, then the nutrient concentration in regions proximal to the capillary would be higher than compared to the distal regions, forming a nutrient gradient, whereas if the diffusion rate is higher than the consumption rate, the nutrient levels would be expected to be relatively uniform throughout the chamber, in a manner similar to the saturation of the dye molecule. If the access of nutrients within chambers is nonuniform, differences in growth might occur, which we have shown to regulate the QS response via modulation of synthesis and dilution rates that ultimately dictates the accumulation rate of LuxR to a level sensitive to the available AI. We wish to explore whether intra-chamber nutrient gradients exist, and if so, whether the growth-dependent differences in QS response amplitude and onset time, which is a temporal phenomenon, translate to spatial differences in response amplitude and onset position within a chamber.

While regions proximal to the capillary could have slightly different nutrient levels since the chamber under consideration as well as the process of diffusion are three dimensional, we will only consider diffusion and any gradients formed as a result in the single dimension that is orthogonal to the flow-through channels. Since the source of nutrients is the flow-through channels which interfaces with the capillary channel, the diffusive flux would pass through that interface plane in the orthogonal direction. For example, if the capillary is connected to the flow-through channel in the x-z plane, the orthogonal direction is in the y direction. Thus, this orthogonal direction, which is also the direction parallel to the longitudinal length of the capillary channels, would exhibit the greatest diffusive flux, and nutrient gradients formed in this axis would be the steepest, as compared to the other two



axes. While there is no method to measure nutrient levels directly, if we assume the nutrient gradient within a chamber arise from unequal diffusion times coupled with uniform cellular consumption, and we know that diffusion positively correlates with growth rate, then the nutrient gradient should give rise to a proportional growth rate gradient. Since we have shown that there is a dependence of the QS response amplitude on growth rate, the QS response amplitude distribution within the chamber should, by extension, reflect the local nutrient levels.

### **3.2.2: Quantification of spatial gradients**

Indeed, by examining the fluorescence micrographs from experiments in which a QS response has occurred, we can see that different chambers exhibit different distributions of fluorescence response within different regions of the chamber. For example, in the auto-induction experiment in tryptone medium where we observed a biphasic distribution with a relatively large dynamic range of response intensities after 24 hours, the chamber type with three long, narrow capillary channels on one side exhibited higher fluorescence levels in regions proximal to the capillary channel than in regions distal to the capillary, whereas in the chamber type with three short, wide capillaries on one side exhibited higher fluorescence levels in regions distal to the capillary channel than in regions proximal to the capillary (Figure 3.1A). However, differences in spatial response intensity within chambers also appear to depend on medium composition. For example, in the auto-induction experiment in casamino acids medium where we observed a biphasic distribution with a relatively narrow dynamic range of response intensities after 24 hours, the fluorescence intensity in both of the chamber configurations mentioned above appear relatively uniform,

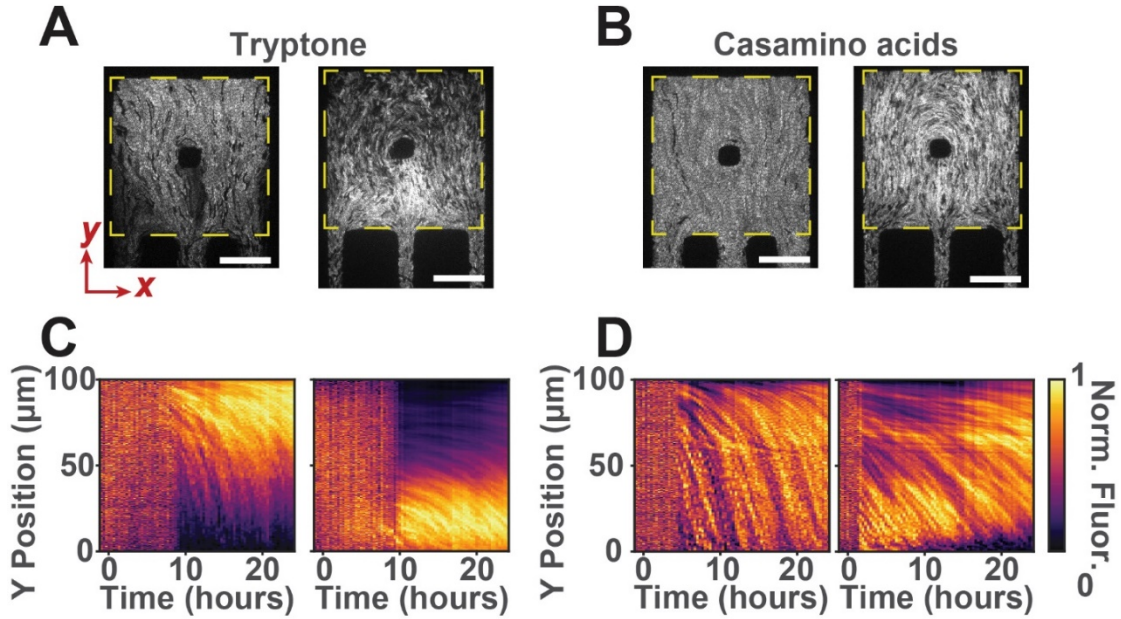


**Figure 3.1: QS expresses spatial gradients of response.** A-D, (A, B) Fluorescence micrographs and (C, D) kymographs of chambers grown in tryptone and casamino acids-based media, respectively, at 25°C. Scale bar, 20  $\mu\text{m}$ .

with no discernable difference between proximal and distal regions of the chambers, relative to the capillaries (Figure 3.1B). To further characterize the fluorescence distribution within chambers, we averaged the 2D fluorescence intensity distribution within a chamber in the direction parallel to the flow-through channels (x) to obtain a 1D fluorescence distribution of the chamber in the direction orthogonal to the diffusive flux plane (y). Combined with normalization of the distribution by mapping the maximum and minimum intensities to 1 and 0, respectively, and aggregating the distribution for each time point of the time-lapse, we can obtain a kymograph that quantifies the response pattern within chambers. Prior to onset, the lack of a signal from cells result in a noisy distribution of normalized intensity with no obvious localization of high intensity. However, once onset of QS response occurs, clusters of high intensity can be observed. For example, in the case of the chamber type with three short, wide capillaries on one side grown in tryptone medium, the kymograph indicated a sustained high level of response in the region

approximately 75  $\mu\text{m}$  (out of 100  $\mu\text{m}$ ) away from the capillary, which in this instance is at 0  $\mu\text{m}$  (Figure 3.1C). The normalized response intensity decreases as the distance from the capillary is decreased, which is in agreement with the fluorescence micrograph. This

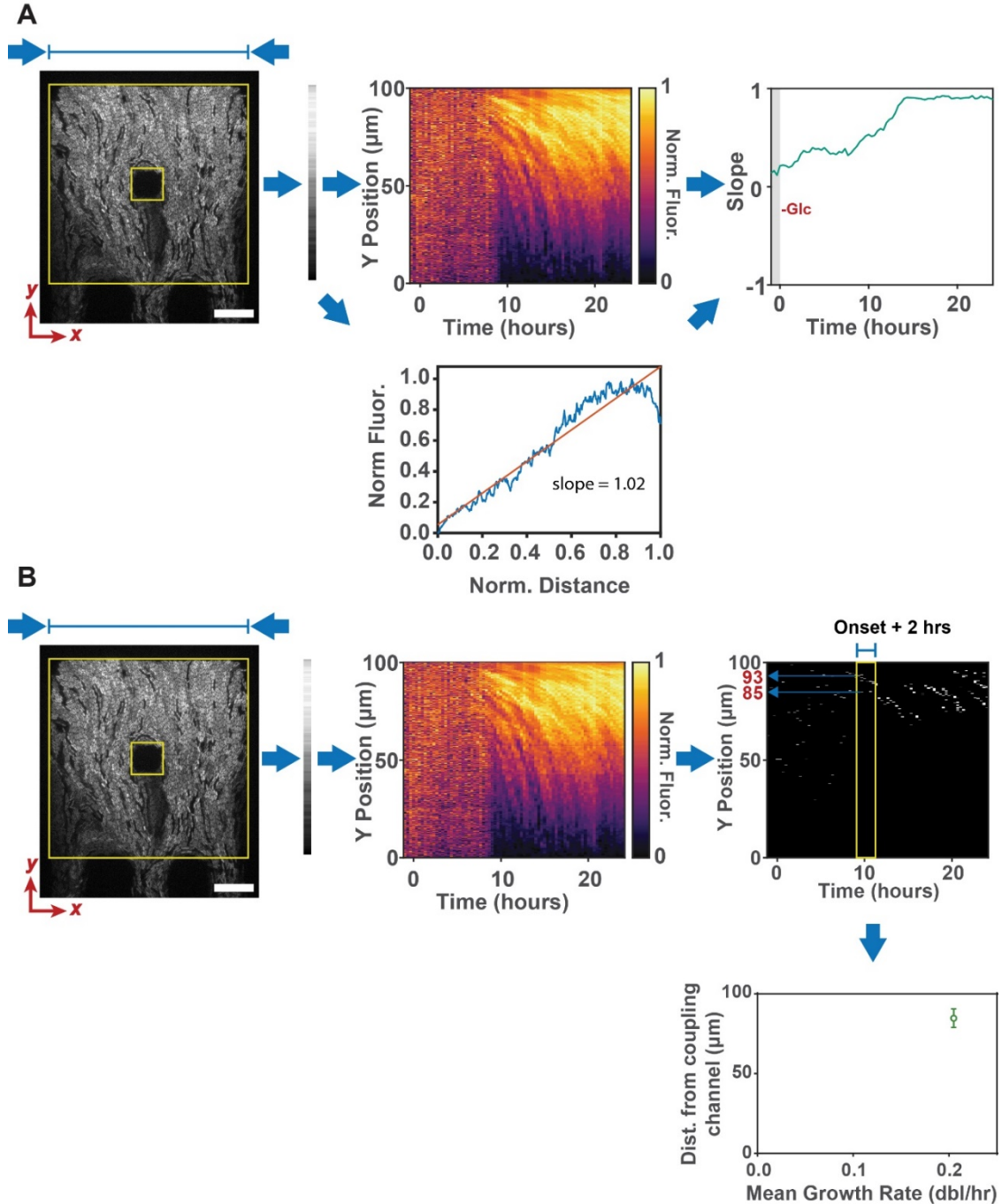


**Figure 3.2: Quantification workflow for spatial gradient and onset location. A,** Diagram indicating the workflow of the quantification of spatial response gradient within chambers. Scale bar, 20  $\mu\text{m}$ . **B,** Diagram indicating the workflow of the quantification of spatial onset localization within chambers. Scale bar, 20  $\mu\text{m}$ .

demonstrates that response gradient can occur within chambers. Conversely, in colonies grown in casamino acids medium and in the same chamber type, the kymograph indicated high and low levels of response spread relatively uniformly throughout the chamber, demonstrating the lack of an obvious response gradient within these conditions (Figure 3.1D). To quantify the gradient of response within chambers for all chambers, the slope from the linear regression of the normalized intensity distribution from each time point of the kymograph was determined. A positive slope indicates higher intensity in regions of the chamber distal to the capillary, while a negative slope indicates higher intensity in regions of the chamber proximal to the capillary (Figure 3.2A).

### **3.2.3: Spatial responses are nutrient-dependent**

In auto-induction within tryptone medium, the majority of the chambers have slopes greater than 0.5 or less than -0.5 after 24 hours, indicating the presence of a significant response gradient within the chambers (Figure 3.3A). The chambers with lowest growth rates have negative slopes from time of onset to the end of 24 hours, indicating preference for higher response levels proximal to the capillary, whereas chambers with intermediate and higher growth rates have positive slopes from time of onset to the end of 24 hours, indicating a preference for higher response levels distal from the capillary. The moment of onset caused a rapid emergence of the response gradient, which sharply increased the polarization within the chamber. While the gradient within the majority of chambers exhibited the same sign for the slope throughout the 24-hour period, a few chambers exhibited a switch in the slope, starting with negative slope initially, but converted to a positive slope as the response progressed. In exogenous induction within tryptone medium, the slopes for the different

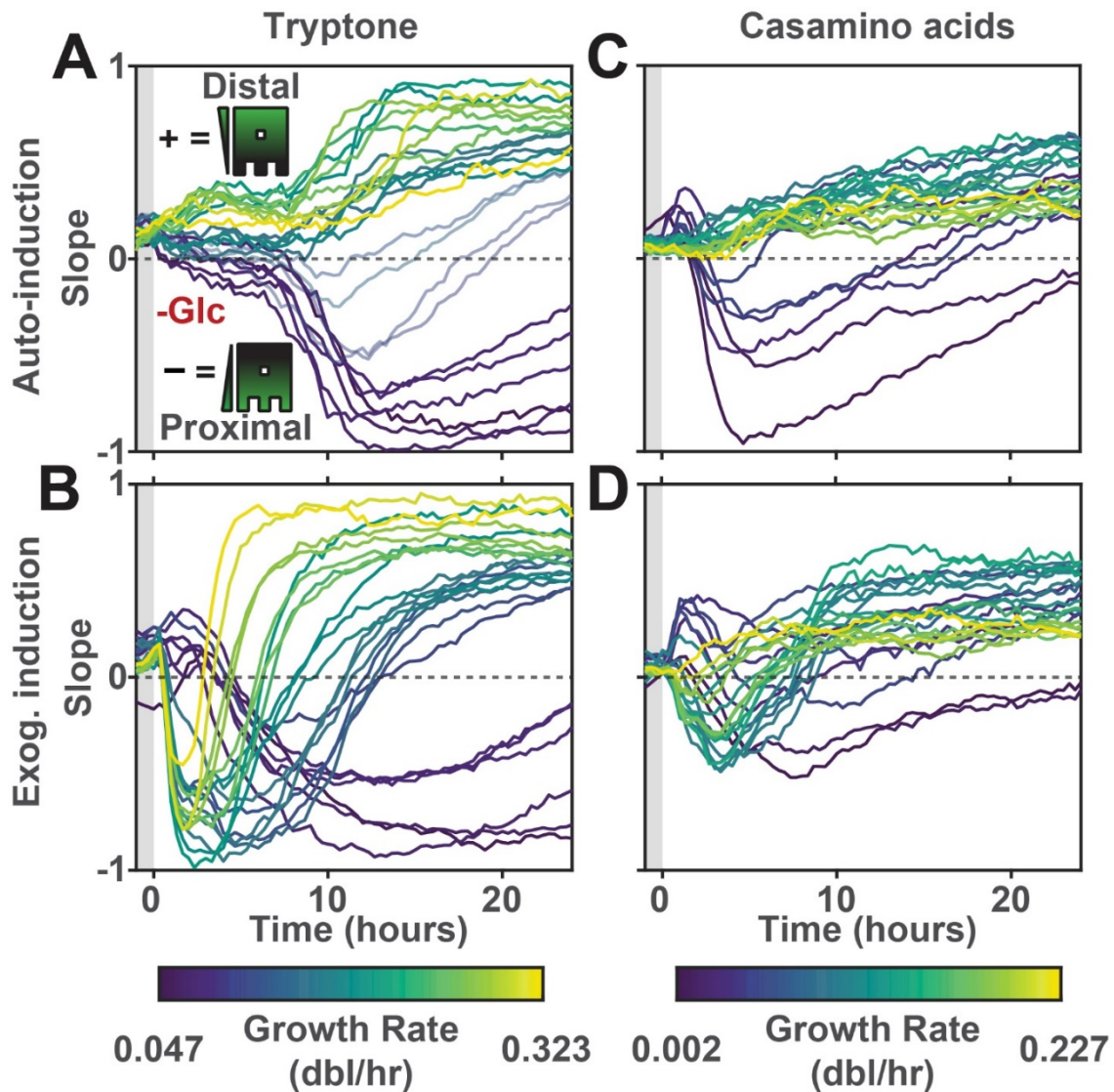


**Figure 3.3: Spatial responses exhibit condition-dependent dynamics. A-D,** Quantification of spatial distribution of response with linear regression in auto- and exogenous induction in (A, B) tryptone and (C, D) casamino acids medium at 25°C. Positive slope indicates higher response in the regions distal from the coupling channels, whereas negative slope indicates higher response in the regions proximal from the coupling channels. (n = 6, from 3 independent experiments).

chamber configurations at the end of the 24-hour period is similar to the auto induction with the majority of the chambers having slopes greater than 0.5 or less than -0.5 after 24 hours, but, like the comparison of their response level dynamics, the dynamics of the slopes are also completely different (Figure 3.3B). Since the introduction of the exogenous AI is

from the capillary, the cells residing within the chamber proximal to the capillary would be exposed to the AI first, causing all of the chamber configurations to start with a negative slope. Although the diffusion of AI into the chamber would take only a matter of minutes, the onset of the response still spread in a hierarchical fashion inward from the proximal regions of the chamber into the distal regions. This could be due to the fact that induction causes the upregulation and expression of QS-related genes, which might increase the consumption of nutrients, exacerbating the nutrient gradient. This allows cells in the proximal regions to have higher initial response levels, as they also have higher access to nutrients for making QS proteins. However, as the cells in the interior and distal regions became induced, they were able to achieve higher levels of induction than the proximal regions, thereby swinging the slope back into the positive regime. This could potentially be due to the shift in balance of the synthesis and dilution as a result of the nutrient gradient. The dynamics of spatial response will be further examined in a later section.

In contrast, in auto-induction within casamino acids medium, the majority of the chambers have slopes less than 0.5 or greater than -0.5 after 24 hours, indicating the lack of an obvious response gradient within the chambers (Figure 3.3C). The lack of an obvious gradient and relatively small slopes indicate the relative uniformity in the response level throughout the chamber, which is observed within the fluorescence micrographs as well. The overall dynamics are very similar to the tryptone cases, except much more subdued. An equivalent analysis can be applied to the exogenous induction case, in which slope values at the end of the 24-hour period were very similar to the auto induction case, and the dynamics was also a much more subdued as compared to the tryptone exogenous

induction situation (Figure 3.3D). The differences in slopes between tryptone and casamino acids medium is likely caused by the same phenomenon that caused the differences in the dynamic range in the distribution of response levels in different chambers between the two medium conditions. Casamino acids was observed to homogenize the response levels between the different chamber configurations, which was attributed to either increased LuxI synthesis rates or increased QS component retention rates as a result of reduced growth and dilution, or a reduction in the consumption rate of nutrients, thereby allowing diffusion to create a more uniform nutrient profile between the chamber configurations and minimizing the effects of differential diffusion. The same reasoning likely applies to the homogenization of the response within the chamber.

#### **3.2.4: Spatial gradients map onto mean response distribution**

Since we demonstrated that the spatial distribution of QS within chambers likely correspond to spatial gradients of nutrients, in a manner identical to how differences in diffusive nutrient access defined the biphasic nature of the mean response distribution, we reasoned that the spatial gradients of response within a colony would therefore correspond to a segment of the biphasic dependence curve around the points associated with the mean growth rate for a given chamber (Figure 3.4A). This would in turn resolve the ambiguity discussed at the conclusion of chapter 2 [i.e., two distinct coupling coefficient (growth rate) values with the same average response], by associating gradients of opposite signs to the rising and falling parts of the biphasic curve. Indeed, we observed that the distribution of slope signs corresponding to spatial response gradients are consistent with their location on either half of the biphasic curve, which have different response inclinations. Chambers

with slower growth rates lie on the side of the curve where mean response level is a

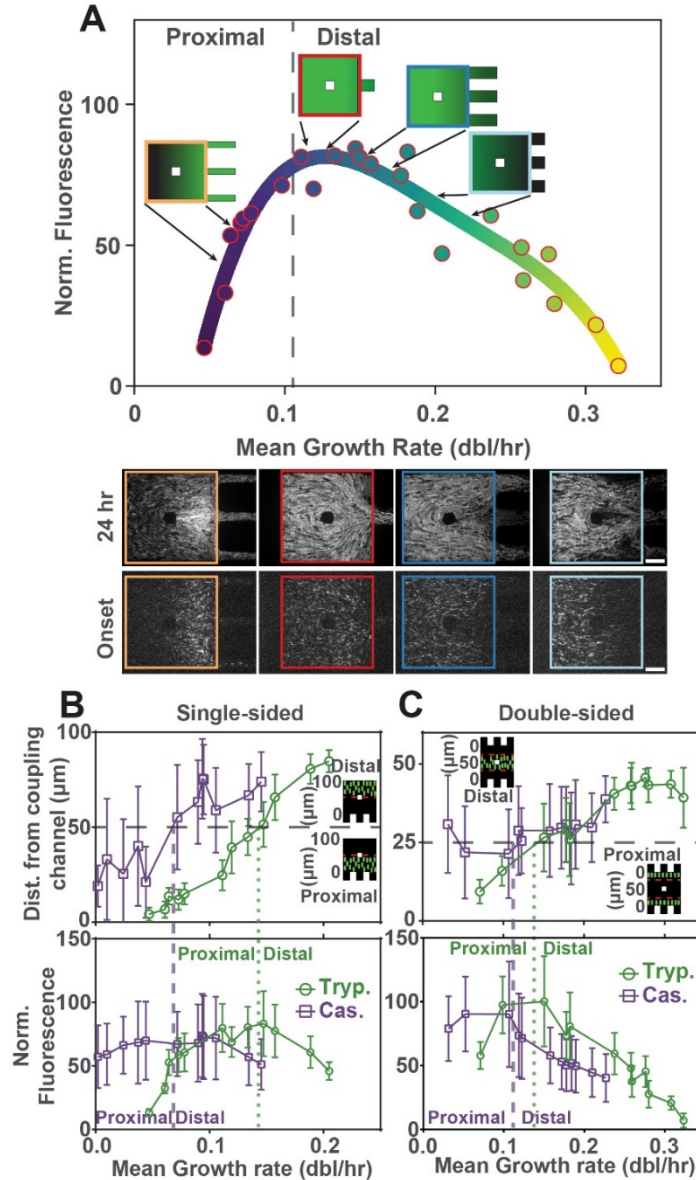


**Figure 3.4: Non-monotonic QS dependence on local growth rate specifies divergent spatial QS gradients and onset locations.** **A**, A smoothed reproduction of the biphasic response distribution from auto-induction in tryptone medium at 25°C color-coded according to growth rate, with diagrams of various chamber configurations with QS response gradients depicted to illustrate the correlation. Fluorescence micrographs of chamber configurations corresponding to those illustrated at 24<sup>th</sup> hour and at onset are below. Scale bars, 20  $\mu\text{m}$ . **B**, **C**, Spatial localization of auto-induced QS response onset in **(B)** single- and **(C)** double-sided chambers in tryptone and casamino acid media at 25°C, in relation to response magnitude distributions after 24 hours in the same conditions ( $n = 43-64$ , from 3 independent experiments for onset location,  $n = 6$  from 3 independent experiments for response magnitude) (mean  $\pm$  SD).



monotonically increasing function of growth rate, meaning that as growth rate increase, the response increases. This matches the spatial gradients of the chambers with these growth rates, which all have negative spatial slope signs corresponding to higher levels of response in the regions proximal to the coupling channels (closer to nutrients, higher growth rate). Similarly, chambers with higher growth rates lie on the side of the curve with a monotonically decreasing mean response level with respect to growth rate, signifying that segments on this portion of the curve have higher response level at lower growth rates. Indeed, the spatial gradients of the chambers with these growth rates, which all have positive spatial slope signs that indicate higher levels of response in regions distal from the coupling channels (away from nutrients, lower growth rate). The coherence between the biphasic mean response distribution and the spatial response gradients further supports the mechanism.

Furthermore, since the spatial response distributions can be explained by the biphasic mean response distribution, we wished to explore whether the dynamics of the mean QS responses can account for the temporal dynamics of the QS response gradients. We can apply the same analysis as we did previously for the last time point by examining the response distributions at discrete time points throughout the time course and compare it with the spatial response distributions at the identical time point. We found that at the onset of QS for auto-induction, the initial response amplitude distribution is already biphasic, with intermediate growth rate chambers achieving the maximum rate (Figure 2.6A). This, in turn, suggested that the location of QS onset in chambers with lower average growth rates would be proximal to the nutrient-supplying channels, while chambers with higher

average growth rate have onset in distal locations. This prediction was indeed supported by the experimental observations, with a monotonic shift of the location of the QS response from more proximal to more distal areas with increasing growth rate (Figure 3.3B, 3.4B, C). On the other hand, the initial rates of QS response were maximal for the chambers with the highest growth rates in exogenous induction, resulting in an initial monotonically increasing response amplitude distribution (Figure 2.6B). This suggests that the onset is localized proximal to the nutrient-supplying channels for all average growth rates, as was indeed observed (Figure 3.3B). Over the course of 24 hours, the response amplitude distribution for auto-induction changes minimally, implying that in most chambers, the spatial gradients would not change signs over the course of the experiment. On the other hand, the response amplitude distribution for the exogenous induction case change from monotonically increasing to biphasic, implying that the gradient signs would change over time. For instance, for chambers with higher growth rates, the initial negative sign would be predicted to switch to positive, resulting in an apparent wave of maximum QS response transitioning from proximal to distal areas of the chambers. These predictions were indeed also supported by experimental observations. While the spatial response were more homogenous in casamino acid medium, which is also reflected in the less pronounced biphasic QS response distribution, it remains consistent with the proposed mechanism (Figure 2.10, 3.3C, D, 3.4B, C). Overall, these results suggested that both the mean values and the spatial gradients of the QS response in individual chambers can be accounted for by the same mechanism, postulating that these responses are defined by the local and environmental conditions, primarily nutrient availability, defining the growth rate values both within different parts of the chamber and for the chamber as a whole.

### **3.2.5: QS exhibits temporal threshold property**

Thus far, QS onset has been demonstrated to exhibit tight spatial and temporal control, with the location and timing of the onset of QS being highly sensitive to the environmental conditions. Specifically, the latter displayed a large range of waiting times before the initiation of signaling. Since QS response onset represents a decision by the cell, based on the information sensed about the environment, to commit to a change in its gene expression profile that results in massive reallocation of resources and behavioral changes in individual cells, onset is naturally tightly regulated. Altering the growth conditions or QS component levels directly has been shown to alter the dynamics of QS, and in particular, the onset time, which experiments and simulations have suggested was due to modulations in the balance of synthesis and dilution rates. Variation of the synthesis and dilution rates effectively altered the QS component accumulation rate, which, if onset is triggered by attaining a LuxR level that is sensitive to the local AI concentration, suggests that the variation in onset time observed previously is reflective of the amount of time required for the buildup of QS components. If, indeed, accumulation of QS components as regulated by synthesis and dilution rates is dependent on the length of time, then variation of the duration of waiting period would affect the amount of accumulation, and therefore, the propensity of onset. Since cells were grown in media with 20 mM glucose, which suppresses LuxR production prior to the start of the experiment, and onset only occurs upon glucose removal, the candidate QS component that is accumulated during the duration of time prior to onset is most likely LuxR. Therefore, by transiently varying the derepression of LuxR production with the duration of glucose removal, we can modulate the time for LuxR accumulation

and ascertain the dependence of onset on the accumulation of basal level production of LuxR. This observation raises the possibility that there is a condition-dependent temporal threshold in QS, requiring a persistent change in the environment longer than the threshold for the response to occur.

A short, transient switch from 20 mM glucose to 0 mM glucose for 4 hours in tryptone medium at 25°C, which is shorter than the fastest onset timing of ~7 hours in these conditions, effectively did not result in the onset of a QS response, producing a pattern of response similar to that from the sustained glucose exposure for 24 hours (Figure 3.5A). This is corroborated by simulation results, which did not display the onset of a QS response in any chamber type after a 4-hour transient switch to higher LuxR constitutive and feedback production rates corresponding to basal, unrepressed expression levels (Figure 3.5A). This demonstrates that the onset of a QS response is dependent on the accumulation of QS components to a high enough level, which manifests as a temporal threshold that can filter stimulating inputs below a certain threshold duration. While the QS response did not occur, the transient input might have primed the cells for a subsequent stimulation via integration of QS component from the previous round of stimulation. This was investigated by periodic changes of the environmental conditions using cycles of removal and addition of glucose (4 hour-long pulses, 50% duty cycle). We again observed no QS onset, even though the total integrated stimulation time (12 hours) exceeded the mean onset time in these conditions (~11 hours) (Figure 3.5B). From the results of the auto induction experiments performed by removing glucose for 24 hours, which resulted in the QS response induction within all chamber configurations, it is known that an increase in the

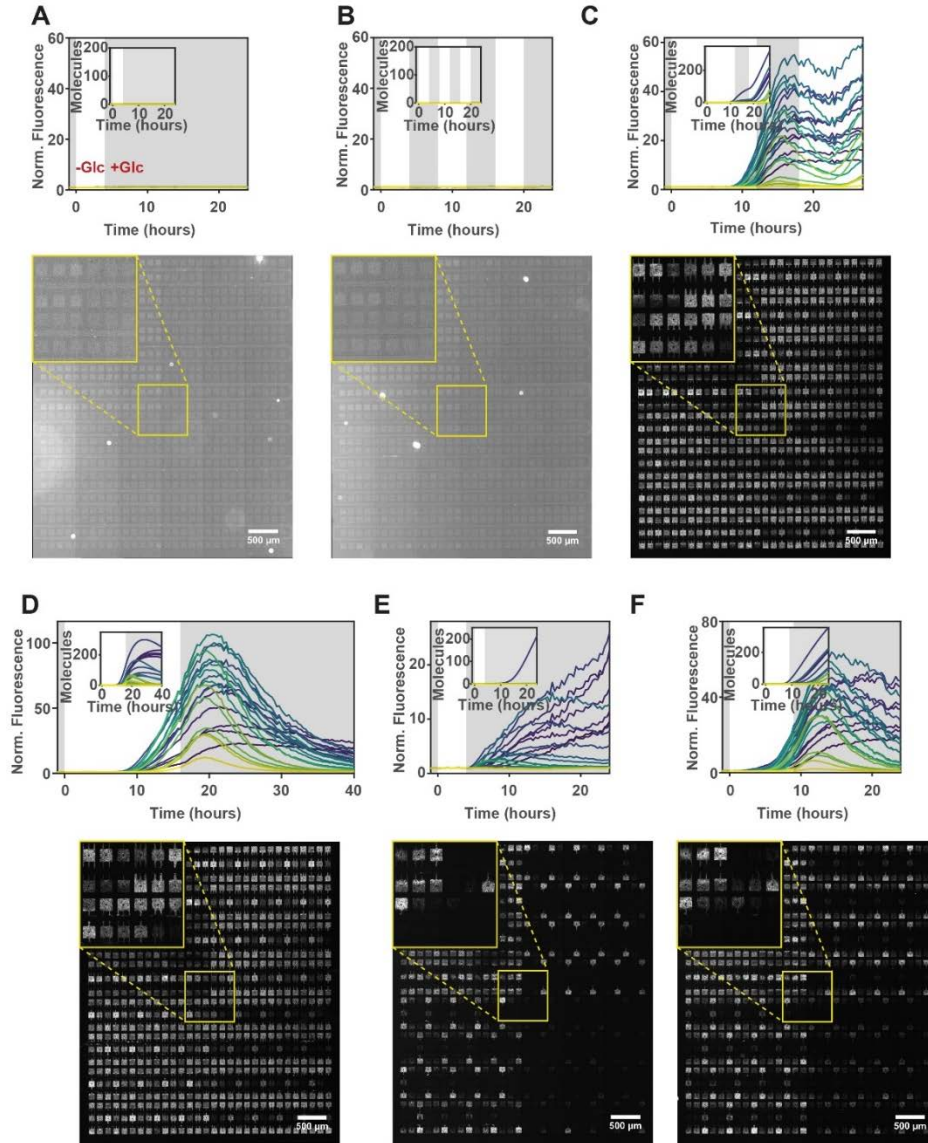


**Figure 3.5: QS displays temporal thresholding and hysteretic properties.** A-F Response dynamics and fluorescence micrographs of (A) 4 hour transient glucose (20 mM) removal, (B) 4 hour, 50% duty cycle pulses of glucose (20 mM) removal, (C) 12 hour glucose (20 mM) removal, followed by 6 hour glucose (20 mM) reintroduction, and subsequent 9 hour glucose (20 mM) removal, (D) 16 hour transient glucose (20 mM) removal, (E) 4 hour transient glucose (10 mM) removal, and (F) 9 hour transient glucose (10 mM) removal ( $n = 6$ , from 3 independent experiments). All conditions were in tryptone medium at 25°C. Insets in graph contains simulated dynamics. Insets in micrographs contain magnified view of the region indicated, which contains all 24 chamber configurations.

duration of derepression would allow for the threshold to be surpassed. Therefore, continuous stimulation for the threshold duration is required for QS onset to occur, and

extending the duration of stimulation time results in induction. However, a reduction in the duration of stimulation per cycle, even with 50% duty cycle, results in the suppression of the response, allowing the system to behave not only as a threshold, but potentially also as a low pass filter. If the onset is indeed the result of accumulation of LuxR, this suggests that the dilution of LuxR occurs relatively fast, perhaps on a similar timescale as synthesis, so that a 50% duty cycle would lead to no effective accumulation of LuxR that can activate the onset, since whatever is produced during the stimulatory period is diluted when glucose is reintroduced.

### **3.2.6: QS response exhibits bistability and hysteresis**

Since we have established that there is a temporal threshold that can restrict the ability to respond unless a threshold duration of stimulation is applied, we next wanted to explore how the temporal threshold compares to the observable timing of QS onset. The mean and S.D. onset time for this condition across different coupling conditions is  $11.0 \pm 2.7$  hours for autoinduction, so a stimulation duration of 12 hours would induce QS in only a subset of chambers if the threshold time is similar to the onset time. Surprisingly, transient glucose removal for 12 hours resulted in induction in all chamber configurations except one, with multiple initiating induction post-stimulation, demonstrating that the threshold is shorter than the observed onset time (Figure 3.5C). The increase in duration of LuxR derepression allowed for a longer period of LuxR production and accumulation, thereby presumably leading to higher levels of LuxR in the cell, which increases the sensitivity to endogenously produced AI and allow for the onset of a QS response to occur. In addition, we found that after the reintroduction of inhibitory concentrations of glucose, the response continued to

increase briefly before decreasing. Likewise, a subsequent reversal in the environment was again followed by delayed changes in signaling output. This stabilizing effect was best exemplified by chambers with the lowest diffusive coupling, which appeared impervious to the perturbations and remained persistently induced throughout. Since transient responses can be stabilized by positive feedback and the associated hysteresis, we tested how QS-associated positive feedback might maintain a response within sustained inhibitory conditions.

By increasing the duration of the transient derepression of LuxR expression from 12 hours to 16 hours for the 20 mM glucose condition, all chambers became induced, and those that were already induced reached an overall higher level of induction, thus, presumably creating an environment with higher levels of endogenous AI (Figure 3.5D). Upon reintroduction of glucose for 24 hours, most chambers lost their response, but persistent induction was still observed in the same group of chamber types, suggesting that the QS onset in poor coupling conditions can become irreversible. The increase in the duration of transient derepression did not appear to be effective in shifting the number of chamber configurations from low stable states to a high stable state. While the longer derepression period allowed for all of the chamber configurations to reach a higher level of induction, the same distribution of chamber configurations still exhibited a decay in the response a few hours after glucose was reintroduced, suggesting that the endogenously produced AI cannot attain high enough levels to sustain a high level of QS response in the presence of high levels of glucose suppression of LuxR production. An analysis of the response dynamics and the accompanying hysteretic diagram provided clues as to the basis of the

sustained induction within previously inhibitory conditions. For the chambers that initiated their response in stimulatory conditions and then subsequently declined in their response once glucose was reintroduced, it suggests that at the 20 mM glucose concentration, there is only one stable low state of response (Figure 3.6A, B). The stimulatory period initiated the response, which tried to reach the high stable state of expression at 0 mM. However, when conditions reverted back to inhibitory, the stable state of response is again at a low level, resulting in the loss of response. However, for the stably induced chamber, there exists two stable states at the 20 mM glucose condition (Figure 3.6C). Since the cells were previously uninduced, the system starts at the low stable state. However, once glucose is removed and the cells become stimulated, the response increases. Due to hysteresis, however, when conditions were reverted back to inhibitory after the cells had already been stimulated, the system approached the second high stable state instead. Therefore, the number of chamber configurations that can reach a high steady state of response is dictated by its stability regimes on the hysteretic plots, which is determined predominantly by the glucose concentration experienced by the colony. Overall, these results revealed a strong bi-stable nature of the response consistent with the postulated feedback interactions within the lux signaling circuit, leading to a ‘permanent memory’ of a prior induction even if the environmental conditions no longer favor QS.

### **3.2.7: Bistability and hysteresis are dependent on LuxR**

Since persistent signaling is determined by the bistability regime defined by the glucose concentration, the propensity for persistent signaling after a transient QS induction may increase if the glucose concentration was decreased. By reducing the concentration of



glucose, the reduction in the suppression of LuxR would make the cells more sensitive to the endogenously produced AI, potentially resulting in more chambers transitioning to a

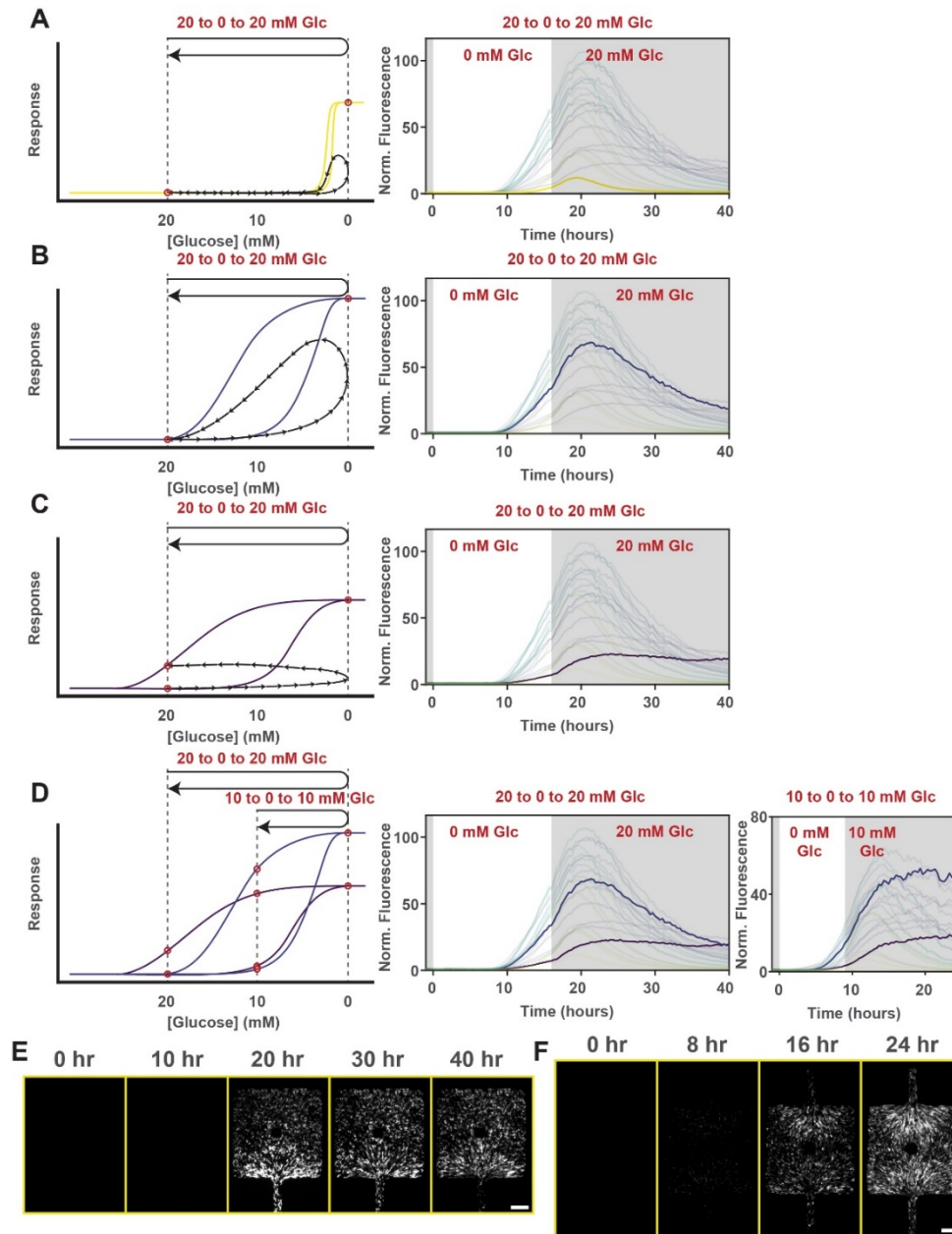


**Figure 3.6: Hysteretic response in transient environments.** A-D, Plots of response dynamics with accompanying diagrams illustrating the hysteretic response, within 16 hour transient glucose (20 mM) removal (A-D) and 9 hour transient glucose (10 mM) removal (D). All conditions were in tryptone medium at 25°C. E, Filmstrip of chamber that maintained a stable high state of expression within 4 hour transient glucose (10 mM) removal. Scale bar, 20  $\mu$ m. F, Filmstrip of chamber that maintained a stable high state of expression within 9 hour transient glucose (10 mM) removal. Scale bar, 20  $\mu$ m.

high stable steady state level of expression. Indeed, for cells pre-incubated in 10 mM glucose (QS onset time of  $7.5 \pm 1.5$  hours), glucose removal over 4 hours was enough to elicit a transient QS onset in many chamber configurations (Figure 3.5E). Upon the reintroduction of 10 mM glucose into the medium after 4 hours of absence of glucose, the QS response in many chambers reached a plateau and subsequently decayed in a similar fashion to the reintroduction of 20 mM glucose, but 7 of the chambers that responded continued to increase in the level of response. It is important to note again that growing the cells in 10 mM glucose as opposed to 20 mM resulted in a faster onset, consistent with previous results. Also, induction for the chambers that did become induced occurred after the reintroduction of glucose, again consistent with the temporal threshold being shorter than the observed onset time. Furthermore, a couple of the chambers did not become induced with this short stimulation time, demonstrating the temporal threshold's ability to filter out stimulates that are shorter than the threshold duration and prevent response onset. Increasing the duration of the transient derepression of LuxR expression from 4 hours to 9 hours in 10 mM glucose condition permitted all chambers to become transiently induced and achieve higher amplitudes of induction, but did not affect the number of chambers displaying irreversible QS (Figure 3.5F). This result was in contrast to only 3 chamber configurations displaying a persistent QS response after restoration of glucose levels to 20 mM, suggesting that the memory of induction, bistability, and hysteresis displayed by bacterial colonies can depend not only on the stressful condition itself, but also on the current state of the environment. Analysis of the hysteretic diagram indicated that lowering the glucose concentration can indeed shift certain chambers into a bistable regime, allowing it to reach a high stable state of expression at 10 mM glucose, while attaining only a low

stable state of expression at 20 mM glucose (Figure 3.6D). The 7 chambers are the types that have the lowest growth rate, meaning also the most restrictive in terms of diffusion, whether it is access to nutrients or loss of endogenously produced AI. However, the ability to remain in a stable high state is most likely not due to differential retention of endogenously produced AI, since chambers in the 20mM condition would have similar diffusion properties, and yet, only the chamber with the slowest growth rate was able to maintain a steady level of response. The ability for some chamber configurations to remain at a stable high state in 10 mM glucose is most likely attributed to the differential access to nutrients, and more specifically, glucose, which altered the degree of repression between the chamber configurations. The modulation of 20 mM glucose by differential diffusion between chamber configurations was most likely not enough, since only the chamber with the lowest growth rate was able to maintain a stable level of response.

### **3.2.8: Emergence of an induced subpopulation**

Visual inspection of chambers with persistent QS response revealed that only a fraction of the cells was induced, which were sparsely distributed (Figure 3.6E, F). The higher-than-basal levels of AI produced by the induced subpopulation could be key to the maintenance of the high stable state of expression in the presence of active suppression. Indeed, simultaneous induction and repression with exogenous AI and glucose, respectively, stably maintained an induced subpopulation (Figure 3.7A, B). This implies that the inherent bistability of the circuit can result in bimodal distributions of cell responses within a clonal population if enough AI is present to react with available LuxR. Therefore, if AI was endogenously produced by cells, instead of supplied exogenously, a population of auto-

induced cells might produce enough endogenous AI to sustain the response in conditions where LuxR production is partially repressed. Furthermore, we hypothesized that this subset of cells could represent a memory of prior stimulation, which can provide a selective

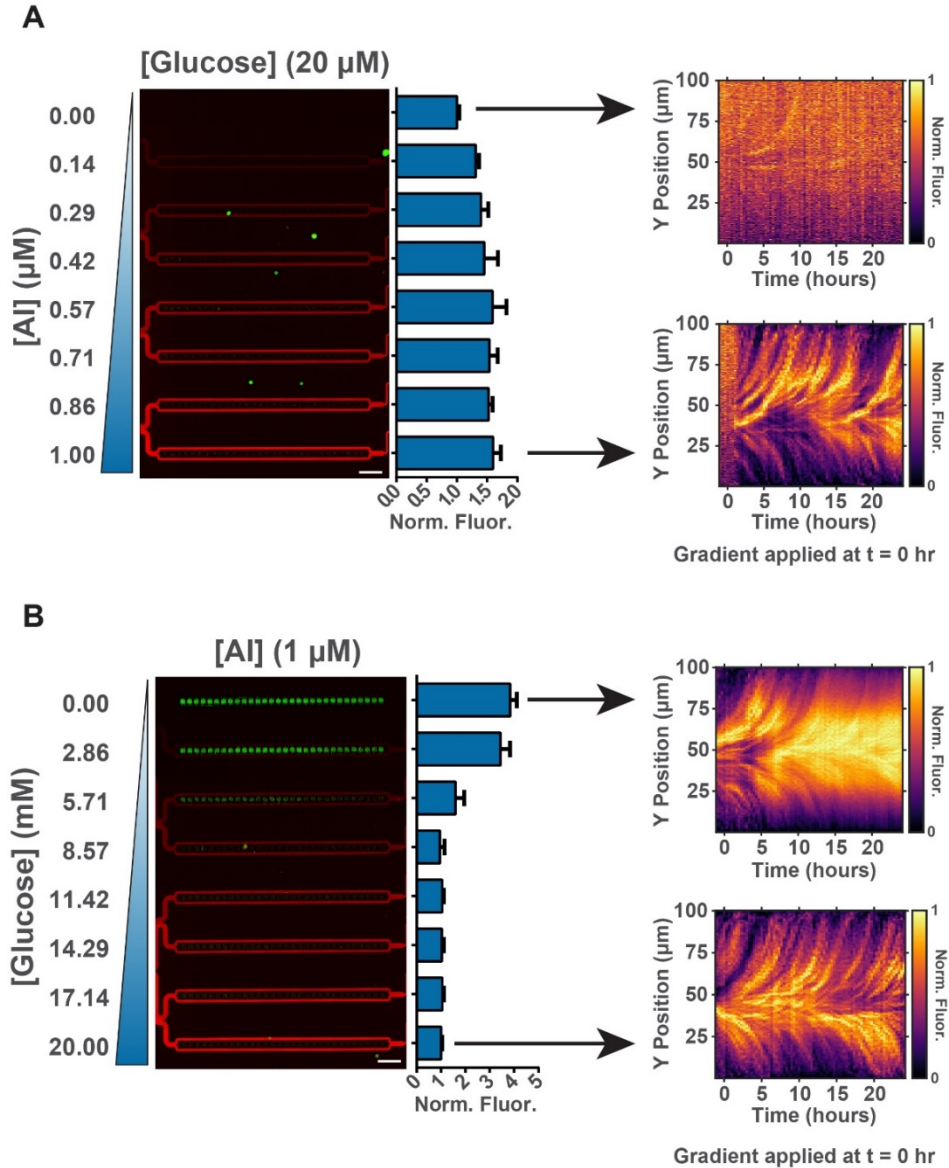


**Figure 3.7: Simultaneous induction and repression elicits induced subpopulation.**

**A**, Fluorescence micrograph and response distribution of exogenous induction with a 0-1  $\mu\text{M}$  AI gradient in the presence 20 mM glucose in tryptone medium at 25°C ( $n=30$ ). Kymographs of the two extreme conditions are shown, with the gradient applied at time  $t=0$  hr. **B**, Fluorescence micrograph and response distribution of exogenous induction with a 1  $\mu\text{M}$  AI in the presence 0-20 mM glucose gradient in tryptone medium at 25°C ( $n=30$ ). Kymographs of the two extreme conditions are shown, with the gradient applied at time  $t=0$  hr. Scale bar, 500  $\mu\text{m}$ . (mean  $\pm$  SD)

advantage if conditions become stimulatory again. Although this strategy is superficially similar to the commonly assumed “hedging of bets” scenario, relating the diversification of response to a selective advantage under uncertain environmental conditions, the cell-cell communication nature of QS imparts additional benefits. The induced cells can potentially promote and accelerate the induction of neighboring cells with their released AI following a change in conditions. We thus explored if the signaling aspect of QS can indeed reduce the temporal threshold and accelerate the onset of response.

### **3.2.9: Induced subpopulation as a memory**

The spatial dependence of QS onset location represents the existence of a subpopulation of cells that are more sensitive to environmental perturbations and can respond earlier than other cells. Such a subpopulation of extra sensitive cells has been encountered previously, as in the case of growth within tryptone medium at 30°C, where individual cells would exhibit a burst of response that was not sustained before diluting out, as well as in the case of exogenous induction in the presence of 20mM glucose, where certain cells were stably induced, while others were suppressed. While these examples support the existence of an extra sensitive subpopulation, the first instance which suggests that such a subpopulation can arise naturally and be effective in its ability to affect the QS response in a significant way is the spatial dependence of QS response onset. The existence of such a subpopulation which can respond earlier implies the possibility of a hierarchical induction of the QS response within a population, in which the most sensitive subpopulation activates slightly less sensitive cells via the signals they produce, which then activate progressively less sensitive cells in a sequential, iterative manner. We have seen evidence of a hierarchical

pattern of induction in the auto-induction of the QS response within tryptone medium at 25°C, which occurs over a long period of time, such that even after 24 hours, the response is still heterogeneous, with numerous cells yet to exhibit a QS response. The heterogeneity in cell induction can be remedied with the addition of exogenous AI, growth within casamino acids medium, or overexpression of LuxR, which can cause the percentage of induced cells to be at or near 100%, indicating that while all cells have the innate ability to respond, it is the conditions dictate the likelihood of a response. If the induction does occur in a hierarchical fashion, then it implies that the AI produced by the extra sensitive initial responders can influence the response of the other cells, which can have multiple advantages.

If environmental conditions change such that a subpopulation of responding cell develops, but then reverts back to a condition un conducive to a QS response, the subpopulation can provide a small amount of AI that helps prolong the overall length of response within the colony before committing to switching off the response entirely or maintaining the induction, thus making it more robust to perturbations. For example, in the experiment with 4-hour transient removal of 10mM glucose, where the conditions were reverted back prior to or at the onset of induction, a select number of chambers were able to maintain a level of response even as the conditions were un conducive to a QS response. In a sense, the formation of a subpopulation of responding cells endows the colony with a memory of the change in the environment, which in the previous case, aided in the robustness of the response when the conditions became un conducive to the QS response. We wonder, however, whether this memory, in the form of a responding subpopulation, could also be

beneficial if the conditions were to then become conducive to QS once more, or become even more conducive to QS than previously. Specifically, could the presence of a responding subpopulation, which produces higher-than-basal amounts of AI, create conditions more conducive to the onset of uninduced cells than within basal levels of AI, thereby helping to prime the colony to respond to an environmental perturbation such that the time required for the onset of the QS is reduced?

### **3.2.10: Stable maintenance of an induced subpopulation**

The maintenance of a responsive subpopulation is difficult to achieve, since it is an unstable state that requires very precise conditions for it to arise. As mentioned, growth within tryptone medium at 30°C produces individual cells that exhibit a burst of response, so by lowering the temperature, the responding subpopulation might stabilize. However, temperature is very difficult to modulate effectively and precisely. Exogenous induction in the presence of 20mM glucose induced a stable subpopulation, but the scenario is unnatural, and saturating levels of exogenous AI would negate any benefit that the responding subpopulation would produce. However, it does provide a clue as to how a stable subpopulation could be obtained. Since high levels of glucose could partially repress LuxR and suppress the effects of high levels of AI, if both were reduced in a proportionate manner, such that AI levels are similar to endogenously produced levels, perhaps when coupled with a correspondingly low level of glucose, it could achieve a similar effect. In addition, lowering the glucose concentration from 20 mM to 10 mM in the previous section enabled an increase in the number of chambers that reached the bistable regime, which consisted of subsets of induced cells amongst a population of uninduced cells. Therefore,

we speculated that glucose concentration might be the key to achieving a stably induced subpopulation. Since the level of glucose required might be within a narrow range, we decided that the use of a gradient-generating microfluidic device would provide the easiest means of screening for a concentration that would support a sustained induced subpopulation. The gradient-generating device utilizes a “Christmas tree” design [87], which involves a series of branching serpentine channels that performs serial dilution by continuously splitting and recombining flow streams that originated from two inputs (Figure 3.8A). In our design, the gradient-generating region can generate linearly-graded doses of a diffusible molecule spanning the concentration of the two inputs, thus providing a high throughput way to screen for a suitable concentration (Figure 3.8B). The channels downstream of the gradient-generating region are connected to chamber arrays consisting of all the chamber configurations with short capillaries, resulting in 12 chamber configurations. There does not appear to be a difference between the same chamber type in different positions (Figure 3.8C-F). The height of the chambers was reduced to 0.7  $\mu\text{m}$ , which slightly clamp down on the cells and reduce the growth rate marginally, to aid in the maintenance of the subpopulation. This fine-tuned the growth rate, in a more precise way that media cannot, which prevents the complete decay of response in the subpopulation once they had become induced.

### **3.2.11: Acceleration of onset by an induced subpopulation**

When cells were grown in 8 distinct glucose concentration doses spanning 0 and 6 mM in tryptone medium within the gradient generating device, it elicited a wide spectrum of responses ranging from complete presence to complete absence of induction within the



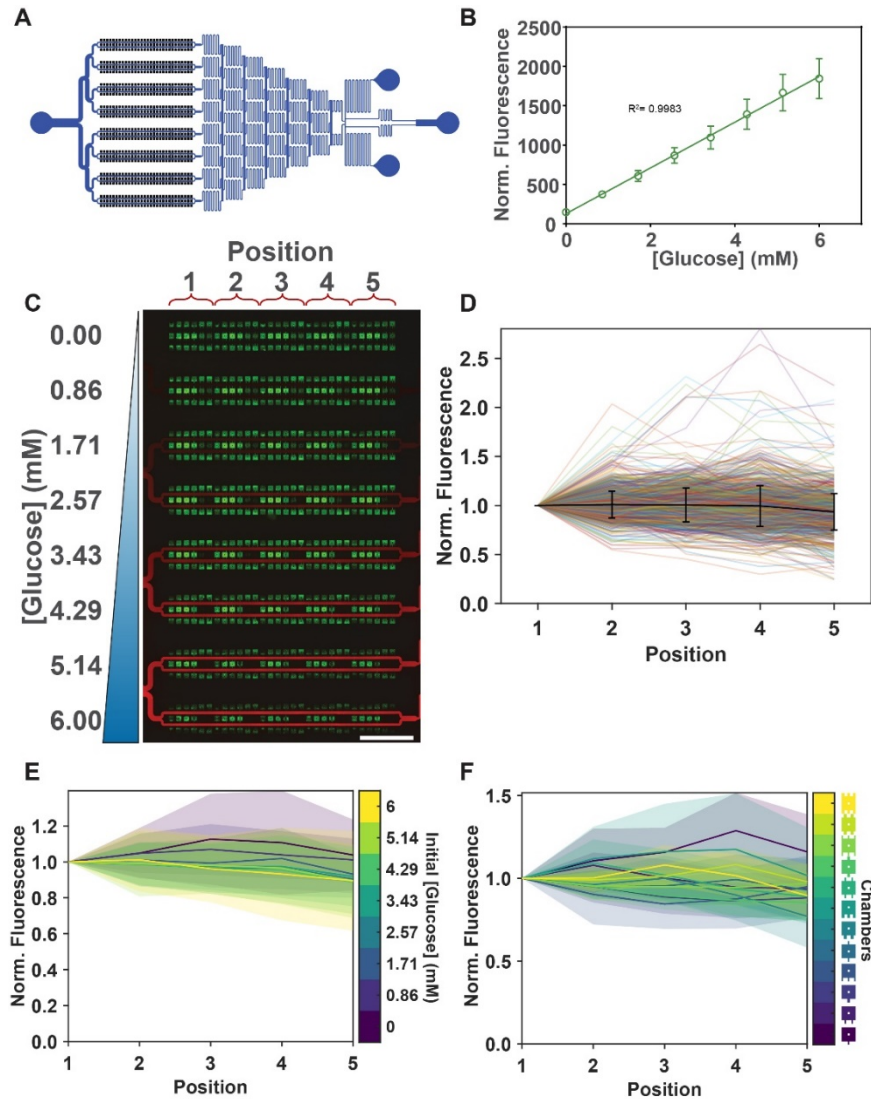


**Figure 3.8: Microfluidic device for screening conditions optimal for emergence of induced subpopulation.** **A**, Diagram of gradient-generating microfluidic device with 12 chamber configurations (short coupling channels). **B**, Distribution of dye fluorescence intensities within the flow-through channels of the 8 linearly-graded doses ( $n=16$ , from 8 independent experiments). **C**, Fluorescence micrograph of gradient generating device, with positions of chamber clusters indicated. Scale bar,  $500\ \mu\text{m}$ . **D**, Comparison of response intensity between the different positions, for all chamber configurations and dose concentrations. **E**, Comparison of response intensity between the different positions, for all chamber configurations across different dose concentrations. **F**, Comparison of response intensity between the different positions, for all dose concentrations across different chamber configuration. (mean  $\pm$  SD)

chamber configuration with the highest diffusive coupling (Figure 3.9A-C). We found that in the 0-0.86 mM range of glucose concentrations, the cells in the colonies were fully

induced, whereas in the 1.71-6 mM range, we observed bi-stable responses, with chambers showing different fractions of induced cells that were stably maintained for at least 40

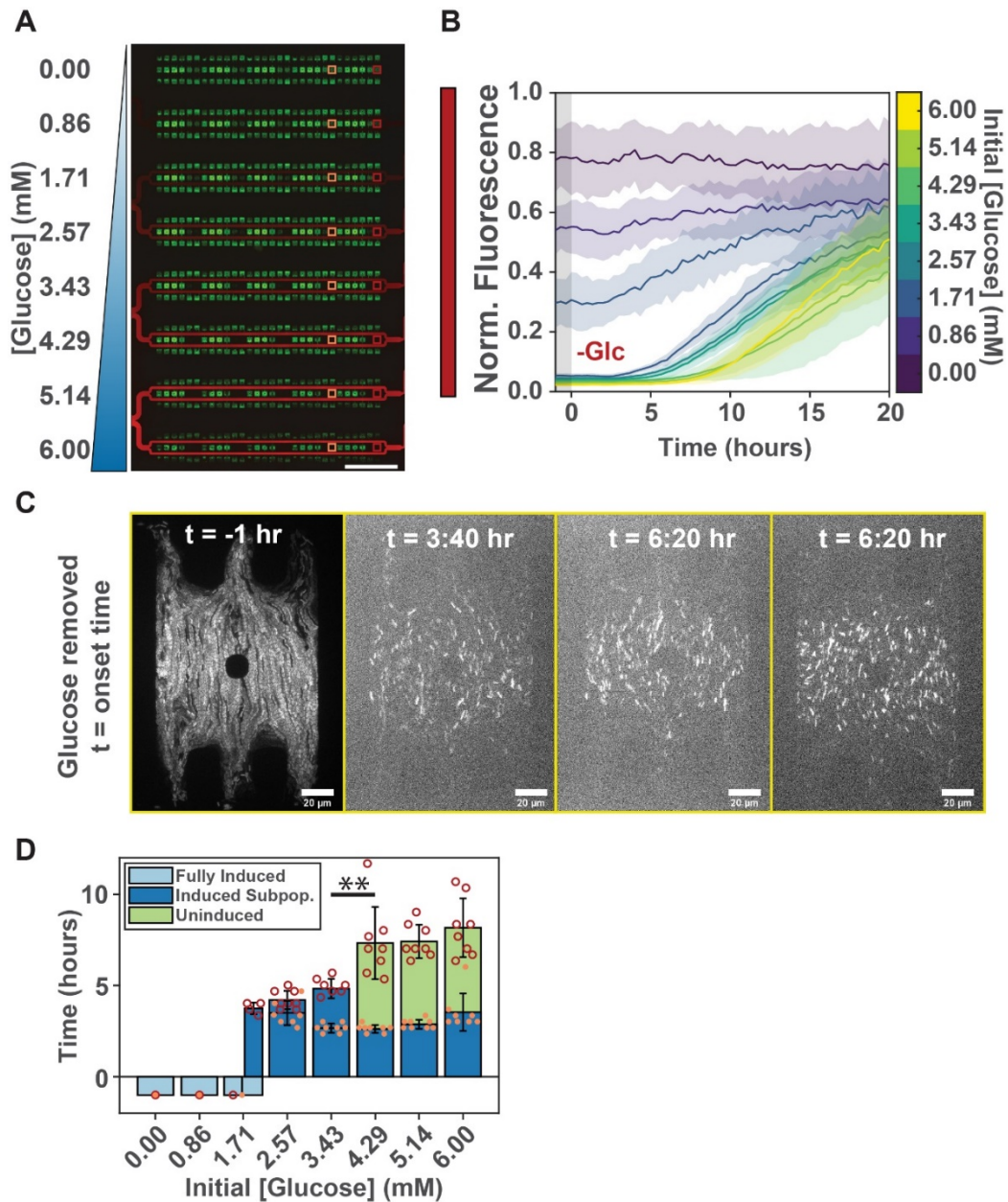


**Figure 3.9: Memory of QS-conductive environment can accelerate subsequent QS onset.** **A**, Fluorescence micrograph of gradient-generating device, with chambers of interest indicated in red boxes, downstream chambers in orange boxes and the gradient visualized in red. Scale bar, 1 mm. **B**, Response dynamics over 24 hours after glucose removal ( $n = 8$ ). **C**, Representative fluorescence micrographs of 4 dose conditions at the onset time after glucose gradient was removed. Scale bar, 20  $\mu\text{m}$ . **D**, Onset time of chambers exposed to different initial concentrations of glucose. ( $n = 8$ ,  $**P < 0.01$ , two tailed Student's  $t$ -test). (mean  $\pm$  SD)

hours after initial onset (Figure 3.9D). In the case of 1.71 mM, the bi-stability resulted in either complete or partial induction, while chambers in the 4.29-6 mM range contained either partially induced or completely un-induced cell populations. The stably induced subpopulation can be observed within the filmstrip as a small collection of cells that are induced amongst a sea of uninduced cells. Throughout the 40 hours in which the stably induced subpopulation was maintained, there is significant turnover of the subpopulation, as induced cells exhibit loss of response as they multiply or are pushed out of the chamber, but uninduced cells also become induced, indicating the secreted AI produced conditions suitable for sustaining a stably induced subpopulation. This is also observed in the kymograph as streaks of signal, which show the cells that are induced to a higher level as they emerge and gets pushed out the chamber (Figure 3.8E). In the two lowest concentrations of 0 and 0.86 mM, full induction of the colony was observed, serving as the positive control, whereas some chambers in the three highest concentrations of 4.29, 5.14 and 6 mM did not exhibit any induction, serving as the negative control. This range of distinct responses allowed us to examine whether and how the presence of different fractions of induced cells would affect the QS response.

Since the AI produced by the induced subpopulation reached a high enough level such that it can sustain itself in the presence of significant turnover, we wonder if the level of AI could also aid in the induction of other cells when conditions become conducive to onset. Since we have shown that onset of induction to be dependent on a balance of AI and LuxR, the additional AI could potentially reduce the level of LuxR necessary for induction to occur, which, by extension, would also reduce the time necessary to accumulate that lower

level of LuxR, and thus, lowering the temporal threshold and the overall time required for induction. In order to test this, the glucose gradient, which maintained a stable steady state for at least 40 hours within each dose condition, was removed, making the environment

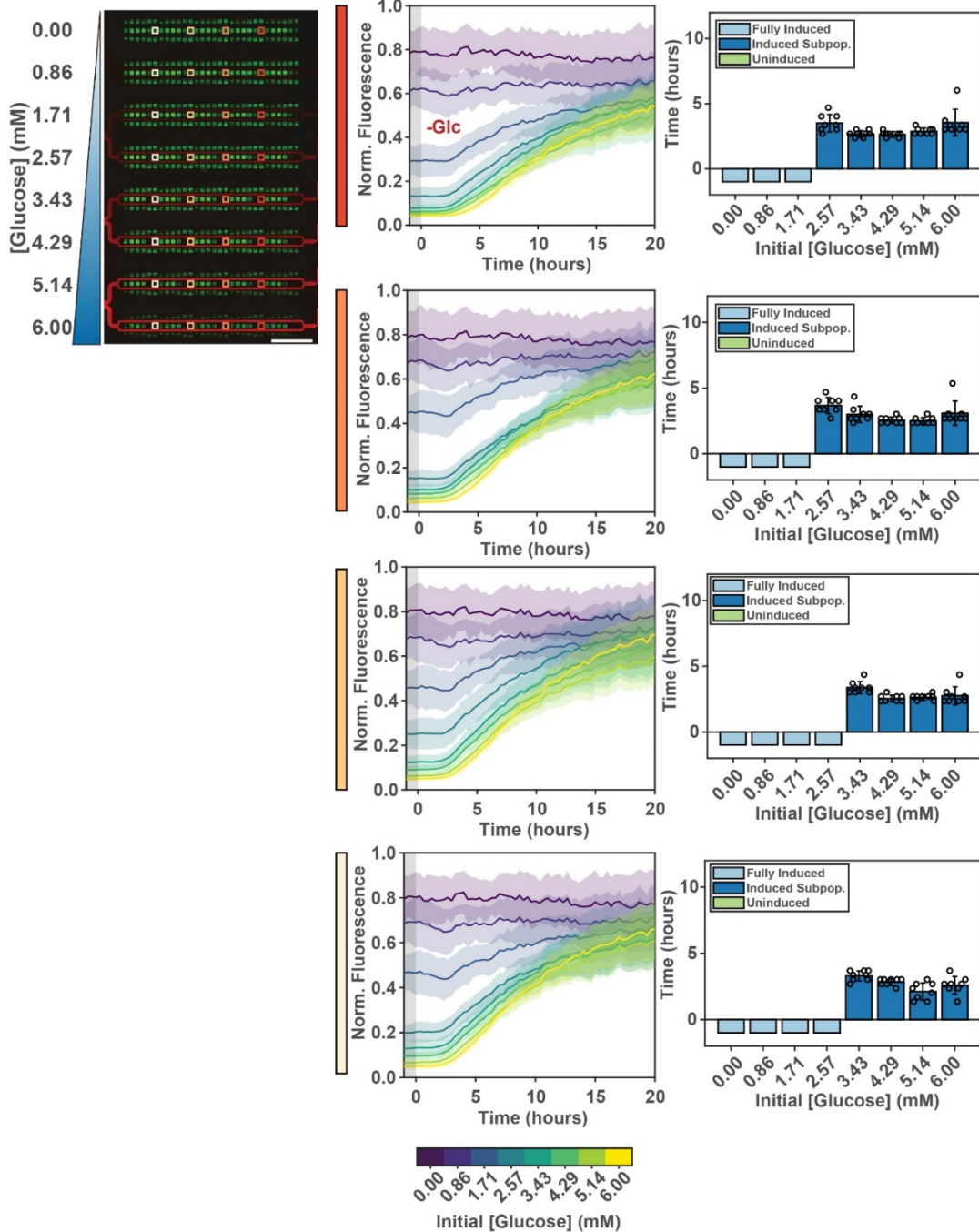


**Figure 3.10: Response dynamics within various initial glucose concentrations and positions.** Plots of response dynamics with corresponding onset times for chambers with the highest diffusive coupling at different positions and initial glucose concentrations. Scale bar, 500  $\mu\text{m}$

conducive to a QS induction response within all the conditions. Glucose removal from all conditions resulted in the complete induction for all chambers, but with distinct onset times (Figure 3.9A-C). In all cases, populations with an initially induced subset of cells underwent significantly earlier inductions of QS response than populations with initially uninduced cells (Figure 3.9D, 3.10). This suggests that the AI produced by the induced subpopulation was adequate for reducing the LuxR necessary for the onset to occur within other uninduced cells, thus, allowing for a faster onset time as compared to the time required for a population of all uninduced cells to become induced. This result was consistent with AI-mediated cell-to-cell communication from the induced subset of cells pre-conditioning the rest of the uninduced cells in the population and thus promoting a quicker QS induction following the onset of adverse conditions. These experiments suggested that if the fitness of the population is coupled to the QS onset, the presence of the persistently induced sub-population can provide a selective advantage to the whole population, enabling faster response of the whole population. Overall, the results in this study suggest that nutrient sensing can contribute additional layers of regulation in QS by defining spatial and temporal control mechanisms based on the growth-mediate balance of synthesis and dilution of QS components, which can complement the cell-to-cell communication underlying QS and enable non-autonomous cell behavior and the associated fitness benefit.

### **3.3: Discussion**

The existence of a threshold based in time has tremendous implications, such as the ability to filter out transient signals so as to only respond to sustained inputs. Since the induction

of a QS response involves the complete change in gene expression profile, it represents a significant commitment by the cell, and a tremendous investment of resources to mount a QS response. If a cell was sensitive to every perturbation in the environment, the initiation of a QS response might occur in situations where it is not optimal, which might place the cell in a disadvantageous position in comparison to other surrounding cells. The ability to filter out and disregard noisy or even short transient signals allows the cell to evaluate the environmental conditions and respond only when it is certain of the nature of the signal. The temporal threshold also imparts cells with the ability to react to changes in the environment, thereby, adjusting the propensity to respond based on the current environmental conditions. A long onset time often occurs in conditions with high growth rates, which might be indicative of conditions that may not be optimally advantageous for the partaking of QS-coordinated activities. This endows cells with the ability to filter out and ignore transient conditions which might be somewhat conducive to the onset of QS response, but might not be sustained, so it provides cells with a longer window with which to decide whether to commit to a response.

The spatial response gradients within colonies might also be explained by a similar cost and benefits analysis as the one used to explain the modulation of onset and intensity of QS response within different media conditions. Analogous to the shorter onset time observed in poor nutrient conditions, which suggest that the QS-mediated adaptive responses might be needed urgently, colonies in poor nutrient conditions might be spatially organized in their response. Extremely starved cells might prefer to conserve resources while allowing better-fed cells to induce QS-associated adaptive responses, which are often

spatially localized to the colony periphery and can function as a protective shell. On the other hand, similar to cells that have long onset times when grown in good nutrient conditions, cells within environments permissive for high growth rate may not need adaptive responses, allowing higher QS responses in slower growing cells, often spatially localize to the interior, to serve as a reserve of induced cells.

A subset of induced cells can represent bet-hedging, a form of response diversification strategy which can impart a fitness benefit by enabling a small number of cells to anticipate and survive sudden catastrophic environmental changes at the expense of the majority of the population. Diversification of the population into subsets of unresponsive and responsive cells occurs via positive feedback regulation, which is present in QS. However, unlike the usual hedging-of-bets strategy, the non-autonomous nature imparted by cell-cell coupling through secreted AI can allow the induced subpopulation, which can anticipate the environmental change, to stimulate the uninduced cells. This allows the uninduced cells to avoid the metabolic costs associated with the initial QS induction but still enable the expression of QS-associated adaptive response when needed. In a sense, this represents a type of “education” of uninduced cells by the induced ones, providing the intercellular communication with a specific meaning. Furthermore, the conditioning of uninduced cells by a subset of induced cells has the additional benefit of lowering the temporal threshold to QS onset via AI-based cell-cell communication. The resulting higher overall population responsiveness can increase the population fitness vs. the populations devoid of such cell “education” capabilities. Overall, environmental conditions can be important factors in regulating QS onset and propagation spatially and temporally.

### **3.4: Methods**

Please refer to sections 2.4-2.5 for methods pertaining to this chapter.



# Chapter 4: Self-imposed mechanical stress can induce biofilm formation

## 4.1: Introduction

Bacterial cells are known to seek out protective niches such as micro-cavities [77, 89] or the cytosol of host cells [90, 91] that can effectively shield the cells from the adverse conditions of the surrounding environment. As a result of the spatial isolation, such colonies can grow to high densities within close proximity of one another, which can lead to the emergence of various forms of collective cell behavior as a result of both biological responses and mechanical effects [11, 59, 92-95]. Uropathogenic *E. coli* that can invade epithelial cells lining the lumens of the urinary tract and form intracellular bacterial colonies (IBCs) constitutes one such example of confined bacterial colonies. The ability of these *E. coli* to infect epithelial cells can hide the potential immune triggers within the host cell cytosol, allowing the bacterial cells to undergo continuous cycles of invasion and dispersion [90, 91] that causes the recurrence and persistence of bacterial urinary tract infections (UTIs). These IBCs also have pod-like 3-D appearances and express various extracellular matrix components, including exopolysaccharide (EPS) and protein fibers (e.g., curli) [96, 97] that is characteristic of bacterial biofilms. Expression of biofilm-associated factors can confer the bacterial colonies protection by reducing the effect of antibiotic treatment through the formation of effective penetration barriers that hinder the penetration of the drugs into the core of the colony [98, 99]. However, the protective isolation of the cytosol that can facilitate collective behavior comes at a cost of mechanical constraining of colony growth and declining access to nutrients, which can lead to onset

and buildup of stresses on the colony that is further compounded by the expansion within increasingly viscous environment from the expression of matrix components and the dense cell packing. While mechanical interactions are known to be crucial for the transition from 2 to 3-dimensional bacterial colonies in a process known as buckling [100, 101], it is unclear how a tightly packed, confined population would respond to an increasing buildup of self-imposed mechanical stress. The interplay between the benefits and disadvantages of the intracellular biofilm formation has likely defined the evolutionary pressure on both bacterial invasion and the host responses. However, the complexity of the interaction between the host and IBCs has restricted our understanding of the onset of the formation of biofilm pod-like structures and the associated costs and benefits. In this chapter, we modeled the emergence of IBCs using a series of simple but highly controlled environmental culture conditions, focusing in particular on the role of mechanical stresses stemming from colony expansion within confining environments.

## **4.2 Results**

### **4.2.1: Confined growth leads to self-generated pressure buildup**

We previously achieved the growth of densely packed bacterial colonies within microfluidic chambers that were connected to media-supplying flow-through channels through channels that were tall enough to allow for the diffusion of nutrients, but shallow enough to prevent the escape of cells [58]. While this design, coupled with the rigidity of the chamber walls, achieved the spatial confinement and dense packing of cells that is required to study the effects of self-imposed mechanical stress on the expanding bacterial colonies, it does not provide a method to precisely measure the pressure that is generated

from the continued growth of the cells, thereby preventing the study of the effects of self-induced mechanical stress. However, by modifying the design of the device by introducing an additional channel on top of the growth chambers, it converts the roofs of the chambers from rigid boundaries that do not readily deform into a flexible elastic membrane that enables the assessment of the mechanical stress exerted by the bacterial colonies (Figure 4.1A). Because PDMS, which constitutes the device as well as the membrane, is highly flexible, the continued growth of a colony is expected to exert forces and push on the membrane, causing deformation and displacement of the membrane away from the chamber. This displacement can be measured with 3-D reconstruction of individual plane images obtained with confocal laser scanning microscopy (CLSM). By filling the chamber layer with a green fluorescent dye and the top channel layer with a red fluorescent dye maintained at atmospheric pressure, we can apply a range of known pressures to the chamber layer and cause the deformation of the membrane roof due to the difference in pressure (Figure 4.1B). By measuring the upward displacements of the roofs near their centers (where the displacements were maximal), we calibrated the roof deformations as a function of applied pressures in chambers with different sizes, allowing us to use this calibration to evaluate the pressures generated by colonies growing in these chambers (Figure 4.1C). The experimentally measured roof displacement values and the corresponding pressure values were congruent with the linear dependences predicted by mathematical modeling that is based on a plate-theory model [102] (Figure 4.1D).

After loading cells into the chamber, five to seven hours of subsequent growth was required to fill the chamber completely, after which the continued growth of the colony resulted in

detectable deformations of the chamber roof (Figure 4.2A). The degree of roof deformation

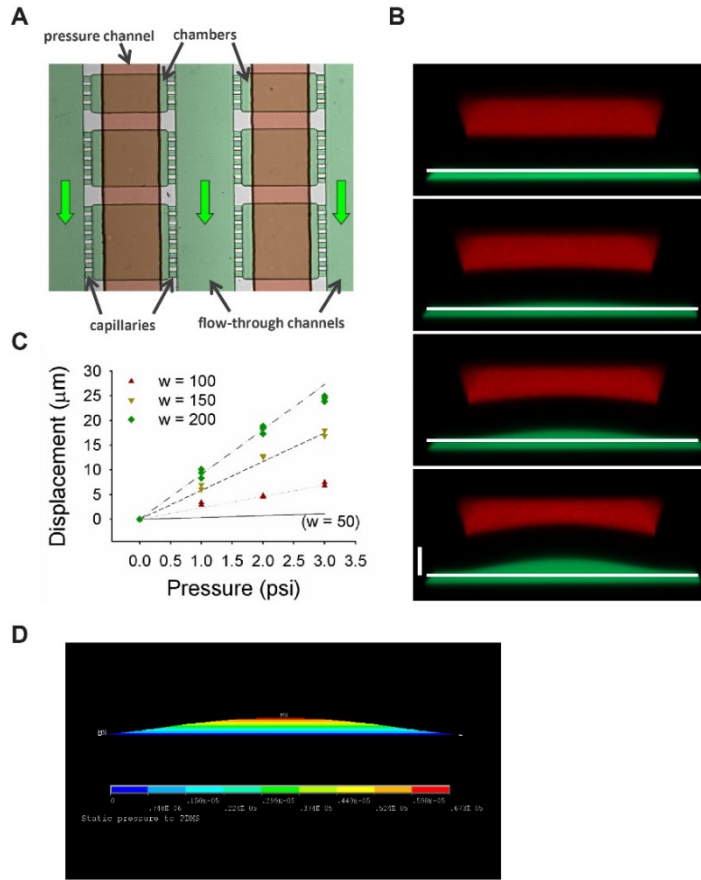


**Figure 4.1: Microfluidic device for measuring pressure from growth within confinement.** **A**, A micrograph of a portion of the chamber array in the microfluidics device. The chamber and flow-through channel layer has been highlighted in green, while the overlaying channel layer used to create the deformable chamber roof has been highlighted in red. Scale bar, 200  $\mu\text{m}$ . **B**, The deformation of a chamber roof increases as progressively elevated uniform external pressure is applied to the chamber layer during calibration, as visualized with 3-D reconstruction from confocal imaging, using solutions of fluorescent dyes Alexa Fluor 488 (green; chamber layer) and Alexa Fluor 555 (red; pressure channel). Scale bar, 20  $\mu\text{m}$ . **C**, A representative calibration plot is obtained by plotting the displacement of the thin membrane as a function of the applied external hydrostatic pressure. The lines super-imposed onto the data points are obtained from the analytic and simulation analysis of the corresponding thin plate deflection theory, described in the Methods section. **D**, numerical simulation of the deformation of a membrane that is 20  $\mu\text{m}$  thick, 150  $\mu\text{m}$  wide and 160  $\mu\text{m}$  tall (long), and has the elastic modulus (corresponding to that of PDMS) of  $E = 0.35\text{MPa}$ , under 1 psi pressure. The resulting membrane deformation (deflection) is approximately 5  $\mu\text{m}$ . The normalized stress values are color coded. The results are fully consistent with the predictions of the plate deformation theory provided in the text. The simulation was performed in ANSYS 10.0.

can be measured as a time course and the corresponding evolution of pressure values can be obtained from the mapping of displacement vs. pressure obtained from the calibration (Figure 4.2B, C). We found that multiple bacterial species, including uropathogenic strain of *E. coli* (CFT073), cystic fibrosis-associated *P. aeruginosa* and gram-positive spherical-shape *S. cohnii* deformed the flexible roofs of the chamber in manners that are consistent with the plate theory model, and can all generate pressures excess of  $\sim 1.5$  psi ( $\sim 10$  kPa) (Figure 4.2D). The pressure of 1.5 psi is comparable to the levels required to induce osmotic bursting of eukaryotic cells (e.g.,  $\sim 1.0$  psi,  $\sim 6.9$  kPa for alveolar epithelial cells, and  $\sim 0.6$ ,  $\sim 4.1$  kPa psi for red blood cells) [103, 104], and for an estimated cell footprint of  $\sim 1 \mu\text{m}^2$ , this pressure corresponds to a force of  $\sim 1$  nN. These results suggest that expanding bacterial colonies are capable of generating forces sufficient to rupture an intact membrane of the host-cell from inside, adding the mechanical bursting out of a host cell to the list of previously proposed possible dispersal mechanisms [105-107]. However, these pressures are lower than the estimated turgor pressure within bacterial cells (4.4-14.5 psi, 30-100 kPa) [108], which is often considered as the potential pressure needed to cease bacterial growth. In comparison, IBCs behaves in a similar manner, with rapid initial expansion followed by a growth arrest at pressures that are below the bacterial turgor pressures [109]. The arrest of cell growth at these relatively low pressures suggest that the cause might be related to adaptive responses by the colonies to the mechanical stress, as opposed to the inability of cells to expand against the membrane further. A possible explanation for the colony arrest at low pressures is due to the increasingly viscous environment around the cells as a result of increasing cell density and transition to a biofilm-like state, which could lead to stresses and hinder growth independent of the

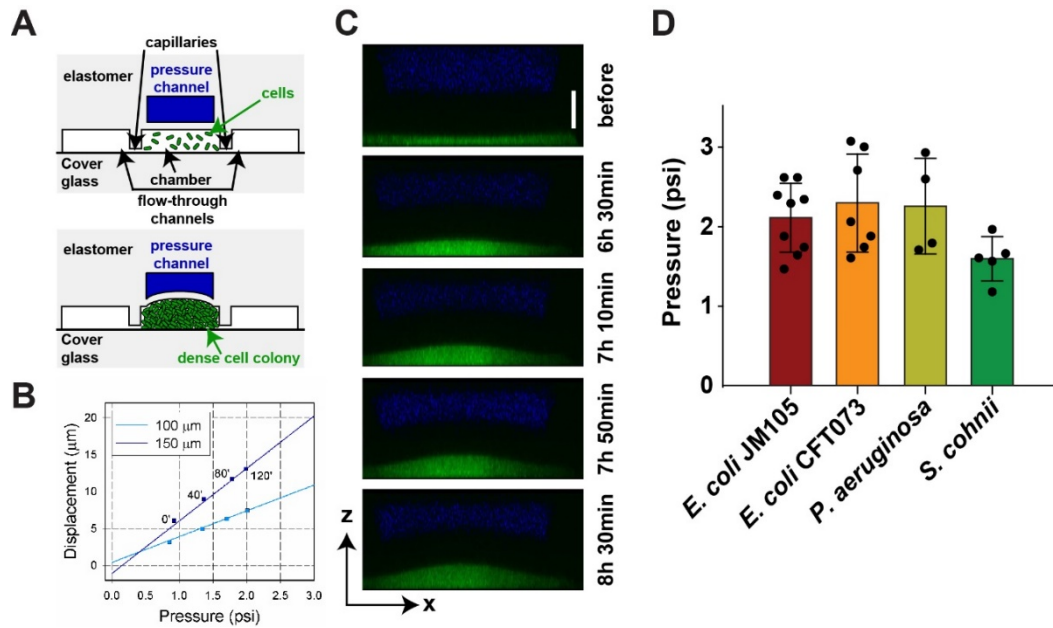


**Figure 4.2: Bacterial growth within confinement can lead to buildup of pressure.** **A**, Schematic cross-section of the microfluidic device, illustrating the deformation of the flexible roof due to bacterial colony growth. **B**, The dynamics of pressure increase generated by expanding *E. coli* colonies confined in chambers of different widths. The values are estimated from the corresponding deformation of PDMS membranes forming the roofs of the microchambers. Pressure values were determined from the displacements of the membrane in z-direction at time points 0 min, 40 min, 80 min, 120 min of growth after the chamber was filled with *E. coli* cells. The calibration procedure is described in the text and shown in Supplementary Fig. 1c. The results were independently validated by confocal imaging experiments at randomly selected time points, as shown in Supplementary Fig. 6. The measurements were performed in 100  $\mu\text{m}$ - and 150  $\mu\text{m}$ -wide chambers. **C**, The deformation of the roof [black area between blue (Alexa Fluor 647) and green (GFP-expressing *E. coli*) layers] is visualized with CLSM. Scale bar for the vertical dimension, 20  $\mu\text{m}$ . **D**, Maximum pressures produced by different bacteria; *E. coli* JM105 (n=9); *E. coli* CFT073 (n=7); *P. aeruginosa* (n=4); *S. cohnii* (n=5).

pressure value. Therefore, we sought to further explore the colony behavior in response to increasing self-induced mechanical stress as a result of growth within confinement.

#### 4.2.2: Self-generated pressure buildup leads to biological stress response

A common cellular response to stresses of various types, including physical stress, is the differential regulation of the heat shock genes, including *rpoH*, which encodes for the heat-

shock sigma factor  $\sigma^{32}$  [110]. To see whether the self-induced mechanical stress that arise from growth within confinement can trigger the induction of *rpoH*, we used a laboratory strain of *E. coli* (JM105) expressing GFP under the control of the *rpoH* promoter, which can generate similar levels of pressure as compared to the other strains we tested. Induction of *rpoH* was determined by measuring the changes in GFP fluorescence per unit volume, obtained by normalizing the total fluorescence intensity measured with wide-field microscopy (WFM) to the volume of the chamber measured with CLSM at the same time point, as well as the changes in GFP fluorescence within individual planes captured using CLSM. We found that prior to roof deformation, the normalized fluorescence intensity values did not reveal detectable induction of *rpoH* and remained at basal levels throughout the filling of the chamber by the cells. However, upon chamber filling, the subsequent deformation of the chamber roof, which corresponded to a pressure value of  $\sim 0.75$  psi ( $\sim 5$  kPa), coincided with a detectable upregulation of the *rpoH*, as indicated by the increase in normalized fluorescence intensity (Figure 4.3A, B). Continued deformation of the chamber roof led to an increase of the volume-normalized fluorescence intensity by as much as 100% with respect to the initial basal value without roof deformation. This increase in *rpoH* expression after roof deformation was also observed within individual plane analysis using CLSM (Figure 4.3C, D). Therefore, these results indicate that the onset of a biological stress response occurs as a result of the self-induced mechanical stress that results from growth within confinement.

#### **4.2.3: Mechanical stress due to colony expansion leads to biofilm formation**

Since *rpoH* upregulation is known to be connected to the onset of biofilm formation in *P. aeruginosa* [111], we explored whether the confinement-induced mechanical stress that

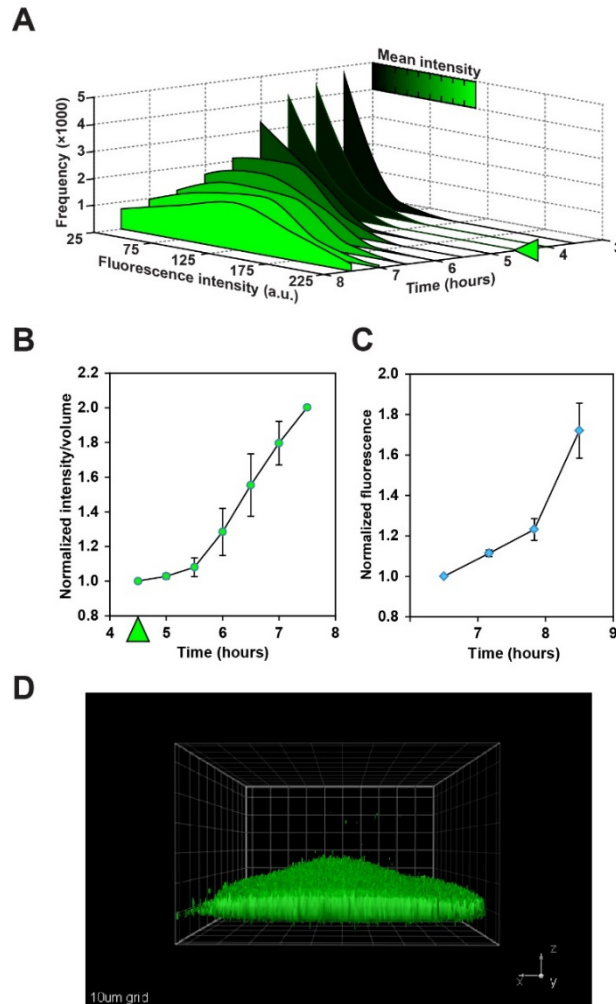


**Figure 4.3: Pressure buildup as a result of confined growth leads to biochemical stress response.** **A**, Distributions of *rpoH* expression-reporting GFP fluorescence intensity per pixel in a WFM image of a chamber (in arbitrary units ranged 25 to 225) at various time points, starting 3.5 hours after seeding cells into the chamber. The arrow ( $t=4.5$  hours) indicates when the chamber is completely filled with cells. The color of the plot shows the mean intensity at the corresponding time point. **B**, The integral fluorescence of bacterial colony in the chamber divided by the chamber volume measured at the same time point. The data is normalized to the time point just before the roof deformation becomes detectable ( $t=4.5$  hours in Fig. 1d) ( $n=3$ ). **C**, GFP expression due to *rpoH* upregulation measured from *xy*-sections of confocal imaging. The data was normalized to the time point when roof deformation started to become measurable ( $t=6.5$  hours in Fig. 1b, indicated by the blue arrow) ( $n=3$ ). Error bars are SD. **D**, A 3D reconstruction of a confocal *z*-stack of an *E. coli* colony expressing GFP under the *rpoH* promoter control within a fully deformed chamber.



resulted in *rpoH* expression within our device would cause uropathogenic *E. coli* (CFT073) colonies to transition to a biofilm state and exhibit biofilm-associated markers. We

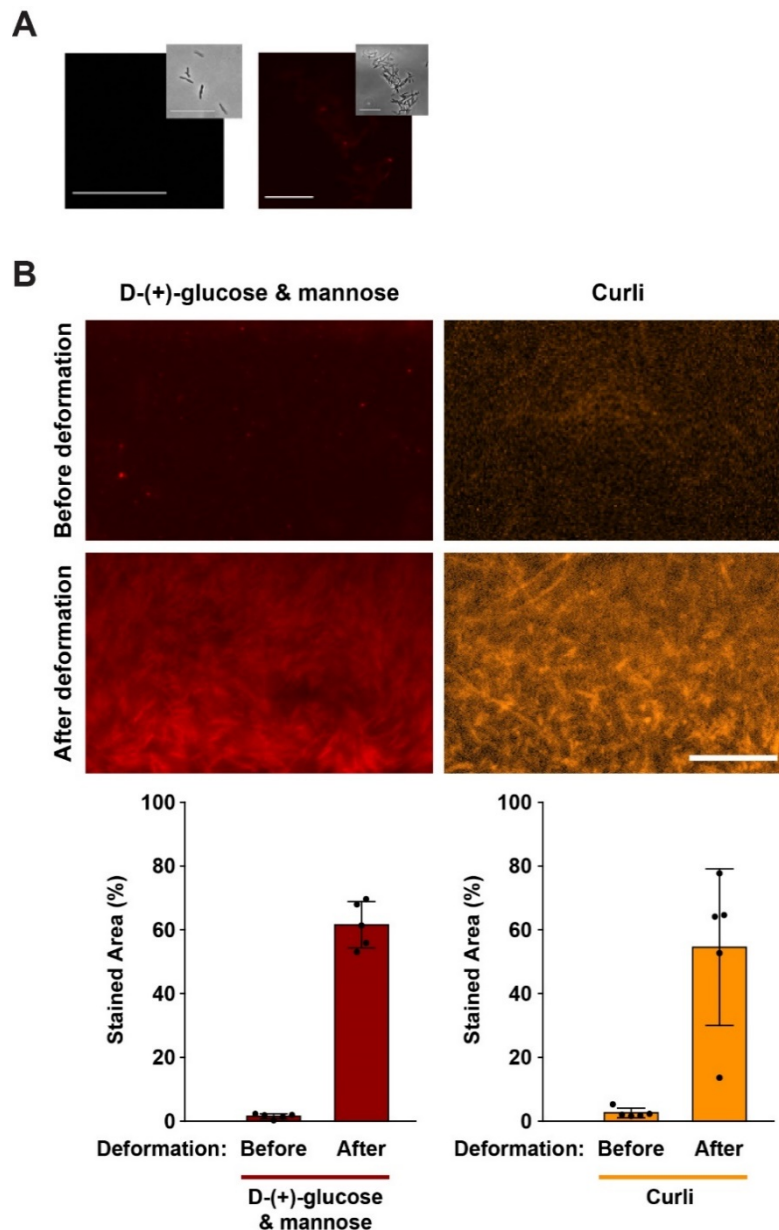


**Figure 4.4: Pressure buildup and stress response leads to expression of biofilm markers.** **A**, Epi-fluorescence imaging shows exopolysaccharide (EPS) expression in individual cells (left) or cell clumps (right), as indicated by rhodamine-labeled concanavalin A stain. Scale bar, 10  $\mu$ m. **B**, Expression of biofilm-associated cell-surface structures, EPS D-(+)-glucose and mannose groups (red) and curli (orange), as detected using rhodamine-labeled concanavalin A (10  $\mu$ g/ml) and Congo Red dye (10  $\mu$ g/ml), respectively, before (top row) and after (bottom row) roof deformation in uropathogenic *E. coli* populations. Scale bar, 10  $\mu$ m. Bar graphs show major increases in expression of biofilm-related factors after roof deformation (n=5). Error bars are SD.

examined two different types of such biofilm markers, exopolysaccharides (EPS) [96] and curli [97], using, respectively, rhodamine-labeled concanavalin A that specifically binds to D-(+)-glucose and mannose groups on EPS [112], and Congo Red dye that has a high affinity to curli structures on the cell surface [113, 114]. These markers are involved in intercellular adhesion crucial for initiation of biofilm formation [115, 116]. We tested for the expression of these known biofilm markers within individual cells and cell clumps, as well as bacterial-filled chambers before (after colonies grew for 5-7 hours, depending on chamber size and initial cell number) and after chamber roof deformation (after ~5 hours of growth past the point when the roof deformation first became visible, resulting in substantially deformed roofs). Comparison of the staining data revealed substantially higher levels of staining, corresponding to much higher levels of expression for both biofilm markers within the post-roof deformation case, suggesting that the biological stress response from the self-induced mechanical stress can trigger a transition to a biofilm-like state (Figure 4.4). Furthermore, we discovered a high level of spatial correlation between the 2-D distributions of *rpoH* upregulation and EPS expression within the bacterial colonies, which both displayed a characteristic butterfly shape, further supporting the hypothesis that local stress triggers *rpoH* expression and transition to a biofilm-like phenotype (Figure 4.5A).

#### **4.2.4: Biofilm formation is spatially correlated with stress response**

The butterfly-shaped pattern of *rpoH* expression could potentially arise from the two major sources of spatial non-uniformity in a growth chamber: the nutrient is only supplied through the two sidewalls adjacent to the flow-through channels, and the vertical

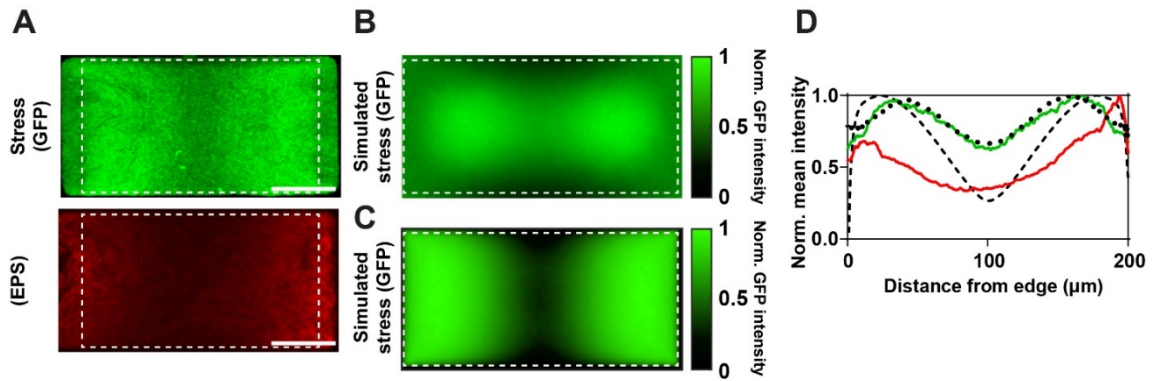


**Figure 4.5: Spatial correlation between expression of biofilm-associated cell surface structures and biochemical stress response.** **A**, Spatial distribution of GFP, as a reporter of *rpoH* expression, and of rhodamine-labeled concanavalin A (EPS stain) in *E. coli* JM105 after roof deformation. Dashed lines show boundaries of the deformable roof. Scale bars, 50  $\mu\text{m}$ . **B**, **C** (**B**) Agent-based and (**C**) mean field simulations of the stress response distribution reproduce the characteristic patterns observed in GFP and EPS expression. The intensity of green color encodes the stress response. **D**, The spatial correlation between the experimentally measured expressions of GFP and EPS and simulated stress responses (agent-based: black dotted curve; mean field: black dashed curve) further supports the connection between mechanical stress and biofilm formation.

displacement of the roof is maximal in the center of the chamber and zero near the side walls. Thus, we questioned whether these two spatial non-uniformities are enough to give rise to the spatial distribution of *rpoH* response, which we attempted to answer with two simple computational models (see Methods for details). In the first agent-based model, nutrient supply was modeled in a spatially non-uniform way by maintaining nutrient levels constant at opposing chamber boundary zones to mimic the supply by flow-through channels, and allowing diffusion and cellular consumption to define the local nutrient levels within the rest of the chamber. Growth rate was assumed to be proportional to the local nutrient levels, and expression of *rpoH* was in turn assumed to be proportional to the pressure and growth rate, because of mechanical stress that we hypothesize to result from growth in a crowded and increasingly viscous extracellular environment. The roof deformation profile was simulated according to the plate-theory model, [102] which was

confirmed by our experimental measurement. Simulation of the mathematical model incorporating these assumptions indeed resulted in the butterfly-shaped growth-induced distribution of stress response essentially identical to the experimentally observed profile (Figure 4.5B, D). The model also predicted the formation of a nutrient gradient from the supply sidewalls towards the interior of the chamber, which was confirmed experimentally with a cAMP-CRP (cAMP receptor protein)-level reporting strain [59, 117] (Figure 4.8A). Given that nutrient levels and growth rates are higher in regions proximal to the flow-through channels than in the interior chamber regions, coupled with the fact that maximal vertical displacement of the roof is in the middle, the overall bulk motion of cells was simulated to move from the periphery of the chamber towards the middle, where access to nutrients becomes even more restricted and cellular activity is expected to be further reduced. This collective cell motion was also observed experimentally. A second, mean field model that represented the process as a viscous fluid undergoing creep flow and incorporated identical assumptions, with an influx and efflux profile corresponding to the growth and roof deformation profiles, respectively, yielded similar results (Figure 4.5C, D). The agreement between the results of the simulations and experiments supports the model assumptions and provides further validation of the hypothesis that mechanical stress resulting from expansion of bacterial colonies in spatially confined regions can lead to formation of biofilm-like structures in uropathogenic *E. coli*.

To directly see whether mechanical stress can trigger the formation of biofilm-like structures, we transiently and rapidly increased the pressure in the pressure channel above the chambers when the chamber has been filled to a dense state with cells, but has not

expanded enough to develop the pressure necessary to deform the roof yet. The application

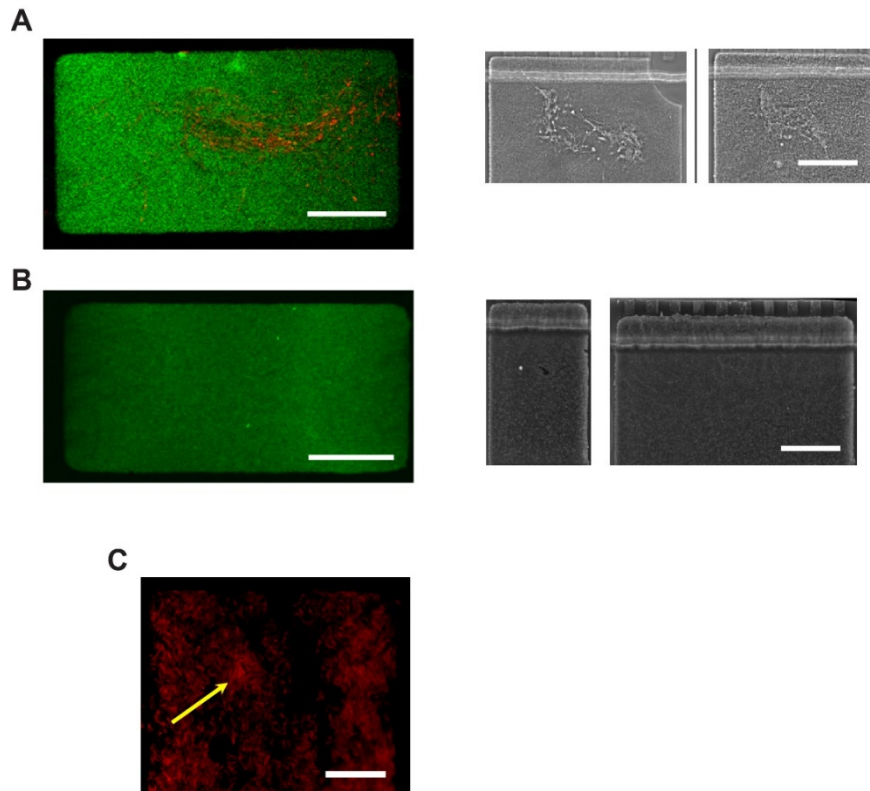


**Figure 4.6: Direct application of pressure.** A-C (A) Examples of GFP (under the control of the *rpoH* promoter) and rhodamine-labeled concanavalin A staining, and solid structure growth in growth chambers following their partial expansion with a transient inward membrane (chamber roof) deformation. The inward deformation was performed by increasing the pressure in the pressure channel to approximately 1 psi at the point of initiation of the outward deformation of the chamber roof, performed for 15 min. This was the time point immediately following the filling of the chamber with the expanding *E. coli* colony. The staining was performed after an additional hour of colony expansion following the inward deformation. The central region, where the staining is concentrated as visualized using confocal imaging, is the area of the highest inward membrane deformation, expected to lead to the highest amount of stress onto the cells. The even distribution of GFP is indicative of the additional input of the self-induced stress during the one hour of outward colony expansion. (B) The early stages of outward roof deformation as a result of cell growth, without initial roof invagination, also results in uniform GFP expression. Scale bars, 50 μm. (C) An example of a confocal image using rhodamine-labeled concanavalin A stain in a 150 μm -wide chamber following its complete expansion after a transient inward membrane (chamber roof) deformation. Note both the expected ‘butterfly’ pattern and the unusual increased staining at the central region, indicated by the arrow. The central region is the area of the highest inward membrane deformation, expected to lead to the highest amount of stress onto the cells.

of external pressure within the pressure channel above the chambers caused a pressure differential opposite of the one that causes the normal upward deformation of the roof, resulting in a downward deformation of the roof instead which presses on the bacterial colony. This invagination is localized in areas under the center of the membrane, where the displacement (and the pressure on cells resulting from it) was maximal. This transient invagination of the roof would mark a transition from a liquid-like property of the colony (allowing rapid relaxation of locally applied stresses throughout the colony leading to uniform stress distribution) to properties akin to jammed colloid states, where stress can remain local, leading to local stress response by the cells and ensuing formation of local biofilm-like structures. Removing the inward pressure on the roof allowed the colony to resume its grow and to produce biofilm markers in the center of the colony (Figure 4.6A). Because the colony had to expand to fill the chamber again, it led to reorganization of the colony and to a more uniform self-induced stress distribution, and ultimately to uniform *rpoH* induction (Figure 4.6B). This uniform distribution is also observed at the early stages of outward roof deformation from cell growth, where no roof invagination was applied. Interestingly, application of transient roof invagination coupled with growth until outward roof deformation resulted in the summation of the butterfly-shaped staining profile as well as staining in the center of the chamber where invagination and the pressure resulting from it was maximal (Figure 4.6C).

#### **4.2.5: Antibiotic tolerance due to biofilm as a penetration barrier**

A functional consequence of biofilm formation is increased antibiotic tolerance, which can be due to adaptive or passive mechanisms [118]. Adaptive mechanisms require the

expenditure of energy, such as the activation of protective cellular machinery in individual cells, including the expression of degrading enzymes, activation of efflux pumps, and reduction of metabolism [119, 120]. Passive mechanisms involve no expenditure of energy, relying on the extracellular biofilm matrix to act as a barrier and shield cells from antibiotic compounds, which can have strong affinity to EPS or other biofilm-associated molecules [121]. For instance, whereas some antibiotics such as fluoroquinolones can readily penetrate the biofilm matrix [122], positively-charged aminoglycosides are very ineffective in penetrating the negatively-charged EPS [123, 124]. To test for the formation of a negatively-charged penetration barrier, we used a DNA-binding, positively-charged fluorescent dye (SYTO 9) as a proxy for positively-charged antibiotics. We compared the penetration of SYTO 9 into uropathogenic *E. coli* (CFT073) colonies in the microfluidic device, as well as the propidium iodide (PI) staining for dead cells with compromised membranes following aminoglycoside antibiotic gentamicin challenge for 3 hours at a concentration 10 times greater than the minimal inhibitory concentration (MIC; as determined by an E-test outside the microfluidic device) at a low density in the exponential growth phase, and at high densities prior to and subsequent to roof deformation.

We found that SYTO 9 uniformly penetrated the chamber and stained the cells uniformly prior to the dense packing of the cells, which is consistent with PI staining results of dead cells following antibiotic treatment, which also displayed a relatively homogenous staining pattern (Figure 4.7). However, when the chamber is filled with cells at high density, but no deformation of the chamber roof is detectable yet, the PI staining of cell death following antibiotic treatment was restricted to regions proximal to the capillary channels (in the areas

containing more rapidly multiplying cells), while SYTO 9 staining was still relatively uniform (Figure 4.7). This suggests that although biofilm materials have yet to be

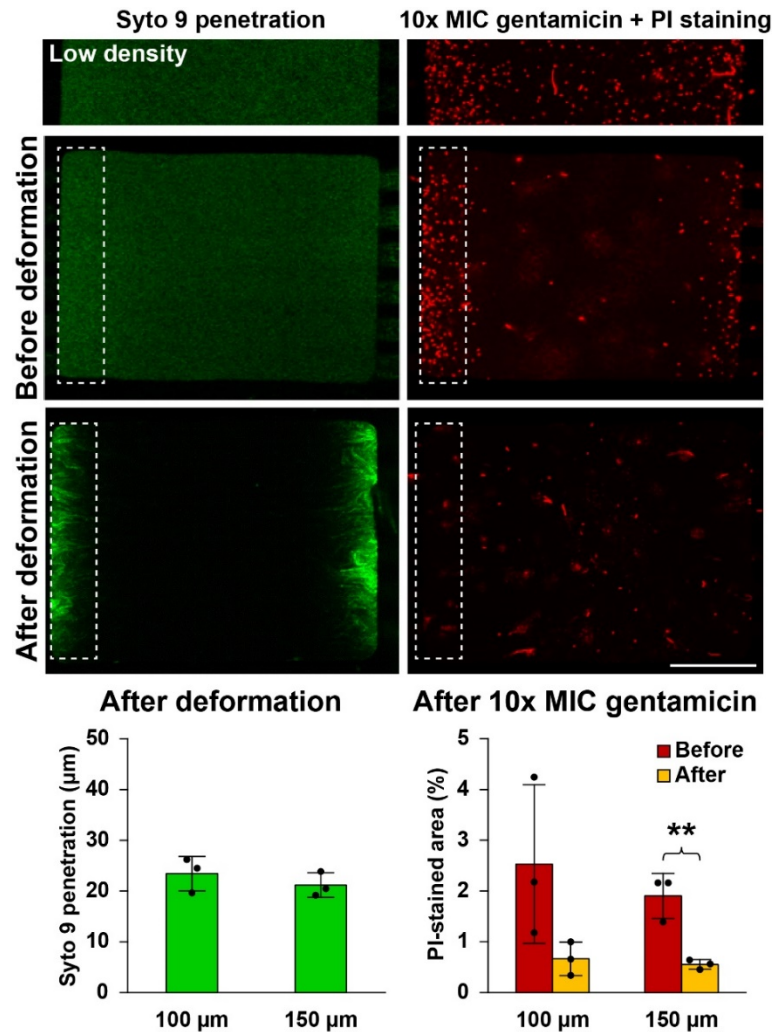


**Figure 4.7: Confinement-dependent formation of a selective penetration barrier confers increased antibiotic tolerance.** SYTO 9 (green, left) dye, mimicking positively-charged antibiotics was used to assess the penetrability of bacterial colonies at low cell density (top), high cell density before roof deformation (middle), and high density after deformation (bottom). Separately, antibiotic tolerance was assessed with 10x MIC gentamicin (15 µg/ml) treatment for 3 hours followed by PI (red, right, to stain dead cells with compromised membranes) staining under identical density conditions. Dotted line boxes indicate regions proximal to the flow-through channels. Bar graphs indicate extent of SYTO 9 penetration after roof deformation and the percentage of PI-stained areas in regions proximal to the flow-through channels after antibiotic treatment in 100 and 150 µm wide chambers. Error bars are SD (n=3); \*\*P<0.01; two-tailed Student's *t*-test. Scale bar, 50 µm.



produced, dense packing still leads to a certain degree of protection against antibiotic treatment due to the reduction of growth rates in the middle of the colony, but it still leaves the fast-dividing cells in the regions proximal to the capillary channels susceptible. However, continued growth of the colony to the point of roof deformation resulted in SYTO 9 penetration that was significantly reduced and restricted only to regions proximal to the capillary channels, while the PI-staining of dead cells has been reduced to negligible levels, which suggests the formation of the biofilm-mediated antibiotic penetration barrier (Figure 4.7). The extent of SYTO 9 penetration and antibiotic-mediated cell death did not depend on the chamber size, indicating that the penetration barrier was due to biochemical changes at the regions proximal to the flow-through channels. Alexa Fluor 488, a negatively-charged fluorescent dye that did not have affinity to extracellular structures, was able to uniformly penetrate bacterial colonies even after the roof became deformed, in contrast to SYTO 9 (Figure 4.8B). Overall, these results suggested that a hallmark of biofilm development – increased antibiotic tolerance – indeed becomes pronounced concurrently with biofilm marker expression within the chambers, revealing functional characteristics of the emerging biofilm-like structures.

#### **4.2.6: Biofilm formation due to self-generated stress within matrix-like environment**

While the microfluidic culture chambers enabled the precise control of the microenvironment around the colonies as well as the measurement of the level of self-induced pressure, which we were able to demonstrate can lead to the formation of biofilms with functional properties, it is not a realistic representation of what happens in nature since the colony may not experience appreciable mechanical stresses until it fills the entire

available space. However, in many cases, expanding bacterial colonies can experience mechanical resistance from very early stages of growth (e.g., during invasion and colonization of the host eukaryotic cells), where the nutrient supply and mechanical

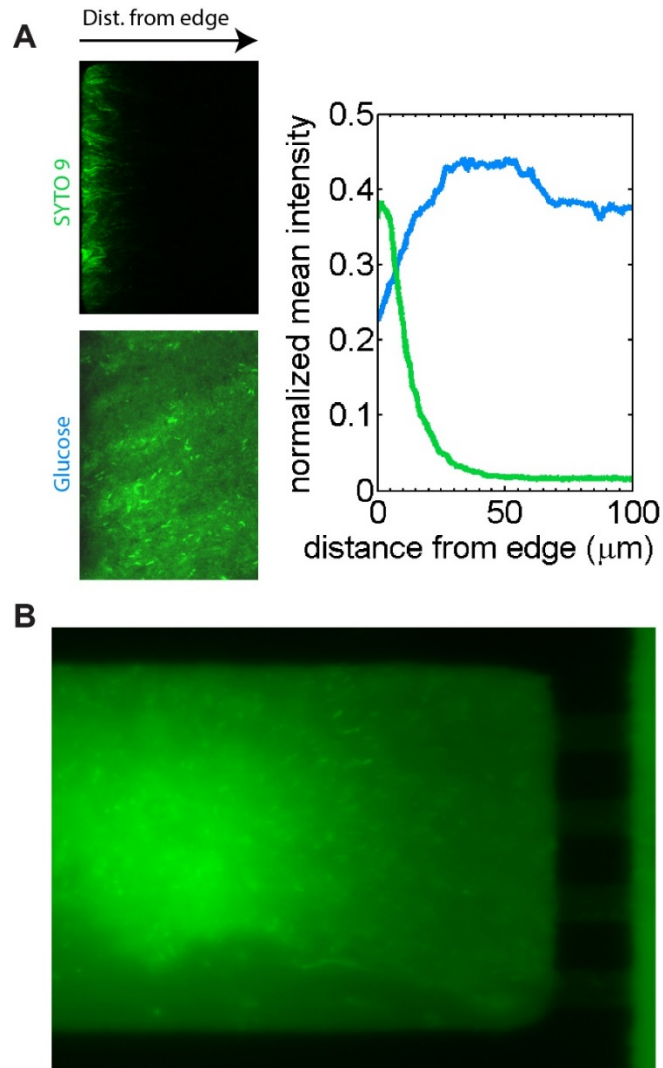


**Figure 4.8: Selective penetration of molecules into the colony.** **A**, Detection of a nutrient gradient from the supply towards the interior of the chamber, with a cAMP-CRP (cAMP receptor protein) level reporting strain expressing at low levels in regions proximal to the exits, and increasing in expression towards the interior of the chamber until a maximal level is reached. Scale bar, 50  $\mu\text{m}$ . **B**, Negatively-charged Alexa Fluor 488 penetrated the chamber in an uninhibited fashion, exhibiting higher levels of intensity towards the interior of the chamber due to the increase in volume as the roof was deformed. Scale bar, 25  $\mu\text{m}$ .

resistance of the surrounding medium (e.g., the matrix of the host cell cytoskeleton) can be much more isotropic, leading to spherical shapes of biofilm-like colonies [125].

We questioned whether the mathematical model we developed and validated for the expansion of biofilm-like colonies in microfluidic chambers can reveal insights into how such a biofilm-like colony might emerge. Therefore, we extended the computational model developed for the microfluidic chamber by using a linear-elastic model to approximate the expansion against an isotropically surrounding matrix and the gradually increasing pressure that arise from continuous colony growth. Simulation of such a model with these modifications suggest that initiation of *rpoH* expression can indeed occur early in colony development, when the population size is small, as a result of pressure incurred from continuous expansion against the increasingly stressed surrounding matrix (Figure 4.9A). While *rpoH* upregulation occurred at a higher level predominantly at the periphery, which was also the region of fastest cell growth due to unrestricted nutrient access, cell growth in the core of the colony declined due to gradual decrease in nutrient access as the colony expanded, leading to reduced *rpoH* expression. However, the increasingly sessile state of these cells within the core of the colony also impeded the dilution of the existing, highly stable GFP proteins, leading the simulated colonies to exhibit relatively spatially uniform levels of GFP in a sharp contrast to the steep spatial gradients of GFP in the butterfly-shaped patterns in the microfluidic culture chambers. Therefore, the simulation results suggested that an isotropic and spatially uniform confining environment could make the increasingly sessile core cells express stress-related factors prior to their transition to dormancy, thereby causing stress response at all stages of colony development.

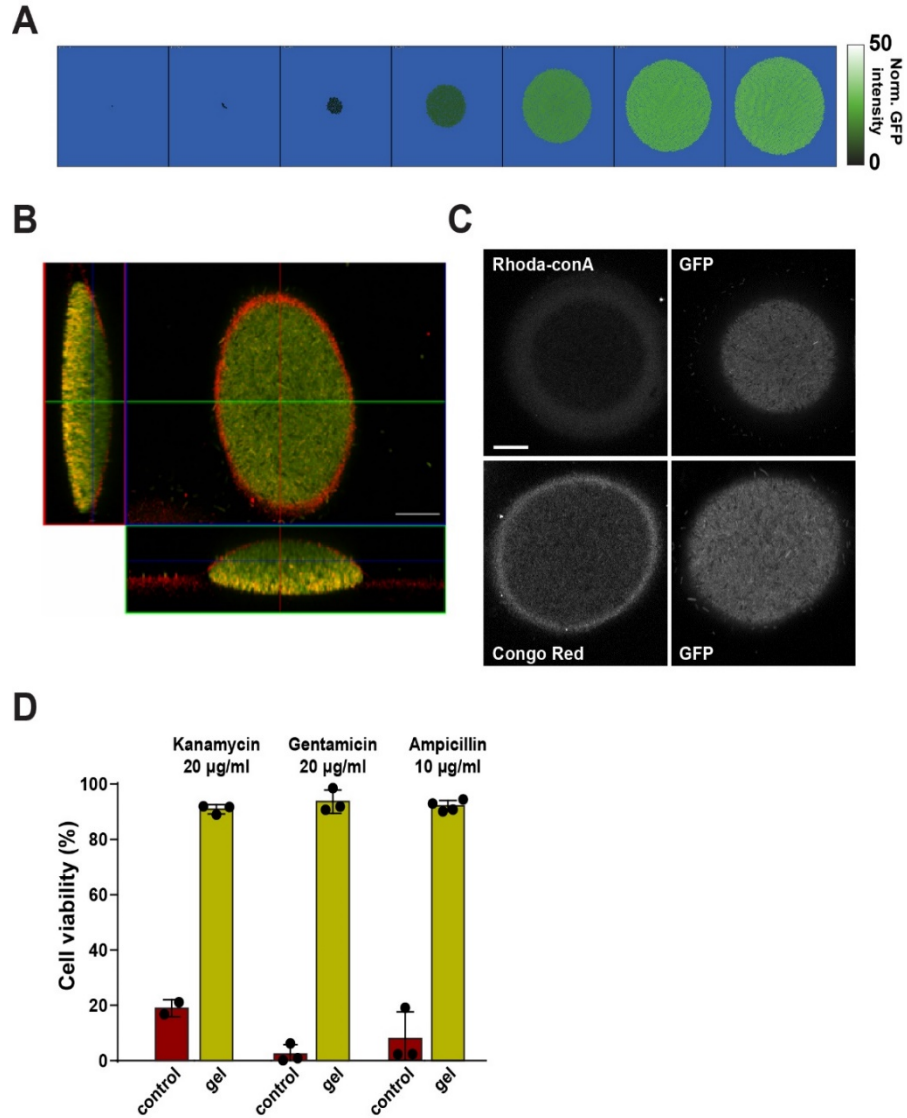


**Figure 4.9: Biofilm growth in environment with mechanical resistance.** **A**, Filmstrip of a simulated colony growing in hydrogel. The green color scale encodes the level of stress response. **B**, Different cross-sections of a colony grown under conditions similar to those shown in Fig. 4b and stained for EPS using rhodamine-labeled concanavalin A. The colony was grown close to the wall of the Petri Dish containing the gel, thus making it asymmetric, and increasing the effective stiffness of the gel on one side of colony. This side displays a more intense EPS staining both at the periphery and inside the colony. Scale bar, 20 µm. **C**, Spatial distributions of stress-reporting GFP and biofilm-like cell-surface structures in *E. coli* (JM105) colonies grown in 1% PuraMatrix hydrogel. CLSM was used to visualize both the rhodamine-labeled concanavalin A-stained EPS D-(+)-glucose and mannose groups and the Congo Red-stained curli after ~6 hours of growth. Scale bar, 20 µm. **D**, Viability comparison between planktonic and 6 hr. hydrogel cultures after exposure to 20 µg/ml of kanamycin (JM105) (n=2 for control, n=3 for gel), 20 µg/ml of gentamicin (CFT073) (n=3), and 10 µg/ml of ampicillin (CFT073) (n=3 for control, n=4 for gel). Error bars are SD.

Furthermore, if accounting for the putative threshold-like dependence of the biofilm development on the stress response intensity, the model suggested that the biofilm markers would be expressed at the periphery of the colony, after the colony reaches a sufficient size. Given the mutual positive cross-regulation between the local proliferation and stress-induced biofilm formation, the biofilm development was expected to be sudden, in the form of a shell encasing the colony.

We experimentally validated model predictions by embedding JM105 *E. coli* cells which express GFP under *rpoH* promoter control into 1% PuraMatrix peptide hydrogel matrix to monitor the distribution of stress during colony expansion within an isotropic environment. This isotropic environment would allow uniform permeation of nutrients into the colony, while also allowing the colony to experience mechanical resistance to expansion from the very beginning, which might better approximate formation of biofilm-like structures in host epithelial cells. While the bulk material properties of this gel [126-128] are different from those of PDMS [129-131], both materials are expected to exert considerable resistance to deformation and elicit cellular responses. Colonies of different sizes were observed in highly-packed states after ~6 hours of growth following the initial seeding, indicating the ability to maintain cohesiveness within the 3-D environment (Figure 4.9B). As predicted by the model, the *rpoH* expression pattern in the hydrogel colonies revealed by CLSM was relatively uniform, with indistinguishable levels of GFP between the core and periphery of the colony, in contrast to the butterfly-shaped *rpoH* expression pattern observed in the microfluidic culture chambers (Figure 4.9C). This suggests the possible onset of a biological stress response early in the colony development, when the colony size

was still small. Staining for the biofilm markers EPS and Curli with rhodamine-labeled concanavalin A and Congo Red, respectively, in well-formed colonies resulted in detectable and near uniform fluorescence in internal regions of the colonies, indicating both the transition to a biofilm-like state early in colony development that coincide with the stress response, as well as the ability of these stains to penetrate into the colonies (Figure 4.9C). In addition, bright halos of staining at the periphery of the colonies further demonstrated elevated levels of biofilm markers EPS and curli secreted at the periphery, which forms a protective shell around the colony that is in agreement with model predictions.

To test for the functional property of antibiotic tolerance conferred by the formation of a penetration barrier as a result of transition to a biofilm-like state in an isotropic growth setting, JM105 cells grown for 6 hours in a planktonic state as well as in hydrogels were subjected to 20  $\mu\text{g/ml}$  of kanamycin challenge (Figure 4.9D). The colonies grown within hydrogels exhibited a significant increase in viability in comparison to their planktonic counterparts. Furthermore, similar experiments performed with uropathogenic *E. coli* and 20  $\mu\text{g/ml}$  gentamicin or 10  $\mu\text{g/ml}$  ampicillin insult displayed similar significant increases in viability as well compared to the same cells planktonically grown in bulk culture (Figure 4.9D). This experiment provided further evidence that growth under mechanical stress can confer substantial protection against certain. Taken together, the experimental results demonstrate that expression of stress-dependent proteins, caused by mechanical resistance of the environment and occurring throughout the course of colony growth, is just as

effective as a sudden, abrupt stress onset at eliciting peripheral biofilm production and conferring the accompanying antibiotics tolerance.

### **4.3: Discussion**

The mechanical environment is increasingly seen as an important determinant of function in a variety of cell and tissue types [132, 133]. While stresses stemming from the external environment have been implicated in the formation of biofilm-like structures [134], we found that this important defensive strategy of *E. coli* is temporally and spatially correlated with the onset of self-imposed physical stress (evidenced by the emergence of a biochemical stress response) as a result of colony expansion in confining environments. This result strongly suggests that the biofilm development could be a direct consequence of evolving mechanical stresses, a common feature of the complex natural micro-environments. Furthermore, the gradual onset of physical stress in a hydrogel environment made the colony express stress-dependent factors at all stages of growth, priming the colony to react much quicker and with increased sensitivity to environmental changes. The temporal and spatial discrepancy in the distributions of stress and biofilm markers under these conditions, which mimic intracellular milieu, suggests that biofilm formation requires exceeding a threshold of the stress levels, which could depend on colony size, nutrient availability, degree of confinement, and the mechanical properties of the confining environment. Overall, these results suggest that physical confinement of an expanding colony, e.g., within a host cell, and mechanical resistance of the environment to the colony growth can be important factors in triggering the biofilm development.

Our results showed that the stress buildup was spatially correlated with increased cell proliferation, which in turn occurred in the regions of abundant nutrient access. Why would these regions accumulate higher physical and thus biological stress levels? The increasingly dense cell colony could have rapidly rising effective viscosity, suggesting that local mechanical stresses might take progressively longer to relax (this is in contrast to growth in aqueous environment, where the stress relaxation is effectively immediate). Therefore, in regions of high cell proliferation, the rate of the buildup of the cell division-induced mechanical stress can exceed the rate of its relaxation, leading to a progressive increase in the stress levels. Even for a relatively low viscosity ( $\mu$ ) on the order of 1 kPa•s (while  $10^6$  times greater than water, still much lower in comparison to many tightly-packed bacterial communities found in nature [135]), the viscous force per unit area experienced by a bacterial cell with a doubling time ( $\tau$ ) of 25 min would be on the order of  $3\mu/2\tau = 1$  Pa from Stokes' law [136], which is on the high end of physiologically relevant viscous forces [134, 137, 138]. Our findings and previous studies [139-142] suggest that bacteria can respond to changes in the viscous forces by alteration of gene regulation, ultimately leading to EPS expression and biofilm formation, which may further affect the mechanical properties of the cell micro-environment. Hence, the onset and progression of the biofilm formation can be subject to a positive feedback and thus occur in a switch-like manner, provided that the local stress levels exceed a threshold value. This positive feedback, however, can be counter-balanced by a negative feedback between the stress buildup and the rate of colony expansion, due to transition to slower growth phenotypes, and possibly higher cell mortality [125]. The interplay between these feedback interactions and sensitivity of cells in biofilms to other aspects of local environment, such as availability of



nutrients and presence of antibiotics, can potentially lead to diverse and highly adaptive biofilm growth allowing considerable structural complexity.

## **4.4: Experimental methods**

### **4.4.1: Bacterial strains and growth conditions**

*E. coli* strain JM105, with low copy number plasmids (pCS101 origin, ampicillin resistance with GFP<sub>uv</sub> gene, *gfp<sub>uv</sub>*) expressing GFP under the control of the heat shock transcription factor  $\sigma^{32}$  promoter, was used to monitor the upregulation of stress response genes in the bacterial colonies. Unless stated otherwise, antibiotic resistance experiments were performed with CFT073 *E. coli*, an uropathogenic strain involved in murine urinary tract infections. JM105 and CFT073 were generous gifts from the Bentley group (University of Maryland, College Park, MD) and the Donnenberg group (University of Maryland School of Medicine, Baltimore, MD), respectively. *S. cohnii* and *P. aeruginosa* strains were obtained from ATCC.

Prior to all experiments, bacterial cells were inoculated from a single agar plate colony and were grown at 30°C in low salt (4 g/L) LB medium supplemented with antibiotics, where appropriate, overnight. Overnight cultures were diluted 1:100 the next day into fresh medium and grown at 30°C to mid-log phase (0.2- 0.3 OD<sub>600</sub>) before being used for experiments.

### **4.4.2: Device design, fabrication, and operation**

The device consists of two layers: a culturing layer on the bottom and a channel layer on top. The layout of the bottom layer is similar to that of the microfluidic chemostat [58], consisting of an array of 8 parallel flow-through channels, each with a depth of 6  $\mu\text{m}$ , which are continuously perfused with fresh media from the inlets. 6  $\mu\text{m}$  deep chambers reside in between the flow-through channels and are connected to the flow-through channels by 0.65  $\mu\text{m}$  deep capillaries. The dimensions of the chamber used are 200  $\mu\text{m}$  in length and either 50, 100, 150 or 200  $\mu\text{m}$  in width. The top layer consists of an array of channels that run on top of the culture chambers, resulting in the thin, deformable layer of PDMS membrane between the layers that serves as the roof of the culture chamber.

The device was fabricated using multiple-layer soft lithography, with the silicon master molds for each layer fabricated using standard photolithography techniques [58]. PDMS (Sylgard 184, Dow corning, Midland, MI) with 5:1 and 20:1 mixtures of resin and catalyst were used for the top and bottom layer, respectively. The top layer was partially cured before individual devices were cut and holes were bored to create inlet and outlet ports. The top layer pieces were then aligned and bonded to the partially cured bottom layer in the oven to complete the curing process. The final devices were immersed in a 0.01 N HCl solution for 1 hour at 80°C, baked for at least 30 minutes in a 150°C oven to increase hardness and Young's modulus, hermetically sealed to #1.5 microscope cover glasses, and further baked at 80°C overnight.

Prior to all experiments, the device was filled with 1% BSA in PBS solution to prevent attachment of cells to the cover glass. The BSA solution was replaced with LB medium

supplemented with antibiotics, where appropriate, before cells were loaded and flow was driven as described in the previous study [58].

#### **4.4.3: Device calibration and pressure measurement**

For calibration, the chip was perfused with fluorescent dyes in both layers (Alexa Fluor 555 on top and Alexa Fluor 488 on the bottom) and external hydrostatic pressure was systematically modulated from 0 to 3 psi and the corresponding vertical displacements of the PDMS membrane were measured in the cross-sectional view of the chamber captured by confocal microscopy. Displacement measurements of the PDMS membrane were performed with multiple chambers of different sizes for each chip via 3-D reconstruction of confocal image stack. The same calibrated chambers were then used for pressure measurements of bacterial colony growth.

#### **4.4.4: Cell staining**

The following reagents were used in our study: 1) Rhodamine-labeled Concanavalin A (10  $\mu\text{g}/\text{mL}$ ; RL-1002, Vector Laboratories, Burlingame, CA), 2) Congo Red (10  $\mu\text{g}/\text{mL}$ ; C6277, Sigma-Aldrich, St. Louis, MO), 3) Propidium iodide (10  $\mu\text{g}/\text{mL}$ ; P4864, Sigma-Aldrich), and 4) SYTO 9 Green fluorescent nucleic acid stain (S-34854, Thermo Fisher Scientific, Waltham, MA). Prior to each staining procedure, LB medium was removed from the device with a PBS wash. The appropriate staining solution was added and allowed to perfuse the device for 30 minutes in the dark, followed by another PBS wash prior to imaging. For staining of samples in hydrogel matrices, existing media was removed and 4% paraformaldehyde fixative was added for 20 minutes prior to the staining.

#### 4.4.5: Microscopy and data analysis

Epi-fluorescence and phase contrast images were captured with a 40x/0.75 Plan-fluor dry objective and a monochrome Cascade 1K digital camera (Photometrics, Tucson, AZ) on a Nikon Eclipse TE2000 inverted microscope equipped with a computer-controlled motorized stage. Colonies in the selected chambers were imaged every 10 to 15 minutes using Slidebook (3I, Denver, CO). To capture 3-D time lapse images of microcolony growth, confocal laser scanning microscopy was performed with a 40x/1.3 Plan-Neo oil objective on a Zeiss LSM 510 Meta confocal microscope. A fast scan was performed to determine the top and bottom of the microchambers prior to performing a full resolution scan. Projected 3-D images and vertical cross-sections were generated with the LSM image browser software. The excitation/emission wavelengths were 395-425/510 nm for GFP<sub>uv</sub>, 485/498 nm for SYTO9, 535/617 nm for propidium iodide, 633/650 nm for Congo Red, and 514/625 nm for rhodamine-labeled concanavalin A.

The dynamics of the stress response onset was calculated by taking the average of the *rpoH*-GFP expression mediated fluorescence intensity data within the region of interest, and normalizing it to the initial time point. In the analysis of the epi-fluorescence data, the results were also normalized to the volume of the cell-filled deformed chamber. To perform this normalization, we confirmed that the elastic plate theory can be used for the membrane deformation analysis, as described below. We used the 3D volume reconstruction (Supplementary Fig. 6) from confocal imaging to validate the following formula:

$$V = V_0 + \int_0^{z_{max}} \int_0^b \int_0^a z(x, y) dx dy dz \quad (12)$$

$$z(x, y) = \frac{z_{max}}{4} \left(1 - \cos \frac{2\pi x}{a}\right) \left(1 - \cos \frac{2\pi y}{b}\right) \quad (13)$$

These formulas represent the first approximation for the deflection of a rectangular plate of length  $a$  and width  $b$  with all sides fixed [143]. The values of  $x$  and  $y$  here represent the coordinates corresponding to the length and width dimensions respectively, while the coordinate  $z$  is orthogonal to  $x$  and  $y$  and oriented in the direction of the deflection. This deflection adds an additional volume to the initial volume  $V_0$ , resulting in the estimate that can be obtained from the measurement of  $z_{max}$ . The same theory also predicts that the displacement of the  $z$  coordinate itself is linearly dependent on the applied pressure, as follows [102]

$$z_{max} = \alpha \frac{p a^2 b^2}{E t^3}, \quad (14)$$

where  $t$  is the membrane thickness,  $a$  and  $b$  are as defined above, and  $E$  is the modulus of elasticity. For a given membrane the coefficient  $\alpha$  is an empirically determined value that depends on aspect geometry, mechanical properties of the material and edge constraint.

To address the question of theoretically predicted pressure distribution within the chamber, we used the formula above as well as performed simulations (in ANSYS 10.0 simulation environment), for the following experimental conditions:  $t=20 \mu\text{m}$ ,  $a=150 \mu\text{m}$  and  $b=160$

$\mu\text{m}$ ;  $E=0.35\text{MPa}$  [129] (data from one of the experimental chamber geometries, see an example in Supplementary Fig. 2). These results were consistent with the calibration data in Supplementary Fig. 1 and the simulations using the same theory as implemented in ANSYS for different chamber widths. We independently determined the change of the deflection for various chambers as a function of time of the bacterial colony expansions (Supplementary Fig. 4). The result was fully consistent with the observations of the calibration experiments (Supp. Fig. 1c) This allowed us to estimate the added volume as a function of time, using it to normalize the epi-fluorescence measurements with the *rpoH* stress reporter. As indicated above, we validated the results by comparison at selected time points to the 3D reconstruction from confocal imaging, see an example below in Supp. Fig. 6.

We also noted that, due to a quick equilibration of *rpoH* expression, on a time scale that is much faster than the experimental time scale (see Fig. 1 also illustrated in a more convenient fashion in Supp. Fig. 5), we can assume that the concentration of the corresponding sigma quickly reaches a steady state, as described by:

$$\frac{dc}{dt} = f - k_d c = 0, \quad (15)$$

where  $f$  is the rate of production,  $c$  is the concentration of the sigma factor and  $k_d$  is the rate of dilution due to continuous cell division, yielding the rate of change of 0. Thus, it is the

concentration  $c$  rather than its rate of change that is directly related to the production function  $f$ :

$$c = \frac{f}{k_d} \quad (16)$$

Therefore, we assumed that, due to the continued rapid cell division following the initiation of chamber deformation, the analysis of the GFP fluorescence intensity levels (rather than the time derivative of this intensity) is adequate for representing the dynamics of *rpoH* expression. Stained areas are calculated by dividing the number of pixels that have intensities higher than a threshold intensity determined by Otsu's method, and dividing it by the total number of pixels within the region of interest.

#### **4.4.6: Preparation of hydrogel matrices**

To prepare the hydrogel-grown colonies, overnight LB cultures were diluted 1:100 and grown to mid-log phase as before. Cells were collected by low speed centrifugation and washed twice with sterile 0.85% NaCl solution. The cells were mixed with 1% PuraMatrix Peptide Hydrogel (Corning Life Sciences, Teterboro, NJ) that has been sonicated for 30 minutes to reduce the viscosity. Addition of medium induces changes in salt concentrations necessary for rapid gelation to occur, thereby encapsulating the cells within the hydrogel. Under physiological conditions, PuraMatrix Peptide Hydrogel forms a transparent hydrogel with an average pore size of 50-200 nm. The LB medium was changed 5 minutes after gelation occurred to equilibrate the pH, and every 3 hours thereafter.

## 4.5: Computational methods

### 4.5.1: Agent-based model

The agent-based simulation, performed using NetLogo [144], models the individual cells as discrete entities, within a two-dimensional grid, and simulates their behavior under non-uniform nutrient conditions, and within an anisotropically-compliant roofed chamber. Collective behavior emerges from the interaction between individual cells, which are governed by a set of rules. Cells were modeled as circles with a diameter of  $D = 1$ , and the chamber dimensions were set relative to the cell diameter, with  $H_x$  (chamber length) =  $140D$ , and  $H_y$  (chamber width) =  $70D$ . Since the model cells are circular instead of rod-shaped, the dimensions of the chamber in the simulation were set such that a similar aspect ratio as well as cell number were maintained as compared to the experiment. The perimeter of the chamber is defined by a separate set of agents, which prevent the movement of cells beyond the confines of the chamber. Any movement, such as the expansion of the colony due to growth, that result in an overlap between a cell and a wall agent will result in a change in the heading of the cell such that it will face away from the wall. The same mechanism also prevents the overlapping of cells with other cells, which can occur if the cell occupancy exceeds the cell capacity for the given location, by aggregating the relative headings of all the overlapping cells and assigning new headings which minimize overlapping, thereby allowing the colony to expand to fill the chamber prior to its full occupancy. Once 99.95% of the simulated chamber area is occupied with cells as a result of the population growth and expansion within the chamber, a buildup of pressure occurs, which is proportional to the average occupancy of the chamber (total number of cells / area) normalized to the basal capacity. The increase in pressure results in the simulated



deformation of the membrane, which is mimicked by an increase in the cell capacity of a given space where a cell resides. The extent of membrane deformation is proportional to the pressure in the chamber, and is approximated by increasing the capacity for cell occupancy at each point in the chamber according to the profile defined by equation 2, as dictated by the plate-theory model [102] (see the validation of the discussion of validation of the model above). Negative differences in capacity and occupancy, as well as the amount of overlap with neighboring cells, lead to the mutual repulsion of inherently non-motile cells, resulting in bulk movement of growing cells toward the interior of the chamber as the roof is progressively deformed.

The model achieves non-uniform growth rate by maintaining a constant nutrient level of 10 at two opposing edges of the chamber, allowing a gradient of nutrients to form as a result of diffusion and cellular consumption. Diffusion is modeled as an equal distribution of nutrient shared to the neighboring regions, whereas maximal consumption rate is set to 0.008. The nutrient consumption rate of individual cells is attenuated by increases in the pressure, and is also proportional to the local level of nutrients relative to the source. Nutrient consumption results in an equal loss of nutrient in the local space. Cellular division occurs when a pre-defined level of nutrient (15) has been consumed. When a cell divides, a new cell is generated and the nutrient level needed for division for each cell is reset to half of the original cell, with a 5% variation added for randomness. Therefore, a gradient of growth rates emerges from the nutrient gradient within the chamber, with higher rates of growth closer to the source of nutrients due to faster consumption, and therefore, a faster rate of reaching the threshold necessary for cell division. Stress, indicated by GFP

production and accumulation, is assumed to positively correlate with the pressure, as well as nutrient consumption rate when pressure is positive. Cellular escape at the two sides of the chamber was modeled with a Monte Carlo simulation. The final stress profile was obtained by integrating the stress in the z-direction within a defined radius of the cell to enable smoothing. Each time step in the simulation of the model includes simulation of the diffusion of nutrients, cell capacity change and pressure change of the environment, followed by the simulation of the consumption of nutrients, division of cells, movement as a result of overlap, and stress profile for each individual cell. Cellular escape from the chamber is simulated at the end.

The hydrogel model is essentially identical to the model above, following the same rules, but with a few key differences. There is no preset boundary which physically limits the expansion of the colony like in the case of chamber growth. Without a boundary, the expansion of the colony depends only on its ability to consume nutrients and divide. The growth remains negatively affected by a buildup of pressure, but pressure experienced by colony as a result of expansion within the isotropic hydrogel matrix is now modeled as a compressed spring using Hooke's law. The pressure is set to be proportional to a factor representing the stiffness of the hydrogel material (0.2), as well as the difference between the colony radius at time =  $t$  and the colony radius at time = 0, which, in this case, was the radius of a single cell (0.5D).

#### **4.5.1: Mean field model**

The *mean field simulation* assumes that the chamber is filled with a viscous fluid that undergoes creep flow. The non-uniform growth rate is modeled by a gradient of rates at which fluid enters the chamber from the bottom, so that there is maximum growth at the sides and less growth at the center. The membrane deformation is mimicked by an equivalent pressure-release profile on the top of the chamber. Stress is assumed to be directly proportional to the growth rate (i.e., the creep rate). The final stress profile (Fig. 2c) was obtained by integrating the stress in the z-direction, which shows good agreement with the measured GFP and EPS expression profiles. The simulation was performed using the COMSOL laminar flow module, which uses by default the compressible-flow formulation of the Navier-Stokes equations. The fluid density was set to  $10^3 \text{ kg/m}^3$ , and the viscosity to  $10^5 \text{ Pa}\cdot\text{s}$ . The dimensions of the chamber used in the simulation were  $H_x$  (chamber length) =  $200 \text{ }\mu\text{m}$ ,  $H_y$  (chamber width) =  $100 \text{ }\mu\text{m}$ , and  $H_z$  (chamber height) =  $6 \text{ }\mu\text{m}$ . The walls had no-slip boundary conditions. The bottom surface of the chamber was set as an inlet with a normal inflow velocity proportional to

$$v = 1.5 + \cos \frac{2\pi x}{H_x}, \quad (17)$$

to establish the gradient mimicking growth rate. The top surface of the chamber was set as an outlet with an exit pressure proportional to equation 2 to mimic fluid flow due to membrane deformation. To calculate the stress, the magnitude of the flow velocity was integrated in the vertical (z) direction.

# Chapter 5: General conclusions

## 5.1: Summary of results

This dissertation has examined multiple ways in which bacterial collective cell behavior can depend on the environmental conditions. By using engineering approaches, in the form of novel microfluidic technologies, we were able to create complex but tightly controlled microenvironments for the cells to reside in, allowing us to precisely perturb and study the interactions between the environmental conditions and the collective behavior that arise from bacteria consortia. We applied these devices first to study the effects of the environment on the coordination of collective cell behavior by QS (Chapter 2). In particular, we found that auto and exogenous inductions of the QS response within the confines of the various chamber configurations both resulted in similar biphasic distributions of response intensities with respect to growth rate, demonstrating that modulation of QS response is dependent on mass transport of factors other than the signaling molecule, inconsistent with classical density- or diffusion-based interpretations of QS. In addition, we found that contrary to the commonly presumed switch-like behavior characteristic of systems with positive feedback, QS displays dynamically complex responses within different environments. Using direct measurements and mathematical modeling, we demonstrate that this environmental dependence can be accounted for by the growth-mediated differential balance between synthesis and dilution of QS proteins. This mechanism can explain changes in QS dynamics that occur as a result of variations in nutrient composition and access, temperature, and direct changes to the synthesis of a QS protein. This allowed the use of different components of QS dynamics as metrics for

discerning the various aspects of the environment, such as global, external variables like the composition, or the local properties such as differences in mass transfer characteristics.

In Chapter 3, this mechanism of balance between QS protein synthesis and dilution can be extended to explain spatial response gradients stemming from local nutrient and growth differences, as demonstrated by the congruence between spatial dynamics and mean response dynamics. This suggested that the onset of QS is spatially localized, with certain cells predisposed with higher propensity for the initiation of the QS response, which is dependent on the local environmental conditions. In addition to spatial control, QS onset also demonstrate tight temporal control, as exhibited in the wide range of environment-dependent onset times. Lengthy onset times revealed the existence of temporal thresholds, which required a persistent stimulation to induce onset, as well as bistable response properties, which can filter out transient or weak stimuli and enhance the robustness of the system by preventing or sustaining an induction event in the face of perturbations. The temporal threshold can be lowered by cell-cell communication stemming from an induced subpopulation that arose from bistability, effectively combining the bet-hedging response diversification strategy with cell signaling to enhance overall population fitness when environments change. These results reveal that QS can display spatially and temporally complex dynamic behavior by incorporating environmental information into one of the most ancient cell communication networks.

In Chapter 4, we use a different version of our developed device to study the direct effects of environmental cues on collective cell behavior. By using new controlled methods

allowing high-throughput and reproducible biofilm growth, we show that biofilm formation is linked to self-imposed mechanical stress. In growing uropathogenic *E. coli* colonies, we report that mechanical stress can initially emerge from the physical stress accompanying colony confinement within micro-cavities or hydrogel environments reminiscent of the cytosol of host cells. Biofilm formation can then be enhanced by a nutrient access-modulated feedback loop, in which biofilm matrix deposition can be particularly high in areas of increased mechanical and biological stress, with the deposited matrix further enhancing the stress levels. This feedback regulation can lead to adaptive and diverse biofilm formation guided by the environmental stresses. Our results suggest previously unappreciated mechanisms of the onset and progression of biofilm growth.

## **5.2 Future directions and concluding thoughts**

This dissertation provided insights into how the effects of the environment on collective cell behavior can be studied with engineered devices which can precisely control the type and amount of stimulation experienced by the cells. Within the context of how the environment can modulate the QS response, many interesting questions are still left unanswered. While the mechanism of the control of QS has been presented as a generalized process of balance of synthesis and dilution QS proteins that is applicable to many environmental conditions, it is not known how the cell can integrate all of the factors of the environment to determine the growth rate. This dependence simplifies the QS dependence on the environment, which can be represented as a decision-making step that relies on the information from directly detected QS signals, but also the preprocessed information about the environment in the form of modulations to the rates of cellular

process. Thus, the direct cues from the environment is not part of the QS decision-making process, but is part of some upstream, higher-order process fundamental to the cell's regulation mechanisms. However, microfluidics can provide a perfect platform for studies relating to the environment, and in particular, studies related to the dependence on nutrients. Unraveling the mysteries of nutrient dependence might explain why tryptone and casamino acids, which are both digestions of casein, but to different degrees, results in such a huge difference in synthesis and dilution (growth) rates that ultimately translate into vastly different QS dynamics. A better understanding of the dependence on different kinds of nutrients, as well as amount, would lead to a better understanding of the sensitivities of the QS response to environmental conditions.

In addition, the QS response dependence analyzed here was performed on the most canonical and well understood pathway in a somewhat isolated scenario, i.e. the circuit was derived from *V. fischeri* and placed into *E. coli*, where its own signaling processes do not interfere with that of the circuit under examination. However, within natural QS circuits, they often do not exist on their own, and are often much more complex in architecture. QS circuits exist in many different species with many different architectures, in which some can exist in series with one coupled to another, or multiple signals can converge into the same downstream regulation pathway, adding redundancy to the response. The environmental dependence might be less emphasized within such scenarios, or might have different modulating effects. It would be interesting to apply the platform and framework developed within this work to study the environmental dependence of other QS circuits and responses.

One particularly noteworthy phenomenon that is worth further exploration is the heterogeneity of the QS response that we observed particularly at the onset as well as within certain conditions in which the population is separated into subsets of induced and uninduced cells. While the emergence of heterogeneity might be due to stochasticity in gene expression in conjunction with different local environments, we observed that induced cells appear to produce progeny that remain induced, resulting in a lineage dependence that can be tracked across multiple generations. This could be due to the fact that the basis of the QS response is the constituent proteins, which are distributed to the progeny as the cells divide. This could lead to questions with regards to the stability and robustness of such lineage dependence and how long and across how many generations such memory can persist. Such studies are tailor-made for microfluidic devices due to the ability to culture cells chemostatically within monolayers indefinitely as long as media is supplied continuously. The ability to visualize individual cells within a monolayer would allow for automated software to perform segmentation and lineage tracking in a high-throughput manner. The results of analyzing the lineage dependence could be juxtaposed against the dependence on the local environmental condition within this work to further our understanding of the QS response. With lineage tracking, we can also test the hypothesis that the induction of QS response constitutes a significant investment of resources by the cells that divert energy from cellular growth and division, thus resulting in reduced growth rate that positively reinforces the QS response. This positive feedback can stabilize the response induction and provide an additional layer of robustness against perturbations that could potentially disrupt the response. In addition, a common theme



throughout this dissertation has been the spatial dependence of responses, which no doubt arose from the defined geometry of the chambers in which the cells are grown. This will be an important factor to consider when attributing the effects to either spatial or lineage dependence.

This dissertation presented just a small number of examples of how microfluidic devices can be a valuable tool in the study of the interactions between the environment and bacterial colonies. We believe that as we continue to appreciate the importance of bacterial communities in relation to human health, the scientific community will benefit from and therefore embrace more of the interdisciplinary approaches such as those presented here to help unravel the complex interconnected networks that govern microbial consortia behaviors.

## Bibliography:

1. Dunny, G.M., T.J. Brickman, and M. Dworkin, *Multicellular behavior in bacteria: communication, cooperation, competition and cheating*. Bioessays, 2008. **30**(4): p. 296-8.
2. Engelberg-Kulka, H., et al., *Bacterial programmed cell death and multicellular behavior in bacteria*. PLoS Genet, 2006. **2**(10): p. e135.
3. Hooshangi, S. and W.E. Bentley, *From unicellular properties to multicellular behavior: bacteria quorum sensing circuitry and applications*. Curr Opin Biotechnol, 2008. **19**(6): p. 550-5.
4. Stubbendieck, R.M., C. Vargas-Bautista, and P.D. Straight, *Bacterial Communities: Interactions to Scale*. Front Microbiol, 2016. **7**: p. 1234.
5. Gilbert, J.A., et al., *Current understanding of the human microbiome*. Nat Med, 2018. **24**(4): p. 392-400.
6. Knight, R., et al., *The Microbiome and Human Biology*. Annu Rev Genomics Hum Genet, 2017. **18**: p. 65-86.
7. Thompson, J.A., et al., *Manipulation of the quorum sensing signal AI-2 affects the antibiotic-treated gut microbiota*. Cell Rep, 2015. **10**(11): p. 1861-71.
8. Bivar Xavier, K., *Bacterial interspecies quorum sensing in the mammalian gut microbiota*. C R Biol, 2018. **341**(5): p. 297-299.
9. Schroeder, B.O. and F. Backhed, *Signals from the gut microbiota to distant organs in physiology and disease*. Nat Med, 2016. **22**(10): p. 1079-1089.
10. Federle, M.J. and B.L. Bassler, *Interspecies communication in bacteria*. J Clin Invest, 2003. **112**(9): p. 1291-9.
11. Shapiro, J.A., *Thinking about bacterial populations as multicellular organisms*. Annu Rev Microbiol, 1998. **52**: p. 81-104.
12. Miller, M.B. and B.L. Bassler, *Quorum sensing in bacteria*. Annu Rev Microbiol, 2001. **55**: p. 165-99.
13. Waters, C.M. and B.L. Bassler, *Quorum sensing: cell-to-cell communication in bacteria*. Annu Rev Cell Dev Biol, 2005. **21**: p. 319-46.
14. Ng, W.L. and B.L. Bassler, *Bacterial quorum-sensing network architectures*. Annu Rev Genet, 2009. **43**: p. 197-222.
15. Haseltine, E.L. and F.H. Arnold, *Implications of rewiring bacterial quorum sensing*. Appl Environ Microbiol, 2008. **74**(2): p. 437-45.
16. Swift, S., et al., *Quorum sensing as a population-density-dependent determinant of bacterial physiology*. Adv Microb Physiol, 2001. **45**: p. 199-270.
17. Swift, S., et al., *Quorum sensing: a population-density component in the determination of bacterial phenotype*. Trends Biochem Sci, 1996. **21**(6): p. 214-9.
18. Fuqua, W.C., S.C. Winans, and E.P. Greenberg, *Quorum sensing in bacteria: the LuxR-LuxI family of cell density-responsive transcriptional regulators*. J Bacteriol, 1994. **176**(2): p. 269-75.
19. Perchat, S., et al., *How Quorum Sensing Connects Sporulation to Necrotrophism in Bacillus thuringiensis*. PLoS Pathog, 2016. **12**(8): p. e1005779.

20. Steiner, E., et al., *An agr quorum sensing system that regulates granulose formation and sporulation in Clostridium acetobutylicum*. Appl Environ Microbiol, 2012. **78**(4): p. 1113-22.
21. Antunes, L.C., et al., *Quorum sensing in bacterial virulence*. Microbiology, 2010. **156**(Pt 8): p. 2271-82.
22. Rumbaugh, K.P., et al., *Kin selection, quorum sensing and virulence in pathogenic bacteria*. Proc Biol Sci, 2012. **279**(1742): p. 3584-8.
23. Zheng, J., et al., *Quorum sensing and a global regulator TsrA control expression of type VI secretion and virulence in Vibrio cholerae*. Proc Natl Acad Sci U S A, 2010. **107**(49): p. 21128-33.
24. Bodelon, G., et al., *Detection and imaging of quorum sensing in Pseudomonas aeruginosa biofilm communities by surface-enhanced resonance Raman scattering*. Nat Mater, 2016. **15**(11): p. 1203-1211.
25. Kim, M.K., et al., *Surface-attached molecules control Staphylococcus aureus quorum sensing and biofilm development*. Nat Microbiol, 2017. **2**: p. 17080.
26. Parsek, M.R. and E.P. Greenberg, *Sociomicrobiology: the connections between quorum sensing and biofilms*. Trends Microbiol, 2005. **13**(1): p. 27-33.
27. Miyashiro, T. and E.G. Ruby, *Shedding light on bioluminescence regulation in Vibrio fischeri*. Mol Microbiol, 2012. **84**(5): p. 795-806.
28. Shadel, G.S. and T.O. Baldwin, *The Vibrio fischeri LuxR protein is capable of bidirectional stimulation of transcription and both positive and negative regulation of the luxR gene*. J Bacteriol, 1991. **173**(2): p. 568-74.
29. Shadel, G.S. and T.O. Baldwin, *Positive autoregulation of the Vibrio fischeri luxR gene. LuxR and autoinducer activate cAMP-catabolite gene activator protein complex-independent and -dependent luxR transcription*. J Biol Chem, 1992. **267**(11): p. 7696-702.
30. Stevens, A.M., K.M. Dolan, and E.P. Greenberg, *Synergistic binding of the Vibrio fischeri LuxR transcriptional activator domain and RNA polymerase to the lux promoter region*. Proc Natl Acad Sci U S A, 1994. **91**(26): p. 12619-23.
31. Waters, C.M. and B.L. Bassler, *The Vibrio harveyi quorum-sensing system uses shared regulatory components to discriminate between multiple autoinducers*. Genes Dev, 2006. **20**(19): p. 2754-67.
32. Henke, J.M. and B.L. Bassler, *Three parallel quorum-sensing systems regulate gene expression in Vibrio harveyi*. J Bacteriol, 2004. **186**(20): p. 6902-14.
33. Le, K.Y. and M. Otto, *Quorum-sensing regulation in staphylococci-an overview*. Front Microbiol, 2015. **6**: p. 1174.
34. Yarwood, J.M. and P.M. Schlievert, *Quorum sensing in Staphylococcus infections*. J Clin Invest, 2003. **112**(11): p. 1620-5.
35. Boedicker, J.Q., M.E. Vincent, and R.F. Ismagilov, *Microfluidic confinement of single cells of bacteria in small volumes initiates high-density behavior of quorum sensing and growth and reveals its variability*. Angew Chem Int Ed Engl, 2009. **48**(32): p. 5908-11.
36. Timp, W., et al., *Jamming prokaryotic cell-to-cell communications in a model biofilm*. Lab Chip, 2009. **9**(7): p. 925-34.
37. Redfield, R.J., *Is quorum sensing a side effect of diffusion sensing?* Trends Microbiol, 2002. **10**(8): p. 365-70.

38. Hense, B.A., et al., *Does efficiency sensing unify diffusion and quorum sensing?* Nat Rev Microbiol, 2007. **5**(3): p. 230-9.
39. Fong, J.N.C. and F.H. Yildiz, *Biofilm Matrix Proteins*. Microbiol Spectr, 2015. **3**(2).
40. Wei, Q. and L.Z. Ma, *Biofilm matrix and its regulation in Pseudomonas aeruginosa*. Int J Mol Sci, 2013. **14**(10): p. 20983-1005.
41. Flemming, H.C., T.R. Neu, and D.J. Wozniak, *The EPS matrix: the "house of biofilm cells"*. J Bacteriol, 2007. **189**(22): p. 7945-7.
42. Flemming, H.C. and J. Wingender, *The biofilm matrix*. Nat Rev Microbiol, 2010. **8**(9): p. 623-33.
43. Zijngel, V., et al., *Oral biofilm architecture on natural teeth*. PLoS One, 2010. **5**(2): p. e9321.
44. Buhmann, M.T., et al., *In Vitro Biofilm Models for Device-Related Infections*. Trends Biotechnol, 2016. **34**(12): p. 945-948.
45. Koseoglu, H., et al., *Ultrastructural stages of biofilm development of Escherichia coli on urethral catheters and effects of antibiotics on biofilm formation*. Urology, 2006. **68**(5): p. 942-6.
46. Neu, T.R. and J.R. Lawrence, *Advanced techniques for in situ analysis of the biofilm matrix (structure, composition, dynamics) by means of laser scanning microscopy*. Methods Mol Biol, 2014. **1147**: p. 43-64.
47. O'Toole, G., H.B. Kaplan, and R. Kolter, *Biofilm formation as microbial development*. Annu Rev Microbiol, 2000. **54**: p. 49-79.
48. Stoodley, P., et al., *Biofilms as complex differentiated communities*. Annu Rev Microbiol, 2002. **56**: p. 187-209.
49. Burmolle, M., et al., *Interactions in multispecies biofilms: do they actually matter?* Trends Microbiol, 2014. **22**(2): p. 84-91.
50. Foster, K.R. and T. Bell, *Competition, not cooperation, dominates interactions among culturable microbial species*. Curr Biol, 2012. **22**(19): p. 1845-50.
51. Kalmokoff, M.L., et al., *Adsorption, attachment and biofilm formation among isolates of Listeria monocytogenes using model conditions*. J Appl Microbiol, 2001. **91**(4): p. 725-34.
52. Cheng, J., et al., *Adsorption properties and gaseous mercury transformation rate of natural biofilm*. Bull Environ Contam Toxicol, 2008. **81**(5): p. 516-20.
53. Romani, A.M. and S. Sabater, *Influence of algal biomass on extracellular enzyme activity in river biofilms*. Microb Ecol, 2000. **40**(1): p. 16-24.
54. Conlon, B.P., S.E. Rowe, and K. Lewis, *Persister cells in biofilm associated infections*. Adv Exp Med Biol, 2015. **831**: p. 1-9.
55. Khan, W., et al., *Aminoglycoside resistance of Pseudomonas aeruginosa biofilms modulated by extracellular polysaccharide*. Int Microbiol, 2010. **13**(4): p. 207-12.
56. Mok, J., et al., *Digital microfluidic assay for protein detection*. Proc Natl Acad Sci U S A, 2014. **111**(6): p. 2110-5.
57. Ahrberg, C.D., A. Manz, and B.G. Chung, *Polymerase chain reaction in microfluidic devices*. Lab Chip, 2016. **16**(20): p. 3866-3884.
58. Groisman, A., et al., *A microfluidic chemostat for experiments with bacterial and yeast cells*. Nat Methods, 2005. **2**(9): p. 685-9.

59. Cho, H., et al., *Self-organization in high-density bacterial colonies: efficient crowd control*. PLoS Biol, 2007. **5**(11): p. e302.
60. Park, J.W., et al., *Microfluidic culture platform for neuroscience research*. Nat Protoc, 2006. **1**(4): p. 2128-36.
61. Beebe, D.J., G.A. Mensing, and G.M. Walker, *Physics and applications of microfluidics in biology*. Annu Rev Biomed Eng, 2002. **4**: p. 261-86.
62. Breslauer, D.N., P.J. Lee, and L.P. Lee, *Microfluidics-based systems biology*. Mol Biosyst, 2006. **2**(2): p. 97-112.
63. VanDersarl, J.J., A.M. Xu, and N.A. Melosh, *Rapid spatial and temporal controlled signal delivery over large cell culture areas*. Lab Chip, 2011. **11**(18): p. 3057-63.
64. van Duinen, V., et al., *Microfluidic 3D cell culture: from tools to tissue models*. Curr Opin Biotechnol, 2015. **35**: p. 118-26.
65. Zahavi, E.E., et al., *A compartmentalized microfluidic neuromuscular co-culture system reveals spatial aspects of GDNF functions*. J Cell Sci, 2015. **128**(6): p. 1241-52.
66. Zhang, M.Y., et al., *Microfluidic environment for high density hepatocyte culture*. Biomed Microdevices, 2008. **10**(1): p. 117-21.
67. Kimura, H., et al., *An integrated microfluidic system for long-term perfusion culture and on-line monitoring of intestinal tissue models*. Lab Chip, 2008. **8**(5): p. 741-6.
68. Ong, S.M., et al., *A gel-free 3D microfluidic cell culture system*. Biomaterials, 2008. **29**(22): p. 3237-44.
69. Wang, P., et al., *Robust growth of Escherichia coli*. Curr Biol, 2010. **20**(12): p. 1099-103.
70. Anetzberger, C., T. Pirch, and K. Jung, *Heterogeneity in quorum sensing-regulated bioluminescence of Vibrio harveyi*. Mol Microbiol, 2009. **73**(2): p. 267-77.
71. Kalia, V.C. and H.J. Purohit, *Quenching the quorum sensing system: potential antibacterial drug targets*. Crit Rev Microbiol, 2011. **37**(2): p. 121-40.
72. Perez, P.D. and S.J. Hagen, *Heterogeneous response to a quorum-sensing signal in the luminescence of individual Vibrio fischeri*. PLoS One, 2010. **5**(11): p. e15473.
73. Williams, J.W., et al., *Robust and sensitive control of a quorum-sensing circuit by two interlocked feedback loops*. Mol Syst Biol, 2008. **4**: p. 234.
74. Connell, J.L., et al., *Probing prokaryotic social behaviors with bacterial "lobster traps"*. MBio, 2010. **1**(4).
75. Hagen, S.J., et al., *Bacterium in a box: sensing of quorum and environment by the LuxI/LuxR gene regulatory circuit*. J Biol Phys, 2010. **36**(3): p. 317-27.
76. Kim, M.K., et al., *Local and global consequences of flow on bacterial quorum sensing*. Nat Microbiol, 2016. **1**: p. 15005.
77. Park, S., et al., *Influence of topology on bacterial social interaction*. Proc Natl Acad Sci U S A, 2003. **100**(24): p. 13910-5.
78. Gorke, B. and J. Stulke, *Carbon catabolite repression in bacteria: many ways to make the most out of nutrients*. Nat Rev Microbiol, 2008. **6**(8): p. 613-24.
79. You, C., et al., *Coordination of bacterial proteome with metabolism by cyclic AMP signalling*. Nature, 2013. **500**(7462): p. 301-6.

80. Stewart, P.S. and M.J. Franklin, *Physiological heterogeneity in biofilms*. Nat Rev Microbiol, 2008. **6**(3): p. 199-210.
81. Miller, W.G., J.H. Leveau, and S.E. Lindow, *Improved *gfp* and *inaZ* broad-host-range promoter-probe vectors*. Mol Plant Microbe Interact, 2000. **13**(11): p. 1243-50.
82. Klumpp, S., Z. Zhang, and T. Hwa, *Growth rate-dependent global effects on gene expression in bacteria*. Cell, 2009. **139**(7): p. 1366-75.
83. Melke, P., et al., *A cell-based model for quorum sensing in heterogeneous bacterial colonies*. PLoS Comput Biol, 2010. **6**(6): p. e1000819.
84. Goryachev, A.B., D.J. Toh, and T. Lee, *Systems analysis of a quorum sensing network: design constraints imposed by the functional requirements, network topology and kinetic constants*. Biosystems, 2006. **83**(2-3): p. 178-87.
85. Cheong, R., et al., *Information transduction capacity of noisy biochemical signaling networks*. Science, 2011. **334**(6054): p. 354-8.
86. Rhee, A., R. Cheong, and A. Levchenko, *The application of information theory to biochemical signaling systems*. Phys Biol, 2012. **9**(4): p. 045011.
87. Dertinger, S.K.W., et al., *Generation of Gradients Having Complex Shapes Using Microfluidic Networks*. Analytical Chemistry, 2001. **73**(6): p. 1240-1246.
88. Elowitz, M.B., et al., *Stochastic gene expression in a single cell*. Science, 2002. **297**(5584): p. 1183-6.
89. Park, S., et al., *Motion to form a quorum*. Science, 2003. **301**(5630): p. 188.
90. Anderson, G.G., et al., *Intracellular bacterial communities of uropathogenic Escherichia coli in urinary tract pathogenesis*. Trends Microbiol, 2004. **12**(9): p. 424-30.
91. Anderson, G.G., et al., *Intracellular bacterial biofilm-like pods in urinary tract infections*. Science, 2003. **301**(5629): p. 105-7.
92. Bassler, B.L., *Small talk. Cell-to-cell communication in bacteria*. Cell, 2002. **109**(4): p. 421-4.
93. Hall-Stoodley, L., J.W. Costerton, and P. Stoodley, *Bacterial biofilms: from the natural environment to infectious diseases*. Nat Rev Microbiol, 2004. **2**(2): p. 95-108.
94. Miller, M.B. and B.L. Bassler, *Quorum sensing in bacteria*. Annu Rev Microbiol, 2001. **55**(1): p. 165-99.
95. O'Toole, G., H.B. Kaplan, and R. Kolter, *Biofilm formation as microbial development*. Annu Rev Microbiol, 2000. **54**(1): p. 49-79.
96. Danese, P.N., L.A. Pratt, and R. Kolter, *Exopolysaccharide production is required for development of Escherichia coli K-12 biofilm architecture*. Journal of Bacteriology, 2000. **182**(12): p. 3593-3596.
97. Kikuchi, T., et al., *Curli fibers are required for development of biofilm architecture in Escherichia coli K-12 and enhance bacterial adherence to human uroepithelial cells*. Microbiol Immunol, 2005. **49**(9): p. 875-84.
98. Garcia-Medina, R., et al., *Pseudomonas aeruginosa acquires biofilm-like properties within airway epithelial cells*. Infect Immun, 2005. **73**(12): p. 8298-305.
99. Justice, S.S., et al., *Differentiation and developmental pathways of uropathogenic Escherichia coli in urinary tract pathogenesis*. Proc Natl Acad Sci U S A, 2004. **101**(5): p. 1333-8.

100. Su, P.T., et al., *Bacterial Colony from Two-Dimensional Division to Three-Dimensional Development*. Plos One, 2012. **7**(11).
101. Grant, M.A.A., et al., *The role of mechanical forces in the planar-to-bulk transition in growing Escherichia coli microcolonies*. Journal of the Royal Society Interface, 2014. **11**(97).
102. Roark, R.J., et al., *Roark's formulas for stress and strain*. 8th ed. 2012, New York: McGraw-Hill. xviii, 1054 p.
103. Mohandas, N. and E. Evans, *Mechanical properties of the red cell membrane in relation to molecular structure and genetic defects*. Annu Rev Biophys Biomol Struct, 1994. **23**(1): p. 787-818.
104. Vlahakis, N.E. and R.D. Hubmayr, *Invited review: plasma membrane stress failure in alveolar epithelial cells*. J Appl Physiol (1985), 2000. **89**(6): p. 2490-6;discussion 2497.
105. Kau, A.L., D.A. Hunstad, and S.J. Hultgren, *Interaction of uropathogenic Escherichia coli with host uroepithelium*. Curr Opin Microbiol, 2005. **8**(1): p. 54-9.
106. Mulvey, M.A., J.D. Schilling, and S.J. Hultgren, *Establishment of a persistent Escherichia coli reservoir during the acute phase of a bladder infection*. Infect Immun, 2001. **69**(7): p. 4572-9.
107. Song, J., et al., *TLR4-mediated expulsion of bacteria from infected bladder epithelial cells*. Proc Natl Acad Sci U S A, 2009. **106**(35): p. 14966-71.
108. Arnoldi, M., et al., *Bacterial turgor pressure can be measured by atomic force microscopy*. Phys Rev E Stat Phys Plasmas Fluids Relat Interdiscip Topics, 2000. **62**(1 Pt B): p. 1034-44.
109. Gaillard, J.L., et al., *In vitro model of penetration and intracellular growth of Listeria monocytogenes in the human enterocyte-like cell line Caco-2*. Infect Immun, 1987. **55**(11): p. 2822-9.
110. Cha, H.J., et al., *Green fluorescent protein as a noninvasive stress probe in resting Escherichia coli cells*. Appl Environ Microbiol, 1999. **65**(2): p. 409-14.
111. Whiteley, M., et al., *Gene expression in Pseudomonas aeruginosa biofilms*. Nature, 2001. **413**(6858): p. 860-4.
112. Allison, D.G. and I.W. Sutherland, *A Staining Technique for Attached Bacteria and Its Correlation to Extracellular Carbohydrate Production*. Journal of Microbiological Methods, 1984. **2**(2): p. 93-99.
113. Pawar, D.M., M.L. Rossman, and J. Chen, *Role of curli fimbriae in mediating the cells of enterohaemorrhagic Escherichia coli to attach to abiotic surfaces*. Journal of Applied Microbiology, 2005. **99**(2): p. 418-425.
114. Olsen, A., et al., *Identification of two protein-binding and functional regions of curli, a surface organelle and virulence determinant of Escherichia coli*. Journal of Biological Chemistry, 2002. **277**(37): p. 34568-34572.
115. Beloin, C. and J.M. Ghigo, *Finding gene-expression patterns in bacterial biofilms*. Trends Microbiol, 2005. **13**(1): p. 16-9.
116. Branda, S.S., et al., *Biofilms: the matrix revisited*. Trends Microbiol, 2005. **13**(1): p. 20-6.
117. Ozbudak, E.M., et al., *Multistability in the lactose utilization network of Escherichia coli*. Nature, 2004. **427**(6976): p. 737-40.

118. Davies, D., *Understanding biofilm resistance to antibacterial agents*. Nat Rev Drug Discov, 2003. **2**(2): p. 114-22.
119. Taylor, P.K., A.T. Yeung, and R.E. Hancock, *Antibiotic resistance in Pseudomonas aeruginosa biofilms: towards the development of novel anti-biofilm therapies*. J Biotechnol, 2014. **191**: p. 121-30.
120. Zhang, L. and T.F. Mah, *Involvement of a novel efflux system in biofilm-specific resistance to antibiotics*. J Bacteriol, 2008. **190**(13): p. 4447-52.
121. Whitchurch, C.B., et al., *Extracellular DNA required for bacterial biofilm formation*. Science, 2002. **295**(5559): p. 1487.
122. Brooun, A., S. Liu, and K. Lewis, *A dose-response study of antibiotic resistance in Pseudomonas aeruginosa biofilms*. Antimicrob Agents Chemother, 2000. **44**(3): p. 640-6.
123. Ishida, H., et al., *In vitro and in vivo activities of levofloxacin against biofilm-producing Pseudomonas aeruginosa*. Antimicrob Agents Chemother, 1998. **42**(7): p. 1641-5.
124. Shigeta, M., et al., *Permeation of antimicrobial agents through Pseudomonas aeruginosa biofilms: a simple method*. Chemotherapy, 1997. **43**(5): p. 340-5.
125. Asally, M., et al., *Localized cell death focuses mechanical forces during 3D patterning in a biofilm*. Proc Natl Acad Sci U S A, 2012. **109**(46): p. 18891-6.
126. Yamaoka, H., et al., *Cartilage tissue engineering using human auricular chondrocytes embedded in different hydrogel materials*. J Biomed Mater Res A, 2006. **78**(1): p. 1-11.
127. Shroff, K., et al., *Fibronectin-mimetic peptide-amphiphile nanofiber gels support increased cell adhesion and promote ECM production*. Soft Matter, 2010. **6**(20): p. 5064-5072.
128. Caliari, S.R. and J.A. Burdick, *A practical guide to hydrogels for cell culture*. Nat Methods, 2016. **13**(5): p. 405-14.
129. Armani, D., C. Liu, and N. Aluru, *Re-configurable fluid circuits by PDMS elastomer micromachining*. Mems '99: Twelfth Ieee International Conference on Micro Electro Mechanical Systems, Technical Digest, 1999: p. 222-227.
130. Johnston, I.D., et al., *Mechanical characterization of bulk Sylgard 184 for microfluidics and microengineering*. Journal of Micromechanics and Microengineering, 2014. **24**(3).
131. Mark, J.E., *Polymer data handbook*. 2nd ed. 2009, Oxford ; New York: Oxford University Press. vii, 1250 p.
132. Hoffman, B.D., C. Grashoff, and M.A. Schwartz, *Dynamic molecular processes mediate cellular mechanotransduction*. Nature, 2011. **475**(7356): p. 316-23.
133. Nelson, C.M. and J.P. Gleghorn, *Sculpting organs: mechanical regulation of tissue development*. Annu Rev Biomed Eng, 2012. **14**(1): p. 129-54.
134. Weaver, W.M., et al., *Fluid flow induces biofilm formation in Staphylococcus epidermidis polysaccharide intracellular adhesin-positive clinical isolates*. Appl Environ Microbiol, 2012. **78**(16): p. 5890-6.
135. Shaw, T., et al., *Commonality of elastic relaxation times in biofilms*. Phys Rev Lett, 2004. **93**(9): p. 098102.
136. Batchelor, G.K., *An introduction to fluid dynamics*. 2000: Cambridge university press.



137. Firrell, J.C. and H.H. Lipowsky, *Leukocyte margination and deformation in mesenteric venules of rat*. American Journal of Physiology-Heart and Circulatory Physiology, 1989. **256**(6): p. H1667-H1674.
138. Lipowsky, H.H., S. Kovalcheck, and B.W. Zweifach, *The distribution of blood rheological parameters in the microvasculature of cat mesentery*. Circ Res, 1978. **43**(5): p. 738-749.
139. Alexandre, G., R. Rohr, and R. Bally, *A phase variant of Azospirillum lipoferum lacks a polar flagellum and constitutively expresses mechanosensing lateral flagella*. Appl Environ Microbiol, 1999. **65**(10): p. 4701-4.
140. Belas, R. and R. Suvanasuthi, *The ability of Proteus mirabilis to sense surfaces and regulate virulence gene expression involves FliL, a flagellar basal body protein*. J Bacteriol, 2005. **187**(19): p. 6789-803.
141. Lauriano, C.M., et al., *The sodium-driven flagellar motor controls exopolysaccharide expression in Vibrio cholerae*. J Bacteriol, 2004. **186**(15): p. 4864-74.
142. McCarter, L., M. Hilmen, and M. Silverman, *Flagellar dynamometer controls swarmer cell differentiation of V. parahaemolyticus*. Cell, 1988. **54**(3): p. 345-51.
143. Koch, M., A. Evans, and A. Brunnschweiler, *Microfluidic technology and applications*. Microtechnologies and microsystems series. 2000, Philadelphia, PA: Research Studies Press. xxi, 321 p.
144. Wilensky, U. *NetLogo*. 1999; Available from: <http://ccl.northwestern.edu/netlogo>.

# Curriculum Vitae

## Educational History

Ph.D. expected	2019	Program in Biomedical Engineering Mentor: Andre Levchenko, PhD	Johns Hopkins School of Medicine
B.S.	2011	Bioengineering: Biotechnology <i>Summa cum laude</i>	University of California, San Diego

## Other Professional Experience

Research Assistant	2010-2011	Dept. of Bioengineering, University of California, San Diego Mentor: Bernhard Palsson, PhD
--------------------	-----------	---

## Academic and Other Honors

2011	Dept. of BE Outstanding Academic Achievement Award	University of California, San Diego
2008-2011	<i>William Stout Scholarship</i>	University of California, San Diego
2007-2011	Joe Martin Scholarship	Bank of America

## Publications (peer reviewed)

**Chu, E. K.,** Groisman, A. & Levchenko, A. Quorum cell communication accelerates dynamic response to environment changes (*in preparation*)

**Chu, E. K.\*,** Kilic, O.\*, Cho, H.\*, Groisman, A. & Levchenko, A. Self-induced mechanical stress can trigger biofilm formation in uropathogenic *Escherichia coli*. *Nature Communications* 9, 4087, doi:10.1038/s41467-018-06552-z (2018).

## Posters and Abstracts

**Chu, E. K.,** Groisman, A. & Levchenko, A. Quorum cell communication accelerates dynamic response to environment changes. 2018 BMES annual meeting. (**Oral Presentation**). Atlanta, Georgia. (2018)

## Service and Leadership

2013	Teaching Assistant, Department of Biomedical Engineering, Johns Hopkins University
2010-2011	Teaching Assistant, Department of Bioengineering, University of California, San Diego